An Investigation of Carbon Nanotube Synthesis: Modelling and Experiments

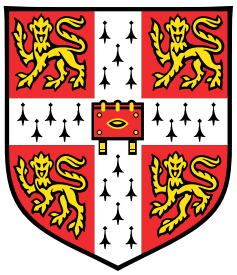

Cen Zhang

Department of Engineering
University of Cambridge

This dissertation is submitted for the degree of
Doctor of Philosophy

Jesus College

October 2018

*I would like to dedicate this thesis to my beloved wife **Xin Jin** and our son **Kaiyin Zhang***

Declaration

I hereby declare that except where specific reference is made to the work of others, the contents of this dissertation are original and have not been submitted in whole or in part for consideration for any other degree or qualification in this, or any other university. This dissertation is my own work and contains nothing which is the outcome of work done in collaboration with others, except as specified in the text and Acknowledgements. This dissertation contains fewer than 65,000 words including appendices, bibliography, footnotes, tables and equations and has fewer than 150 figures.

Cen Zhang
October 2018

Acknowledgements

First, I would like to express my deepest gratitude towards my supervisor, Professor Simone Hochgreb, for her continued support, professional guidance and encouragement throughout the whole period of my PhD studies. Her open-minded, enthusiastic, and rigorous attitude in academic research truly encouraged me to face and solve challenging problems.

I would like to thank Dr. Yi Gao who taught me how to conduct research and carry out experiments independently. Her invaluable advice is greatly appreciated. I would like to thank Dr. Bo Tian for supporting me in many aspects throughout the past four years. I can still recall the moments when we performed the "scary" flame experiments in the dark and noisy lab.

I wish to extend my appreciation to Dr. Cheng Tung Chong who encouraged me to try the hydrogen flame experiments. Without his encouragement, it would be difficult for me to make progress in such a short period of time. I thank Mr. Boning Ding for his generous support and help for conducting SEM and TEM characterisations for the nanomaterials. I am grateful to Dr. Xiao Zhang for his expertise in CNTs and invaluable support. I thank Dr. Adam Boies and Professor Alan Windle for their enlightening advice and support of research.

I sincerely thank my colleagues Dr. Luming Fan, Dr. Kaiqi Hu and Dr. Yaoyao Zheng for borrowing their equipment to me and providing kind support. I appreciate the discussions and suggestions by Dr. Lee Weller. I would like to thank Mr. Xin Chang and Mr. Canlin Ou for helping me conduct the SEM and EDX analysis. I thank Ms. Zhen Du who assisted me with centrifuging samples. I appreciate the professional advice and encouragement from Dr. Wei Meng. I would like to convey my heartfelt gratitude to those who provided me generous support throughout my entire research period in Cambridge.

Last but not the least, I would like to thank my family for their unconditional love and support.

Abstract

Carbon nanotubes (CNTs) possess exceptional mechanical, electrical and thermal properties by virtue of their unique physical structures. In recent decades, continued efforts have been made to develop techniques for producing CNTs on an industrial scale. The floating catalyst chemical vapour deposition (FCCVD) method has been widely accepted as a promising technique for mass production of CNTs. Despite the recent progress in improving the technique, a lack of fundamental understanding of the limiting factors and the underlying mechanisms of CNT synthesis makes it difficult to scale up the production to meet the ever-growing industrial demands. The present study aims to develop numerical and experimental approaches to extend our understanding of CNT synthesis, and ultimately help develop methods for mass production of CNTs.

A multi-phase thermodynamic equilibrium model consisting of C, H, O, Fe and S elements, at stoichiometries and temperatures consistent with CNT synthesis using the FCCVD method was developed. The effects of variable amounts of the different elements, as well as inert species (Ar and N_2) on the species and phase distributions were investigated as a function of temperature at atmospheric pressure. The results reveal that the threshold formation temperature for graphitic carbon products, C(s), increases with the H/C molar ratio. The addition of sulphur into synthesis suppresses the formation of α-Fe(s) in favour of FeS(s). Solid iron carbide Fe_3C(s) takes up all Fe atoms beyond 700 °C, which then turns into liquid phase or dissociates into vapourised Fe(g) beyond 1250 °C. The effect of the estimated bulk Gibbs free energies for different types of CNTs in lieu of C(s) show little change to the overall species and phase distributions within the estimated uncertainties. The effect of inert gases Ar and N_2 relative to H_2 as a carrier gas is found to be a lowered threshold formation temperature for C(s), from ~700 °C in H_2 down to ~100 °C. The formation of C(s) is significantly affected O/C molar ratios where no C(s) shall be formed at O/C > 1.0.

Carbon nanotubes were produced using a premixed laminar flat flame burner where a H_2/air flame was used to provide heat, while feedstocks containing various proportions of carbon and catalyst precursors (ethanol, ferrocene and thiophene) were injected through a central tube to the post flame region. The as-produced nanomaterials were collected at downstream of the post-flame region at a height above burner of 230 mm. Various

techniques were used to characterise the collected samples including Raman spectroscopy, energy-dispersive X-ray spectroscopy (EDX), scanning electron microscopy (SEM) and transmission electron microscopy (TEM). A formation window in the equivalence ratio range $\phi = 1.05 - 1.20$ was identified, and the flame temperature was found to be the dominant limiting factor for the inception of CNTs. CNTs bundles were formed and the diameter of individual CNTs were observed to be lower than 5 nm. The formation of CNTs was accompanied by a production of highly crystalline nanoparticles of a size between 20 nm and 100 nm. These nanoparticles were identified as iron oxides and/or elemental iron nanoparticles by EDX. We studied the role of thiophene in flame synthesis of CNTs for the first time, and found the number density and the overall length of CNTs were markedly improved by adding thiophene to the precursor mixture. The optimum range of the mass ratios of sulphur to iron elements in the catalyst precursors was determined to be 0.1–2.0.

A 2-D diffusion model was developed to assist the understanding of the flame method. The spatial distributions of mixture fraction, local temperature, and axial velocity of flows were obtained. This model serves as a pivotal that links all the numerical methods developed in the thesis, and has the capability of estimating a spatially-resolved species distribution for the flame synthesis. The present project both numerically and experimentally studied CNT synthesis, and extended our understanding of the fundamental mechanisms, shedding light into possible routes for mass production of CNTs.

Table of contents

List of figures

List of tables

Chapter 1

Introduction

Carbon nanotubes (CNTs) were first discovered by Iijima in 1991 whilst using an arc discharge evaporation method for producing fullerene [1]. He reported the formation of "needle-like" cylindrical carbon structures consisting of a few concentric graphitic tubes, ranging in number from a couple up to a few tens. These hollow-shaped CNTs typically consist of a single or multiple walls of graphene layers, and their diameters can range from a few to several tens of nanometres. These unique physical structures, including curved graphitic arrangements, small diameters and high aspect ratios, result in exceptional mechanical, thermal and electrical properties of CNTs, and hence they are widely regarded as one of the most promising and advanced functional materials in the twenty-first century. Since the discovery of CNTs, the past few decades have witnessed a fast expansion of the scientific community of CNT research and their commercial applications. According to the report by Volder *et.al* [2] , the global production capacity of CNTs has experienced more than a 10-fold increase in the annual productivity since 2004. Meanwhile the annual number of publications and related patents in the field are growing at a steady rate.

1.1 Overview of CNTs

1.1.1 Structure and morphology

A CNT can be visualised by wrapping a 2-D graphene sheet into a cylindrical hollow-shaped tube without having their edges overlapped on its surface. The curled graphene sheet consists of numerous hexagonally arranged carbon atoms that constitute the tube. The direction of wrapping the graphene sheet can be taken almost arbitrarily, which results in many possible CNT structures [3]. In Fig.1.1.(a), three main classifications of CNT structures are illustrated, and their featured periodic atomic arrangements that distinguish themselves from the others

are indicated in red. The classification of the CNT structures is primarily performed based on their symmetry: achiral (symmetric) and chiral(non-symmetric) [3]. From Fig.1.1.(a), the armchair and zigzag CNTs are categorised as achiral nanotubes, and the other belongs to chiral nanotubes. As indicated by the red lines shown Fig.1.1.(a), the names of the two different achiral tubes originate from the cross-sectional morphology of the tubes, while a chiral tube does not exhibit such periodic morphology at the cross section, only showing a spiral symmetry.

A widely acknowledged method to precisely describe the atomic structure of a CNT is the use of the tube chiral vector, $\vec{C}_h$, and the chiral angle, θ ($0^\circ \leq |\theta| \leq 30^\circ$) [4]. According to Fig.1.1, the two dotted lines represents the boundaries of the graphene sheet to be wrapped into a CNT, while $\vec{C}_h$ indicates the direction of wrapping, or the circumference of the tube. Hence the chiral can be described as:

$$\vec{C}_h = n\vec{a}_1 + m\vec{a}_2 \tag{1.1}$$

where (n,m) is a pair of integers indicating the number of steps along the zigzag C-C bonds in the hexagonal lattice, and $\vec{a}_1$ and $\vec{a}_2$ are unit vectors, illustrated in Fig.1.1.(b). As indicated in the figure, the angle between the chiral vector $\vec{C}_h$ and the unit vector $\vec{a}_1$ is defined as the chiral angle θ, which indicates the level of "twist" of the tube. Zigzag and armchair CNTs have chiral angles $\theta = 0^\circ$ and 30°, respectively, while those of chiral tubes reside in between. Hence, the chiral indices for zigzag and armchair tubes follow the specific formats as ($n = 0$ or $m = 0$) and ($n = m$), respectively, while the rest of combinations are deemed to be chiral tubes. Given a specific pair of chiral indices (n,m) of a CNT, one shall be able to estimate its diameter as the C-C bond distance in graphene is known as 1.42 $\mathring{A}$.

The knowledge of the chirality of CNTs is crucial for investigation of their material properties. Based on the chirality, single-walled carbon nanotubes (SWCNTs) can be categorised into two main types: metallic and semiconducting CNTs. All armchair SWCNTs are metallic tubes while all others tubes are semiconductors tubes with a band gap [5]. It is important to understand which type(s) of CNTs is(are) formed during the synthesis as their potential applications are determined by the intrinsic properties, although most of the current techniques produce them simultaneously. While there exist some cases where preferential synthesis of either metallic (> 90%) [6] or semiconducting (> 95%)[7] CNTs has been achieved.

Carbon nanotubes may comprise different number of concentric graphene shells, ranging from a single to multiple layers as shown in Fig.1.1.(c). The average diameter of a SWCNT is typically between 1-2 nm, while a further reduction to 0.4 nm can also be attained [8]. Electrical superconductivity has been realised using these extremely thin SWCNTs [9],

which provides a possible direction for its future applications. Multi-walled carbon nanotubes (MWCNTs) can be orders of magnitude larger than SWCNTs depending on their number of walls. The distance between two graphene layers, or wall-to-wall distance, is measured as ~0.4 nm [10].

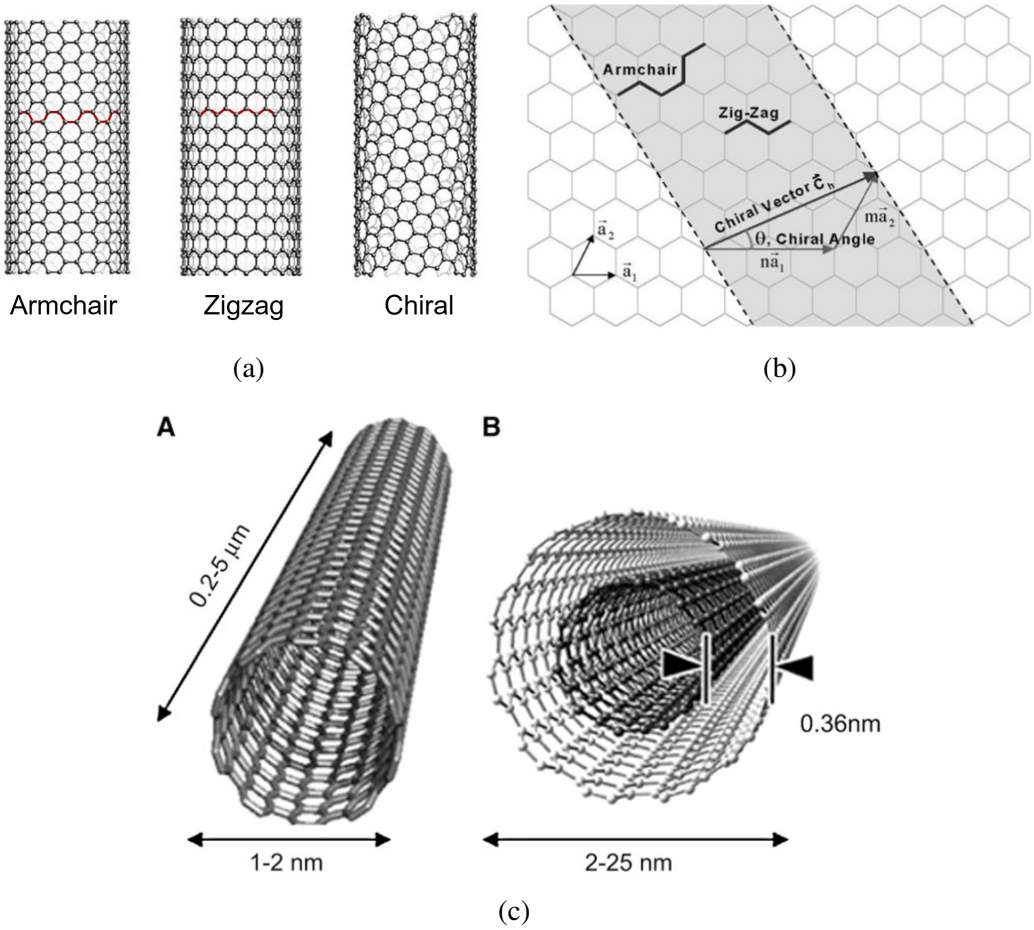

Fig. 1.1 Schematic of structures of carbon nanotubes. (a) Classification of carbon nanotubes (left to right): armchair, zigzag, and chiral nanotubes (figure adapted with permission from Fig.2 in Ref.[11]). (b) Schematic of a single-walled and a multi-walled carbon nanotubes (figure adapted with permission from Fig.1 in Ref.[12]). (c). Schematic of an unwrapped graphene sheet constituting a SWCNT (figure adapted with permission from Fig.1 in Ref.[4]).

1.1.2 Properties of CNTs

According theoretical calculations [13, 14], a defect-free SWCNT typically has a Young's modulus value of ~1 TPa, a tensile strength over 100 GPa and a failure strain of 15-30%, if only considering cross-sectional area of CNT walls. Direct measurements on MWCNTs show

that the actual strength of the nanomaterials can reach ~80% of the theoretical estimation, which is orders of magnitude higher than any of the current industrial fibres [13], and 10-100 times of the strongest steel [4]. MWCNTs have a capability to carry high current densities ($> 10^9$ A/cm^2) without causing any observable damage to the structures [15]. The thermal conductivity of individual SWCNTs is found close to 3500 W m^{-1} K^{-1}) at room temperature, around twice as much as natural diamonds and nearly nine times of copper.

1.1.3 Applications of CNTs

Due to the unique structures of CNTs, which render them exceptional chemical and physical properties, these nanomaterials have been widely studied and applied in many areas. We here introduce some major fields that CNTs have been applied or commercialised. While there exist many other fields for the application of CNTs, more detailed reviews can be find in Ref.[5, 2].

1.1.3.1 Composite materials

The first large-scale commercialisation of MWCNTs is realised in making polymer composites where MWCNTs are added as electrically conducting components by virtue of their high aspect ratios and exceptional electric conductivity [5]. In the automotive sector, conductive CNTs have been incorporated into plastics for manufacturing gas lines and filters. These composites help dissipate electrostatic charge that would otherwise build up and result in explosions [2]. The exceptional mechanical property of CNTs make them highly attractive for manufacturing structural composites especially for weight-sensitive applications. CNT-fibre epoxy composites containing a high volume fraction of CNT fibres ($\geq 25\%$) have been developed, which already achieve a similar level of reinforcement as commercial composites reinforced by high-strength carbon fibres [16]. Apart from enhanced strength and stiffness in composites due to the incorporation of CNTs, CNT fillers can improve material damping without comprising mechanical properties and structural integrity of the composites [17]. Hereby, such nanocomposites can be applied in sporting equipment such as rackets, baseball bats and bicycle frames [2].

1.1.3.2 Coatings and films

Another fast growing field for the application of CNTs is the multi-functional coating industry. Silicone-based coatings doped with a tiny fraction of MWCNTs are reported to significantly reduce biofouling on ships' hulls by weakening the adhesion strength of barnacles [18]. Hence this effect brought by the addition of CNTs helps ships reduce propulsion fuel

consumption and enhance their manoeuvrability. Continued efforts have been made to develop transparent, conductive CNT-base films. It has been reported that SWCNTs can be used to fabricate functional ultrathin transparent films which are optically homogeneous and electrically conductive [19]. These attractive features offer the CNT-based functional films a range of applicable fields including displays, touch-screen devices, and photovoltaics [2].

1.1.3.3 Electrode materials

Another fast expanding field is the research of electrochemical applications of CNT materials. Due to high conductivity, mesoporous character, and resiliency, pure CNTs and their composites are highly competitive materials for fabricating components of electrodes [20]. Although the capacitance of pure CNTs are moderate, from 5 to 40 F/g [21], and are strongly influenced by their microporosity, the capacitance of these CNT materials can be drastically boosted via blending with either electrically conducting polymers such as polypyrrole (capable of reaching 170 F/g) or transition metal oxides such as MnO_2 (capable of reaching 220 F/g) [20]. While the capacitance of the composites is highly sensitive to the alignment and nanostructure of CNTs, and therefore is limited by the current synthesis techniques. Nevertheless, these CNT-based materials are still strong candidates for manufacturing new generation of supercapacitors. In addition, CNTs can also be applied in fuel cell technology as they are found to be an ideal catalyst-support material. Their excellent conductivity enables a fast charge transfer and the unique mesoporosity character facilitates the diffusion of reagent molecules and products in fuel cells [20]. More importantly the use of CNTs in fuel cells can reduce platinum (Pt) consumption and hence potentially lower the manufacturing cost [22].

1.2 Methods of CNT Synthesis

Plasma arc discharge (PAD), pulsed laser vaporisation (PLV) and chemical vapour deposition (CVD) are the three mainstream methods for producing CNTs. Although detailed techniques may differ, all these methods, however, share three common features: (i) a carbon source, (ii) a high temperature and (iii) catalyst precursors.

1.2.1 Arc discharge

The arc discharge method is the technique by which Iijima first discovered the existence of CNTs [1]. In Fig.1.2.(a), a typical arc discharge apparatus is illustrated. This apparatus consists of two pure graphite rods, serving as the anode (+) and cathode (-) which can be vertically or horizontally aligned as shown in the figure. Prior to synthesis, an inert gas,

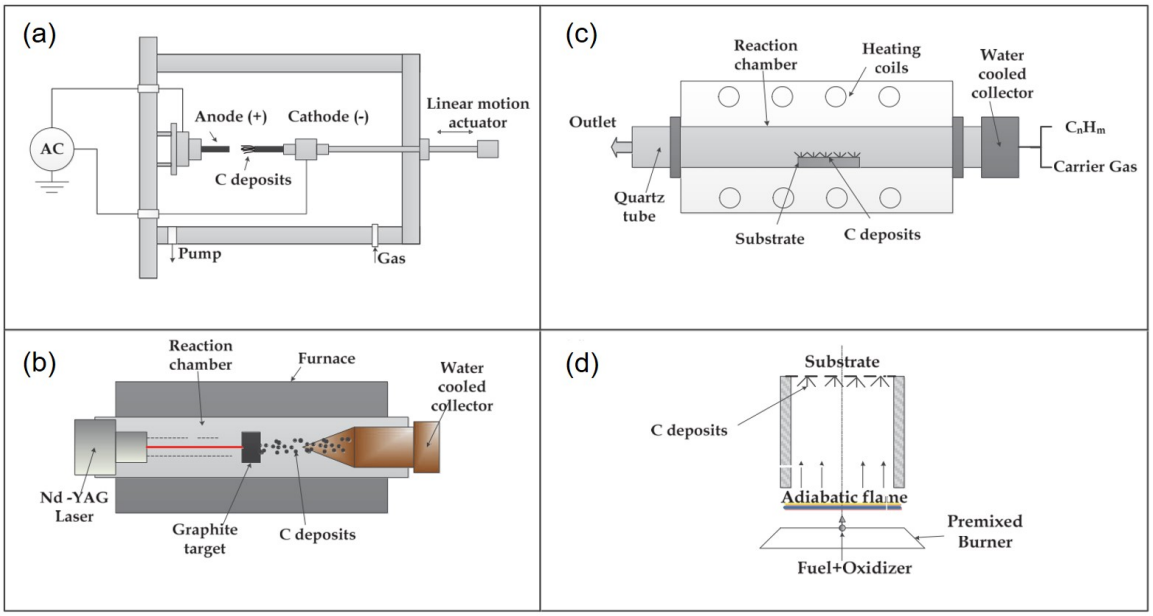

Fig. 1.2 Schematic of CNT synthesis methods: (a) arc discharge, (b) pulsed laser vaporisation, (c) chemical vapour deposition and (d) flame synthesis (figure adapted with permission from Fig.2 in Ref.[23]).

typically helium or argon, is introduced into the chamber to a target pressure. Then an AC/DC arc voltage is applied between the anode and cathode, which results in an evaporation of the carbon materials from the anode. The as-produced carbon materials are mostly fullerenes which are deposited throughout the whole chamber, while a small amount of CNTs can be found in the deposits covered on the cathode [1]. If the anode graphite rode is incorporated with metal catalyst (*e.g.* Fe, Co or Ni) while keeping the cathode graphite rod unaltered, SWCNTs can be produced [24]. Other ambient gases have been studied and it is found gases containing H atoms (*e.g.* CH_4 [25] or H_2)[26] are more effective than inert gases to produce the CNTs. Although highly crystalline CNTs with less defects can be produced via the arc discharge method, the alignment of the as-produced CNTs is hard to control [27]. Nevertheless, the mass production capability of this method is still limited to a laboratory scale, making it less suitable for industrial applications.

1.2.2 Pulsed laser vaporisation

The pulsed laser vaporisation method was initially developed by Smalley *et.al* for the synthesis of fullerenes [28], which was later adapted by the same group to produce SWCNTs [29]. Fig.1.2.(b) illustrates a schematic of a setup of the laser vaporisation technique. The system consists of a laser source (typically Nd:Yag or CO_2 laser [27]), a furnace providing

uniform heat, a quartz tube, a graphite composite target comprising metal catalysts, a water-cooled sample collector and a flow system supplying buffer gases into the quartz tube [30]. When a laser beam is directed to the graphite target, carbon starts to evaporate due to the rapid localised heating by the laser , which leads to the formation of CNTs. The as-produced CNTs are then carried by the buffer gas and captured by the water-cooled collector. This technique possesses several advantages. First, high crystalline SWCNTs with minimal defects and impurities can be produced via this technique [27]. Second, diameters of the as-produced SWCNTs can be controlled by varying the furnace temperatures [31], buffer gas flow rates [32], and metal catalysts [33]. While the disadvantages of the technique are its limited productivity and energy-intensive characteristics, which makes it a less favoured method by industry.

1.2.3 Chemical vapour deposition

Increasing demands for high-quality CNTs require suitable large scale methods for mass production of CNTs. The arc discharge and pulsed laser vaporisation techniques are, however, only suitable for producing CNTs on a laboratory scale, and therefore have very limited potential for scaling up the CNT production. The chemical vapour deposition method (CVD), instead, is capable of producing CNTs with controllable morphologies and in a relatively large quantity [34, 2]. This technique was originally designed to produce carbon filaments in the presence of iron catalysts in 1959 [35]. After the discovery of CNTs [1], CVD methods have been further optimised and developed to accommodate the need of mass production of CNTs. There exist a range of CVD configurations, including fixed beds [36], fluidised beds [37], floating catalysts [34], and many other combinations such as plasma-enhanced CVD methods [38].

Fig.1.2.(c) illustrates a typical setup of CVD method which involves a heating furnace, a quartz/alumina tube and a flow supply system. The general operating procedures for all the CVD configurations are similar: 1) using a furnace to heat a tube reactor and maintain the reactant flows at a target temperature, 2) introducing a feedstock containing carbon sources and catalyst precursors into the tube, and 3) collecting CNTs downstream [30]. The arrangement of the tube reactor can be horizontal or vertical, depending on the technical requirements.

1.2.3.1 Fixed and fluidised CVD

In a fixed-bed CVD system, solid catalyst precursors are placed on a boat which is inserted inside the reactor. When the furnace is heated to the desired temperature, carbon sources

carried by a buffer gas are introduced into the reactor, and CNTs start to grow upon the catalytic sites on the surface of the precursors. This process is however heavily limited by the inhomogeneous interactions between gaseous carbon sources and the catalyst particles, where the ever-growing CNTs cover the catalytic sites on the surfaces, deactivating the catalysts fixed on the boat [37]. While in a fluidised-bed CVD system, the tube reactor is usually placed vertically in which supported catalyst particles are suspended by an upward buffer gas. This arrangement allows a homogeneous mixing of gaseous carbon sources and catalyst particles, and a better heat transfer [39].

1.2.3.2 Floating catalyst CVD

Currently a mass production of CNTs is primarily achieved by CVD methods, among which the floating catalyst CVD (FCCVD) is one of the most attractive techniques. This method is an economical, controllable and continuous industrial scalable tool [40], which allows a direct withdrawal of CNT fibres from the reactor tube [34]. In this method, the catalysts are firstly vaporised and then driven into the hot reaction zone instead of being supported by a fixed substrate bed. As a result, the suspended catalysts in the reactant flows are mixed with carbon sources, which promotes the CNT inception and growth and, most importantly, makes it possible to continuously produce CNTs in a large quantity.

The continuous mass production of CNTs by the direct spinning FCCVD was initially reported by Windle et.al [34], as shown in Fig.1.3. From the figure, one can see that CNT fibres formed in the reactor are continuously drawn out by a rotating spindle either vertically (Fig.1.3.(A)) or horizontally placed (Fig.1.3.(B)). Apart from the vertical arrangement setup, this technique also has a horizontal version which has the same direct-spinning characteristics [41]. This method normally involves a continuous and controlled supply of carbon source (*e.g.* ethanol [34, 42], toluene [43] or carbon monoxide [44]), an iron-based catalyst (*e.g.* ferrocene [34] or iron pentacarbonyl [44]), and a sulphur source (typically thiophene [34, 45, 42, 41]). These precursors carried by a buffer gas (typically H_2, or inert gases such as N_2 or Ar [46–48]) are injected into a tubular reactor which is kept at temperatures of ~1000 °C. The positive temperature gradient upstream of the tubular reactor accelerates the pyrolysis of the iron and sulphur catalysts, which in turn leads to the nucleation of nanoparticles for the subsequent carbon deposition. The whole process takes place in a furnace heated between 1100 °C and 1450 °C, at residence times of the order of tens of seconds [49].

Windle's group [34, 42, 50] have carried out a series of investigations on the mechanisms of CNT formation, and they primarily focused on the therapy consisting of ethanol (the carbon source), ferrocene (the iron precursor) and thiophene (the sulphur precursor). They found that methane and water were generated by the thermal decomposition of ethanol at

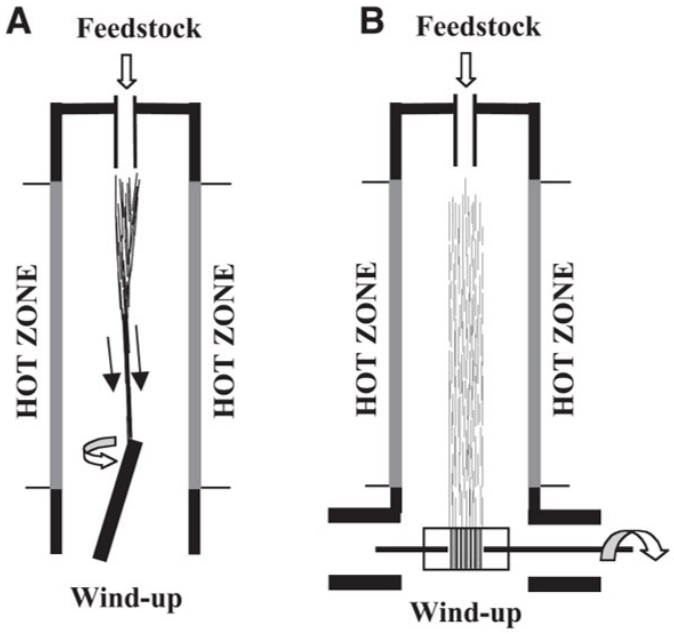

Fig. 1.3 Schematic of the direct spinning process in a floating catalyst CVD system developed by Windle *et.al* [34]. Left: schematic of direct spinning of CNT fibres by a vertical rotating spindle inside a tube reactor. Right: schematic of direct spinning of CNT fibres by a horizontal rotating spindle outside a tube reactor. (Figure adapted with permission from Fig.1 in Ref.[34].)

high temperatures, and the as-produced methane then reacted with iron nanoparticles to form hydrogen and CNTs based on the following reaction [50]:

$$CH_4(g) \rightarrow 2H_2(g) + C(s) \tag{1.2}$$

The widely accepted mechanism for CNT formation is that the gas-phase carbon is initially generated as a result of the pyrolysis of carbon sources before being absorbed by metal catalyst nanoparticles [50]. When the carbon absorption reaches its saturation point, carbon atoms precipitate out to form cylindrical CNTs on the surfaces of the catalyst nanoparticles [51]. Although progress has been made in developing semi-empirical recipes for the production of spinnable fibres [34, 52, 50], the underlying chemical, nucleation and agglomeration mechanisms of CNT formation in this method are not fully understood.

Although CVD possesses many advantages over the other techniques such as mass production capability, continuous process and controllable synthesis, its productivity and the quality of CNT products still fall short of the ever-growing industrial demands. Moreover, CVD is an energy intensive technique which needs continuous power supply for furnace

heating, and the complexity of the apparatus assembly together with its manufacturing and maintenance costs drives up the commercial prices of CNTs produced using the method.

1.2.4 Flame synthesis

Apart from the previously introduced methods, flame synthesis gradually becomes an attractive alternative for CNT production as it possesses the potential for a continuous mass production of CNTs at a significantly lower cost than any of the mainstream synthesis methods. Over the past few decades, flame synthesis of nanomaterials has gained increasing popularity, and many commercial products are produced using this method including carbon blacks (Cabot, Birla Carbon), fumed silica (Cabot, Evonik), titanium dioxide pigment (Cristal, Millenium) and other ceramics, with an estimated of production of millions of tons valued at over $15 billion per year [53]. The discovery of MWCNTs in flames were first reported by Howard *et.al* while he performed the synthesis using premixed hydrocarbon/oxygen flames (C_2H_2, C_2H_4 and C_6H_6) in a low pressure chamber [54]. Various flame configurations have been developed for producing CNTs since then, and a comprehensive review can be found in Ref.[30, 55].

Unlike a CVD system that normally requires a furnace to generate heat, a flame synthesis method, instead, produces heat by a direct combustion of flammable mixtures. A typical flame synthesis system is generally much simpler than a CVD method, which typically consists of a premixed or diffusion flame burner, a flow supply system and a collection unit. Despite of various types, the flame systems can be summarised into two main categories based on the types of flames: 1) diffusion flame [56–58], and 2) premixed flame[59–63] configurations. Whichever flame configuration is used, it must provide an appropriate carbon source to generate gas-phase carbon species for CNT formation. Moreover a stable heat source is critical to the decomposition of catalytic precursors and the subsequent formation of the catalyst nanoparticles. These elemental metal nanoparticles are activated in flames where the inception of the solid graphitic layers is initiated due to the high temperature environment [30]. Then, CNTs start to grow on the surface of metal nanoparticles either supported by a metal alloy substrate [60], or suspended in gases [63].

1.2.4.1 Diffusion flame configuration

As shown in Fig.1.4.(a), the co-flow diffusion flame is one of the simplest flame configurations used for CNT synthesis. Air or oxygen is supplied from the outer ring of the burner while the fuel is injected through the central tube. CNTs are then produced on a substrate containing catalyst precursors (Ni, Fe, Co, *etc.*) placed on top of the diffusion flame. This configuration

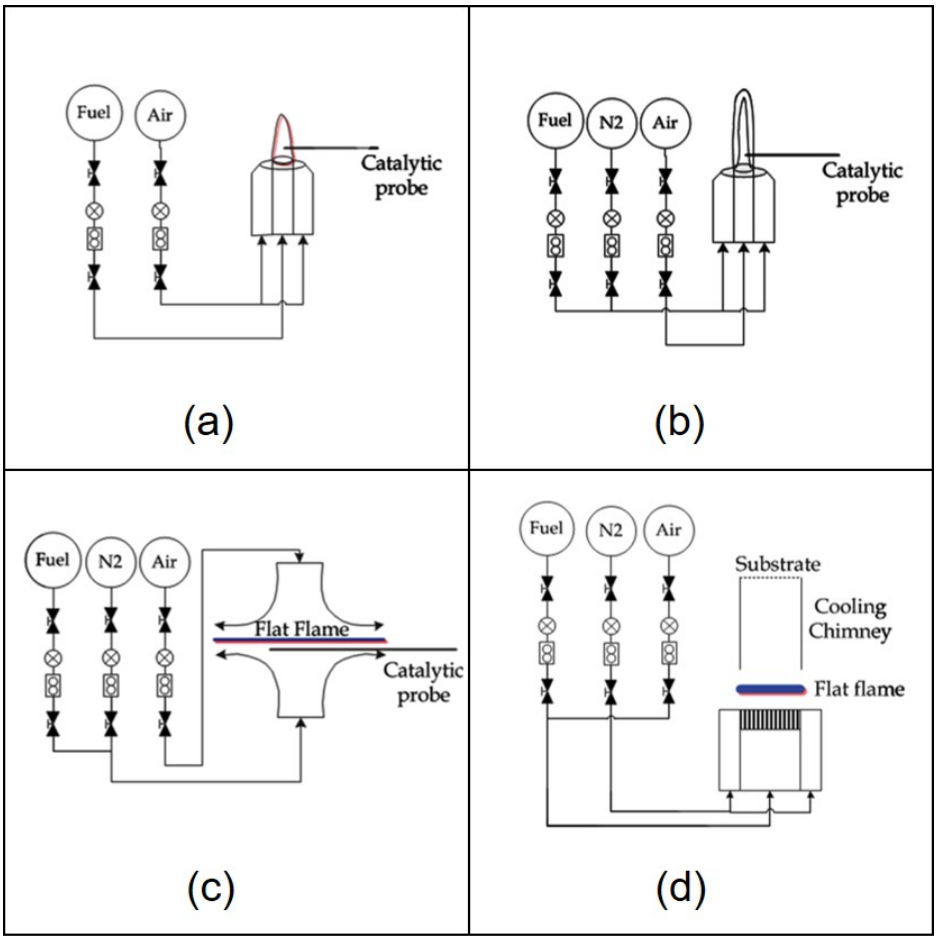

Fig. 1.4 Schematic of flame synthesis configurations: (a) co-flow diffusion flame, (b) inverse diffusion flame (c) counter-flow diffusion flame, and (d) premixed flame. (Figure adapted with permission from Fig.4 in Ref.[23].)

possesses some advantages such as ease of assembly and minimal risk of flashback. It has been reported acetylene-air [64], methane–air [65, 57] and ethylene-air [57] diffusion flames can be used to produce CNTs at atmospheric pressure on the co-flow diffusion configuration. While it also has some disadvantages. For instance, soot formation is a common problem during the synthesis if hydrocarbon is used as the fuel. Moreover, CNTs must be extracted from the flame at a very early stage, as the nanomaterials would be otherwise oxidised by the downstream oxygen-rich environment [66].

Fig.1.4.(b) illustrates the setup of an inverse diffusion flame burner. In contrast to the co-flow configuration, the flow supply in this setup is inversely arranged where the fuel is supplied via the outer ring while air through the central tube to generate an inverse diffusion flame. Diffusion flame with a high stoichiometric mixture fraction (Z_{st}) can be achieved using this method, which helps eliminate the formation of soot and polycyclic aromatic

hydrocarbons (PAHs) during the synthesis [66]. Furthermore, it allows CNTs to form in the fuel-rich region where oxidisation at downstream of the flame is hence avoided.

Another widely used diffusion flame configuration is the counter-flow setup as shown in Fig.1.4.(c). It consists of two vertically aligned cylindrical burner where the fuel and air streams are supplied from the bottom and top nozzles separately (or the other way around), which creates a stagnated diffusion flame plane in-between. The main advantage of this geometry is to provide a 1-D flow field along the stagnation plane that markedly facilitates numerical interpretations of the synthesis [67, 68]. It is reported that CNTs can be produced using methane-oxygen [58, 69] and ethylene-methane-oxygen flames [70] via this method.

1.2.4.2 Premixed flame configuration

The premixed flame configuration is favoured by many researchers due to its simple 1-D flame structure that facilitates the characterisation of the process via numerical analysis compared with their diffusion counterparts. More importantly, the species distribution can be analysed by thermodynamic equilibrium calculations and kinetic modelling, and hence it becomes a promising tool to help research unveil the underlying mechanisms of CNT synthesis [71]. Another advantage of using premixed flames is the flexibility of varying equivalence ratios ϕ achieved by changing the relative supply of the fuel and oxidiser streams. As a result, flame temperatures can be readily controlled, allowing a comprehensive parametric study for the CNT production. The configuration of the premixed flame system mainly falls into two categories: 1) catalyst support and 2) floating catalyst types.

The catalyst support configuration is widely used for producing CNTs as the materials can directly grow upon the catalyst nanoparticles (typically Ni [62] or Co [72, 56, 60]) coated on a metal grid/mesh. This method is easy to perform, and the as-produced materials can be directly collected from the substrates. Various fuels have been used for producing CNTs including C_2H_4, C_2H_2, CH_4, H_2 and CO [72, 57, 62, 73, 56, 60]. However, the yield of this method is limited to a laboratory scale due to the substrate support feature, hence not suitable for industrial applications.

The floating catalyst premixed flame configuration, on the other hand, possesses the potential for a large scale production of CNTs due to the absence of substrates. Instead, vaporised catalyst precursors and carbon sources are supplied to the reaction zone, which resembles a FCCVD configuration. Most importantly, various *in situ* diagnostic techniques *e.g.* laser-induced incandescence (LII) and light extinction method can be used for studying this process, and computational analysis becomes relatively easy to perform.

There exist a few of studies using the floating catalyst premixed flame method, and most of them were undertaken at low pressures. Table 1.1 summarises the studies using the floating

Table 1.1 Experimental conditions for CNT synthesis using the floating catalyst premixed flame method.

Literature	Fuel/oxidiser	ϕ	Catalyst	Carrier gas	P/atm
Diener [59]	C_2H_2/O_2; C_2H_4/O_2; C_6H_6/O_2	1.7–3.8	Fe, Ni, Co	Ar	0.1
Vander Wal [73, 74]	C_2H_2/air	1.5–1.75	Fe	CO/H_2/He; C_2H_2/H_2/He	1
Height [63]	C_2H_2/O_2/Ar	1.4–2.2	Fe	Ar	0.07
Wen [75]	CH_4/O_2/Ar	2.0–2.1	Fe	Ar	0.26

catalyst configuration for CNT synthesis. Diener et al. [59] investigated the synthesis of SWCNTs at low pressures, using a combustion apparatus originally designed for producing fullerenes. Different fuels (C_2H_2, C_2H_4 and C_6H_6) and catalyst metal precursors (Fe, Ni and Co) were tested for the synthesis, and the results showed that both C_2H_2 and C_2H_4 flames were capable of producing SWCNTs along with a small quantity of MWCNTs, at ϕ between 1.7 and 3.8. C_6H_6/O_2 flames, however, only produced long metal-filled MWCNTs in a large quantity–estimated as 10% of the overall solid carbon production–over the same equivalence range, and no SWCNTs were observed.

Height *et al.* [63] further investigated CNT synthesis in premixed C_2H_2/O_2/15%Ar flames at a low pressure condition (0.07 atm). Argon was used to carry the catalyst precursor, iron pentacarbonly ($Fe(CO)_5$) vapour, at a feeding concentration of 6000 ± 500 ppm (by molar) for the synthesis. The overall yield of nanotubes was estimated as low as 0.1 wt.% of carbon and 2.5 wt.% of iron. A "formation window" for CNTs was identified as $\phi = 1.5 - 1.9$. Based on their observations, catalyst particles primarily formed between 10 mm and 40 mm height above burner (HAB) in the post-flame region, while CNTs started to form at 30 mm HAB, and continued to grow up to 70 mm HAB. Iron oxides, primarily Fe_2O_3, were identified and they attributed the growth of CNTs to the catalytic feature of Fe_2O_3, which is however doubtful based on our current understanding.

A further investigation of CNT synthesis was conducted by Wen *et al.* [75] who used the same experimental setup as Height's [63] but different premixed flame compositions–CH_4/O_2/15%Ar flame. The operating pressure was still maintained at a low pressure (0.26 atm), and the feeding concentration of metal catalyst $Fe(CO)_5$ was reduced to between 100 ppm to 500 ppm (by molar). Their results identified the formation window for CNTs at ϕ

of 2.0-2.2. In addition, they observed two types of iron nanoparticles during synthesis by conducting EDX (energy dispersive X-ray) and X-ray diffraction (XRD) analyses: 1) iron oxide (Fe_3O_4 and Fe_2O_3) and 2) elemental iron coated with graphite layers. While the later was found to be the direct catalyst for the growth of SWCNTs rather than iron oxides as suggested by Height [63].

Instead of directly mixing catalyst precursors with combustible mixtures into the flames, Vander Wal *et.al* created a pyrolysis flame configuration for CNTs synthesis [74, 73]. This setup consisted of a hybrid configuration where a McKenna burner with a central tube of 10 mm was used to stabilise premixed flames for heat supply, whilist a 7.6 mm long stainless steel tube of 25 mm outer diameter, called a "chimney" structure, was placed just above the central tube at 10 mm HAB. C_2H_2/air premixed flames were stabilised on the outer ring of the burner, while metal catalyst precursors, ferrocene, were carried by different gas mixtures, CO/H_2/He or C_2H_2/H_2/He, through the central tube into the chimney. The materials were collected by a thermophoretic probe inserted inside the chimney. In their setup, the outer ring of premixed flame serves as the heat source, and the mixture gases, supplied through the central tube containing both the carbon source (CO or C_2H_2) and the catalyst precursors, are heated inside the chimney via heat transfer by the hot post-flame products. It is worth noting that a fraction of post-flame products including CO_2, H_2O, unburnt hydrocarbon species and soot particles also enter the chimney, which may also participate in the synthesis. The results showed that CO was "superior" to C_2H_2 in terms of being as the carbon source. PAHs formed while using C_2H_2 were found to be detrimental to the CNT formation due to their high thermodynamic stability and the inherent resistance to catalytic cracking [73]. The role of H_2 was discussed, and they suggested that an appropriate amount of H_2 in the synthesis could help remove surface carbon species on catalyst nanoparticles, including iron carbides and amorphous carbon, and retain the activity of the catalytic sites on the surfaces of the nanoparticles [74].

Although many attempts have been made to produce CNTs using various flame configurations, the mechanisms of CNT synthesis are still not fully understood. The complexity and challenges reside in the flame medium, even for a premixed flame. A flame medium is rich in intermediate radicals formed during rapid and intense homogeneous reactions [30], and the typical by-products such as PAHs formed in the fuel-rich hydrocarbon flames make the analysis even more challenging. Hereby there is an urgent need to find a new way of producing CNTs via the flame method where the formation of the intermediates and by-products such as PAHs can be minimised.

1.2.5 Comparison between FCCVD and flame synthesis

The FCCVD and the floating catalyst premixed flame methods both share many common features. First, they both use gaseous mixtures of carbon and catalyst precursors for the synthesis, which is suitable for a continuous mass production of CNTs. Second, they share most of the precursors, including carbon sources (*e.g.* methane and ethylene), and metal precursors (ferrocene and iron pentacarbonyl), although the addition of sulphur precursor has not yet been reported in the flame studies. While differences between the two methods are obvious. For the FCCVD technique, the heat source is provided by a furnace which has a certain operating temperature range, and a controllable temperature gradient. Therefore, the reaction inside the furnace reactor can be more precisely controlled. Whereas, the hot region in the flame system is sustained by flame fronts generated by the combustion of flammable mixtures. This however produces a sharp temperature gradient across the reaction zone which might be adverse to CNT synthesis. One of the major challenges of using a FCCVD system is to apply *in situ* non-intrusive diagnostic techniques to study the synthesis process in real time due to the enclosed heating furnace. The species distribution and the complex inception and formation mechanisms of CNTs in the tube reactor are therefore difficult to fully visualise and understand. In contrast, the premixed flame configuration possesses a relatively simpler structure and optically accessible characteristics. Moreover, there exist many models already developed for studying the chemical reactions in flames. In addition, *in situ* diagnostic techniques have been extensively used in the combustion field, and a burner setup can be easily modified to accommodate the need for a real-time diagnostics.

Although a continuous mass production of CNTs has been achieved by FCCVD methods, their current throughput still fall short of industrial demands due to lack of a thorough understanding of the synthesis process. Therefore, there is an urgent need of developing new methods for studying the underlying physics and chemistry of CNTs.

1.3 Aims and objectives

The present project aims to develop numerical tools and experimental methods to extend the understanding of the mechanisms of CNT synthesis. The primary objectives of the thesis are to:

1. Develop a thermodynamic equilibrium model using the software suite Cantera [76] to investigate equilibrium species distributions in a FCCVD system.

2. Design a premixed flame configuration that minimises the formation of intermediates and by-products in flames to study the synthesis of CNTs.

3. Develop a numerical model to simulate the flame synthesis and improve the understanding of the process.

1.4 Thesis structure

Chapter 1 introduces the background of carbon nanotubes, including their structures, properties, and current applications. The methods of CNT synthesis are reviewed with an emphasis of chemical vapour deposition methods (CVD). And the flame synthesis method, as an emerging technique, is introduced and compared against CVD methods.

Chapter 2 describes the methodology of the thermodynamic equilibrium model developed for investigating species distributions in FCCVD systems. The thermodynamic properties of different CNTs reported in literature are summarised and compared.

Chapter 3 discusses equilibrium species distributions based on successful input conditions in FCCVD systems. Results in a broader range of input conditions are also demonstrated. The effect of oxygen in CVD systems on CNT synthesis is discussed.

Chapter 4 demonstrates the design of the floating catalyst premixed flame system for CNT synthesis. Details of the primary components are illustrated, and the experimental procedures are described.

Chapter 5 summarises the results of the parametric study using premixed H_2/air flames. Key parameters controlling the CNT synthesis are discussed. Results from the numerical study using a 1-D burner stabilised flame model are included.

Chapter 6 discusses the roles of ferrocene and thiophene in the flame synthesis of CNTs. Results from the parametric study of different amounts of ferrocene and thiophene are summarised and discussed.

Chapter 7 introduces a 2-D diffusion model established to describe the synthesis environment of the flame method. A numerical analysis procedure that connects all three models developed in the thesis is proposed.

Chapter 8 presents a summary of the thesis and lays out plans for future work on both numerical modelling and experimental studies.

Chapter 2

Methodology of Equilibrium Study on FCCVD Synthesis of CNTs

2.1 Introduction

Thermodynamic equilibrium calculations are widely used in the field of combustion to determine adiabatic flame temperatures and the post-flame species distributions. This numerical method has also been used to predict carbon deposition in fuel cells. Formation of solid carbon on the surface of the anode leads to an obstruction of gas transport and hence restricts the performance of a fuel cell [77]. Most of current thermodynamic equilibrium model centres only on gas phase equilibria, and there exist a few studies that investigate gas-solid phase equilibria by considering the existence of graphite [78, 79] or carbon nanofibres/tubes [77, 80] in fuel cells. However, to the best of our knowledge, the thermodynamic equilibrium method has not yet been applied for studying the species distribution in a FCCVD scenario. In this chapter, we introduce the model of the thermodynamic equilibrium used for analysing the species distribution in FCCVD synthesis. The present work aims to study this process from a thermodynamic perspective, by asking the questions: what are the expected equilibrium products over a range of temperatures, and how are they shifted by changing the stoichiometry of H, C, S, Fe and O? Are these consistent with observed products? The comparison of the resulting expected equilibrium compositions with the real products offers insight into what rate limiting processes may be playing a role in the real system. Since thermodynamic properties are described in terms of Kelvin (symbol: K), we therefore use the Kelvin scale to describe the results in Chapter 2 and 3.

2.2 Thermodynamic equilibrium calculations

2.2.1 Method

The thermodynamic equilibrium of a mixture can be represented by a set of simultaneous non-linear equations connecting the thermodynamic properties of substances, subject to the laws of atomic conservation [81]. There two major methods for calculating equilibrium compositions of a mixture: the equilibrium constant method and the Gibbs free energy minimisation method. The first method becomes quickly impractical for a moderate number of species, so the second method is adopted here. The total Gibbs free energy, G, of an ideal chemical mixture is a function of temperature T, pressure P and the number of moles of each species n_i, given in the canonical form as

$$G = f(T,P,n_i) = \sum_{i=1}^{I} n_i g_i \tag{2.1}$$

where g_i is the partial molar Gibbs free energy of species i expressed as,

$$g_i \equiv \left.\frac{\partial G}{\partial n_i}\right|_{T,P,n_{j\neq i}} \tag{2.2}$$

Based on the definition of Gibbs free energy, g_i can hence be described as,

$$g_i = h_i - Ts_i = g_i^0 + \mathscr{R}T\left(\ln\frac{Px_i}{P_0}\right) \tag{2.3}$$

where g_i^0 is the standard Gibbs energy of species i at a standard state condition P_0 (usually 1 bar), x_i is the molar fraction for species i in mixture, and h_i and s_i are its partial molar enthalpy and entropy, respectively. v is the specific volume, $\mathscr{R}$ is the universal gas constant.

For condensed phases, since solids and liquids can be usually treated as incompressible *i.e.* the specific volume v_i^0 of the substances can be assumed constant with pressure, the entropy of their pure substance therefore only depends on temperature. Hence the partial molar entropy for condensed species,$s_{i,c}$, is given as,

$$s_{i,c} = s_{i,c}^0 - \mathscr{R}\ln x_i \tag{2.4}$$

Then the partial Gibbs free energy for condensed species i can be obtained by:

$$g_{i,c} = h_{i,c} - Ts_{i,c} = g_{i,c}^0 + v_i^0(P_{i,c} - P_0) + \mathscr{R}T\ln x_{i,c} \tag{2.5}$$

Here each condensed species is regarded as a pure substance, *i.e.* the molar fraction of the condensed species i, $x_{i,c}$, equals to unity, and $P_{i,c}$ then becomes the total pressure of the environment P.

The standard Gibbs free energy at atmospheric pressure is defined as:

$$g_i^0 = h_i^0 - T s_i^0 \tag{2.6}$$

where standard molar specific enthalpy h_i^0 and entropy s_i^0 are only a function of temperature, and include the Gibbs free energy of formation $\Delta g_{f,i}^0 = \Delta h_{f,i}^0 - T_0 \Delta s_{f,i}^0$ at the standard state (101.325 kPa and 298 K), tabulated for many species in thermodynamic databases [82].

$$g_i^0 = g_i^0 - g_i^0(T_0) + \Delta g_{f,i}^0 \tag{2.7}$$

The dependence of the absolute standard molar specific enthalpy and entropy is expressed in the form of polynomials, which have traditionally saved computational time, as follows [82]:

$$\frac{c_p^0}{\mathscr{R}} = a_0 + a_1 T + a_2 T^2 + a_3 T^3 + a_4 T^4 \tag{2.8a}$$

$$\frac{h^0}{\mathscr{R}T} = a_0 + \frac{a_1}{2} T + \frac{a_2 T^2}{3} + \frac{a_3 T^3}{4} + \frac{a_4 T^4}{5} + \frac{a_5}{T} \tag{2.8b}$$

$$\frac{s^0}{\mathscr{R}} = a_0 \ln T + a_1 T + a_2 \frac{T^2}{2} + a_3 \frac{T^3}{3} + a_4 \frac{T^4}{4} + a_6 \tag{2.8c}$$

These fitting parameters (a_0 to a_4) are obtained by means of a least-squares fit (4^{th} order polynomial), and a_5 and a_6 are obtained by referencing the standard enthalpy and entropy formation, respectively. Given an existing database of species, equilibrium calculations for mixtures of the same can be performed. The ideal gas assumption is valid under these low pressure dilute conditions. Condensed phases are also assumed to be ideal mixtures, although this could be revised if sufficient information about activity is available.

2.2.2 Equilibrium conditions

The equilibrium molar fraction of all the species involved in a system at constant pressure and temperature can be determined by minimising the total Gibbs free energy of a mixture G according to:

$$dG = \sum_{i=1}^{I} g_i(T,P) dn_i = 0 \tag{2.9}$$

subject to the constraints of atomic conservation:

$$b_j = \sum_{m=1}^{M} \sum_{i=1}^{I} a_{i,j,m} n_{i,m} \tag{2.10}$$

where $a_{i,j,m}$ is the number of atoms of element j in species i of phase m, and b_j is the total number of atoms of element j. The stoichiometric Villars-Cruise-Smith (VCS) algorithm is particularly suited for handling multiphase problems [83, 84]. In the present study, the software suite Cantera [76] implements this algorithm to solve equilibrium problems. The program has been widely used in chemistry and engineering research fields and is a collection of object-oriented software tools for calculating problems of chemical kinetics, thermodynamics and/or transport processes.

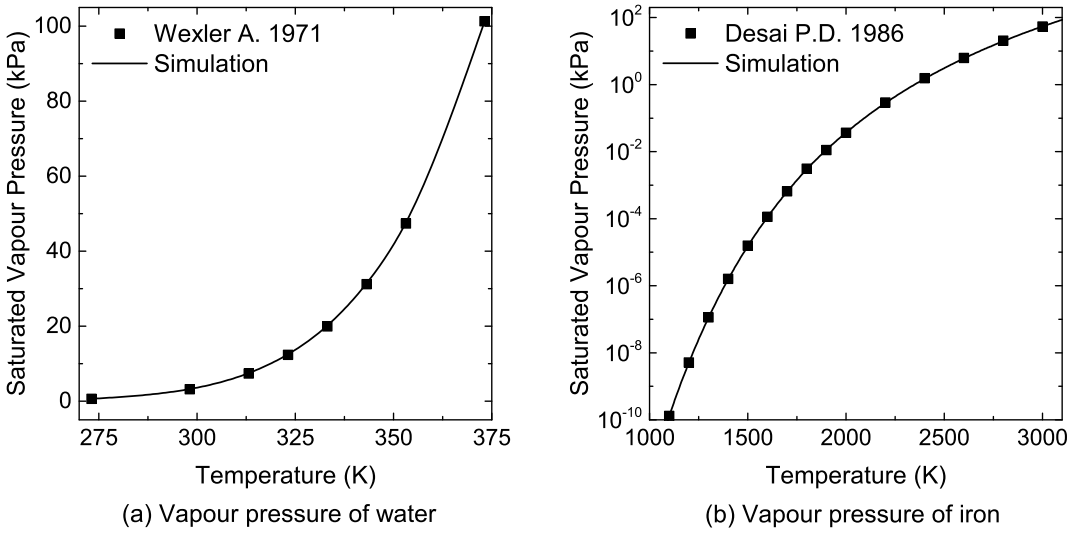

Fig. 2.1 Comparison of calculated vapour pressures of (a) water and (b) iron against their experimental values (water and iron data from Ref.[85] and [86], respectively).

2.2.3 Solver validation

The results obtained using the three-phase equilibrium code were first verified by calculating known saturated vapour pressures of water and iron over a wide range of temperatures up to their respective boiling points. Simulation results were compared against literature data for water [85] and iron [86]. Fig.2.1 shows excellent agreement in both cases.

Further validation was performed by simulating pyrolysis of methane including formation of solid phase graphite at atmospheric pressure against simulation results by Sasaki *et al.* [78]

who used a different equilibrium solver (HSC chemistry Version 4.1, Outokumpu Research Oy, Finland). Fig.2.2 illustrates the evolution of major species CH_4, H_2 and graphite, C(s), calculated by both solvers, showing exact agreement.

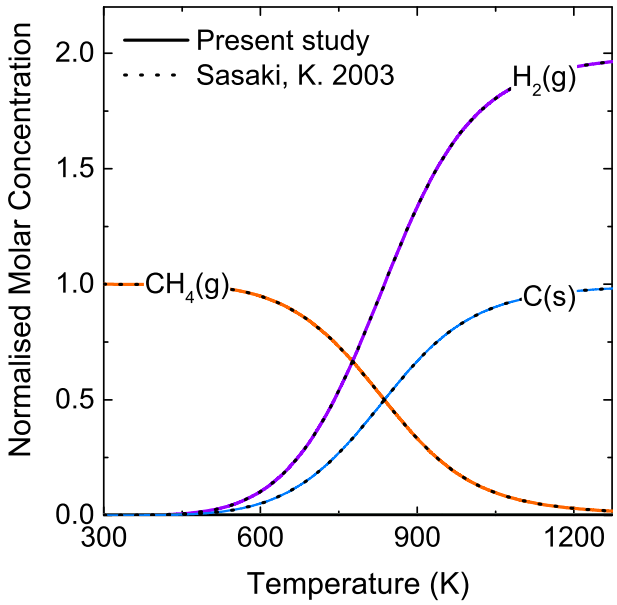

Fig. 2.2 Comparison of methane pyrolysis results in the present simulations solver and those in Ref.[78]. The number of moles of all species considered are normalised to CH_4.

2.2.4 Species and phases

The present calculations include over 100 species in various phases, and the full list can be found in Appendix A. Most of the species considered herein have well-established thermodynamic properties provided in [82]. Properties for condensed phase iron carbide, Fe_3C(s) and Fe_3C(l) were extracted from Burcat's thermodynamic database [87], as were the properties for gas phase thiophene, C_4H_4S(g), and ferrous sulphide, FeS(g). Fe_3C, or cementite, is a metastable phase and it is very likely to decompose into Fe and graphite at higher temperatures beyond its melting point [88, 89]. Thermodynamic properties of ferrocene, $Fe(C_5H_5)_2$, were extracted from Fulem *et al.*'s theoretical estimations [90].

Thermodynamic properties of ferrocene were extracted from Fulem *et al.* [90] and Simões's organometallic thermochemistry Data [91], using a 7-parameter polynomial fit (see Eq.2.8). Since the reference only provides ferrocene data covering the lower temperature range (200 to 1000 K), the thermodynamic properties beyond this temperature range were

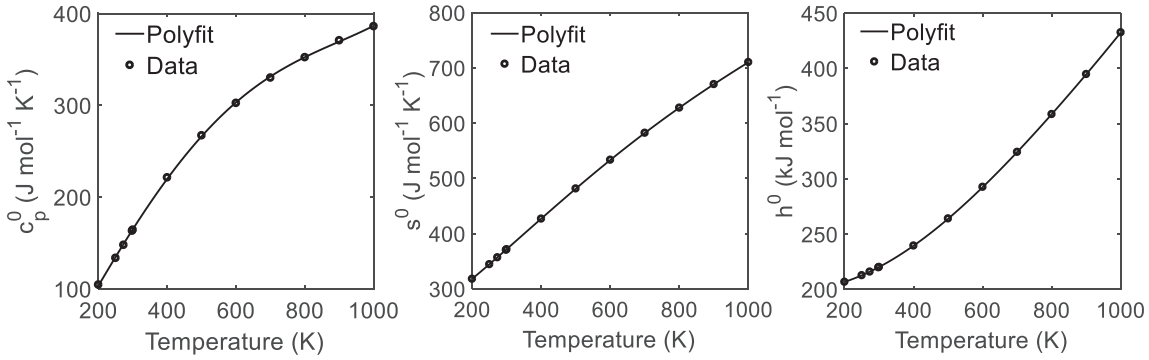

Fig. 2.3 Fitted curves of thermodynamic properties of ferrocene based on data from Ref.[90] between 200 K and 1000 K. Left: specific molar heat capacity, middle: specific molar entropy, right: specific molar enthalpy.

extrapolated automatically by the solver. This does not affect the calculation, as no ferrocene survives beyond 1000 K.

Fig.2.3 shows the reference data of specific molar heat capacity c_p^0, entropy s^0 and enthalpy h^0 of ferrocene [90] and their corresponding fitted curves. The seven parameters are determined as follows: a) 4^{th}-degree of polynomial is initially fitted to the data of c_p^0, and 5 parameters, $a_0 - a_4$ are derived accordingly, b) parameters a_5 and a_6 are calculated by based on the standard enthalpies of formation and standard entropies of ferrocene provided in the references, respectively, c) all the parameters obtained are then used to fit the data for h^0 and s^0 according to Eq.2.8.

Table 2.1 Reactor reference conditions

Species	Flow rate	Unit
H_2	800	ml/min
CH_4	80	ml/min
$Fe(C_5H_5)_2$	0.35	mg/min
C_4H_4S	1.3	mg/min
Nominal ratios	Molar	Mass
H/C	23	2
C/Fe	2000	430
C/S	250	90

2.3 Test conditions

Typical furnace temperatures for CNT aerogel using the FCCVD method are between 1423–1723 K (or 1150–1450 °C) [49] at atmospheric pressure. The present calculations cover a

temperature range of 300–2200 K to understand the sensitivity to temperatures, as well as to shed light into the process.

The baseline and ranges of flow conditions in the reactor are as indicated on Table 2.1, as reported by Gspann *et al.* [52]. A carrier flow of hydrogen is used, with a molar ratio H_2/CH_4 at 10, and much smaller flow rates of ferrocene and thiophene. Therefore the baseline molar ratios between the elements are normalised with respect to that of Fe as H:C:S:Fe $= 45500 : 2000 : 8 : 1$. This ratio was varied away from the baseline by changing the relative amount of different elements to understand the sensitivity of the equilibrium species distributions over a range of temperatures considered.

Chapter 3

Equilibrium Study on Species Distributions in CNT synthesis

3.1 Introduction

In this chapter, we investigate species distributions in a FCCVD system by applying the thermodynamic equilibrium method described in Chapter 2. As already introduced in Chapter 1, various carbon sources can be used to produce CNTs such as methane [92], benzene [93], toluene [94] and ethanol [34, 94]. The major difference in comparing different carbon sources for the synthesis in terms of thermodynamic equilibrium is whether or not to include oxygen into calculations. The H/C ratio of all species present in a FCCVD system is primarily determined by the amount of H_2 (excluding the cases using inert gases to carry reactants) as the buffer gas rather than the internal H/C ratio of carbon sources. We hereby separate our study into two parts: 1) a C-H-Fe-S system and 2) a C-H-Fe-S-O system.

3.2 C-H-Fe-S system

3.2.1 Methane pyrolysis in hydrogen

We start by considering the two major species in CNT synthesis, methane in hydrogen, and ask the question of how C and H elements are partitioned between different species under equilibrium conditions over a range of temperature, and as the molar ratio of H_2/CH_4 from 0 (pure methane environment) up to 1000 (very dilute methane environment).

Fig.3.1 shows how equilibrium compositions change as a function of temperature for different H_2/CH_4 ratios. Starting from zero H_2 (upper left), we have CH_4 pyrolysis, which yields increasing amounts of solid carbon C(s) and H_2 as temperature increases. With the

increase of H_2/CH_4 ratios, much of the carbon is converted into C(s), but the temperature where the conversion starts elevates from ~500 K for zero H_2 to ~1000 K for $H_2/CH_4 = 10$. In the current analysis, We define here the threshold temperature for conversion into of C(s) the point corresponding to 0.1 mol.% of C atoms converting into C(s).

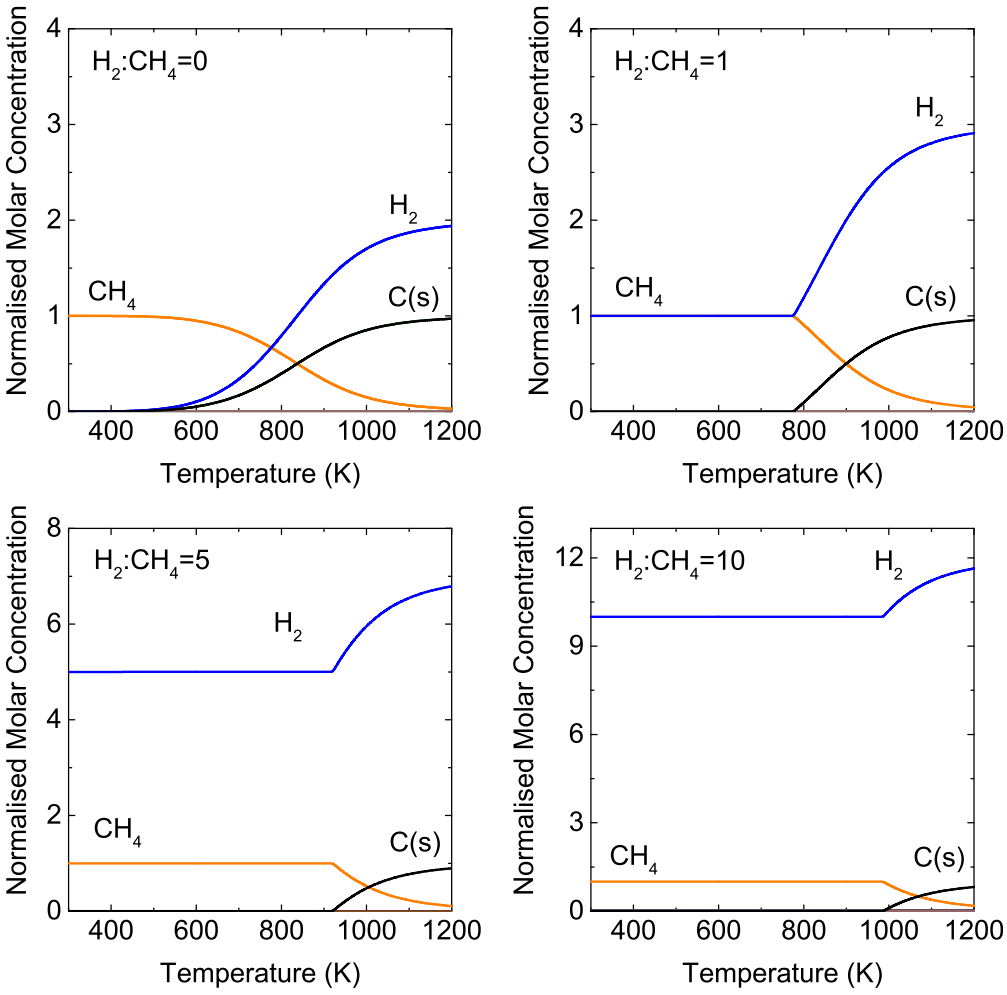

Fig. 3.1 Methane pyrolysis at different molar ratios of H_2/CH_4 from 0 to 10 between 300 K and 1200 K.

From Fig.3.2.(a), the threshold temperature for carbon conversion increases monotonically with H_2/CH_4 ratios, from 500 K at 0.01 (low dilution) to 1700 K at 800 (heavy dilution). This indicates that H_2 dilution in CH_4 acts as an inhibitor to the formation of C(s); beyond a ratio of 800, no C(s) is found within the temperature range considered. Fig.3.2.(b) shows the evolution of major species during thermal decomposition of methane for different H_2/CH_4 ratios. Conversion of CH_4 is primarily into C(s), but at higher H_2/CH_4 beyond 100, acetylene, C_2H_2(g), appears at temperatures around 1600–1800 K. This is a similar threshold

temperature found in combustion systems for soot to be formed. Studies on soot formation suggest that at temperatures above around 1500 K, acetylene becomes more stable than most of hydrocarbons [95]. Guéret *et al.* [81] observed a similar trend while performing equilibrium simulations for CH_4 pyrolysis at molar ratios of H_2/CH_4 between 0 and 2 over the temperature range from 673–2073 K (400–1800 °C) . In their simulations, which only considered gaseous species (and no C(s)), it was found that an increase in the H/C ratio (stronger dilution by hydrogen) resulted in a decreased level of methane decomposition, but a increased amount of acetylene at a given temperature. Furthermore, they found higher H/C ratios promoted the formation of acetylene and ethylene, while adversely affecting benzene formation. Experimental measurements of CNT formation find a lower conversion to C(s) than expected from equilibrium. This suggests that a significant energy barrier is likely to exist, which is possibly lowered by the use of catalysts.

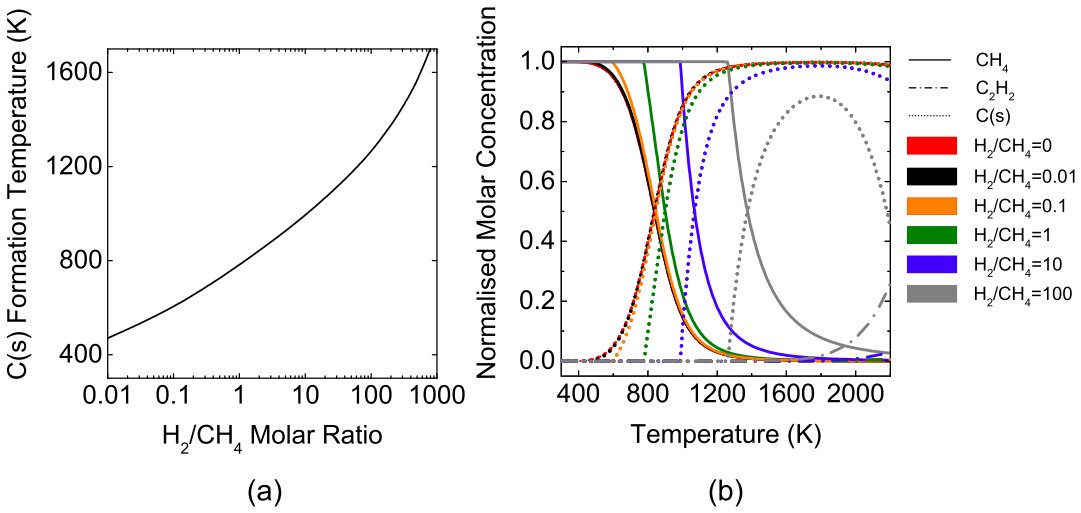

Fig. 3.2 Effects of H_2 dilution on thermal decomposition of CH_4: (a) threshold temperatures for carbon conversion as a function of H_2/CH_4 ratios, and (b) normalised molar concentration of major carbon-containing species, methane, acetylene and solid carbon, as a function of temperature for different H_2/CH_4 ratios.

A FCCVD furnace typically operates above 1273 K (1000 °C) and the reacting environment has H_2/CH_4 of ~10, as lower values lead to the formation of sooty carbon. The location of the operating point coincides with the transition from full conversion to C(s) towards the formation of acetylene. This may suggest that the process requires a particular type of acetylenic bond for building CNTs.

3.2.2 Elemental partition at the baseline condition

The input species are reformed under equilibrium, appearing as different species and in different phases as the temperature increases. The results are shown in Fig.3.3 for the baseline furnace stoichiometry listed in Table 2.1. The molar number of each element is normalised against that of iron, yielding the baseline stoichiometry at H:C:S:Fe = 45500:2000:8:1. Fig.3.3 illustrates the normalised elemental partition of C, Fe and S atoms at equilibrium on a molar basis between 300 K and 2200 K. To understand the plot, one may pick a specific temperature on a specific graph showing a molar distribution of element A (C, Fe or S), and draw a vertical line from the bottom x-axis to the top passing through one or several areas in different colours that correspond to various species. After that, one may find several points of intersection between the vertical line and the boundaries of the coloured areas. By measuring the vertical distance between the points of intersection within a specific coloured area (corresponding to a specific species), the molar fraction of element A which that specific species takes up can be determined accordingly.

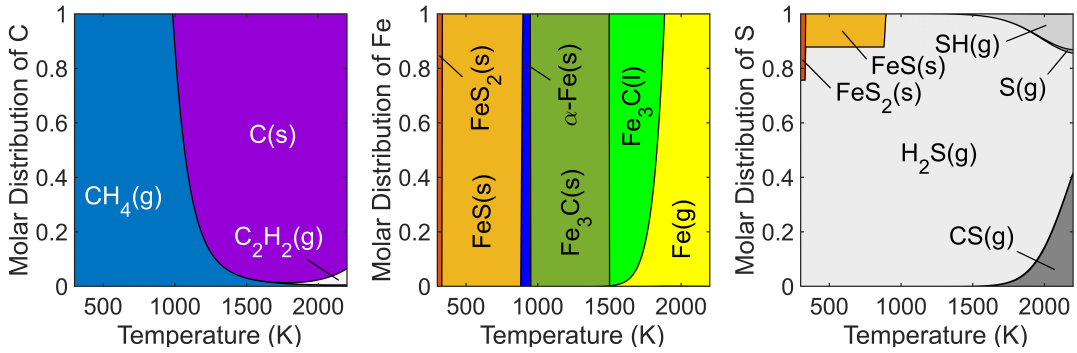

Fig. 3.3 Partition of C, Fe and S elements into their respective species between 300 K and 2200 K at the baseline condition (H:C:S:Fe = 45500:2000:8:1).

According to Fig.3.3, the input catalysts ferrocene and thiophene do not appear on plots as they are present in only very small concentrations in feedstocks and fall apart at low temperatures at equilibrium. It is seen that CH_4 is general thermodynamically stable at low temperatures up to around 1000 K. As the temperature increases, CH_4 is converted to C(s), up to about 1800 K, beyond which C_2H_2(g) starts to emerge. The rapid growth of C_2H_2(g) at higher temperatures beyond 1500 K is also observed in simulations by Guéret *et al.* [81]: higher temperatures allow the split of C-C bonds as well as C-H bonds, leading to the formation of triple bonds and hence giving rise to the appearance of acetylenic species.

Unlike the partition of carbon, the distribution of the iron-containing species over temperatures shows phase transitions taking place over very narrow temperature windows. At low

temperatures, solid iron sulphide, in the form of FeS_2(s) or FeS(s), is favoured. A transition over a narrow temperature boundary takes place at around 880 K away from FeS(s) and into solid α-Fe(s). The latter exists only between 880 K and 950 K before another transition takes place, and beyond 950 K, into solid iron carbide (cementite), Fe_3C(s). This species contains all of the iron at equilibrium up to 1490 K, at which it undergoes a phase change into liquid. This temperature coincides with a point where the metal vapour pressure for Fe increases significantly, representing nearly a quarter of the total number of moles of iron at 1800 K. From this temperature onwards, iron partitions from liquid Fe_3C(l) into vapour Fe(g) beyond 1880 K.

The equilibrium distribution of sulphur (S) is simpler: equilibrium drives it towards the acid gas hydrogen sulphide H_2S(g) over the whole temperature range. Solid iron sulphite FeS(s) appears up to around 880 K where Fe atoms partition into α-Fe(s). At higher temperatures, H_2S(g) prevails up to 1450 K where gaseous SH(g) and CS(g) emerge.

Within the typical synthesis temperature range of 1400–1750 K, thermodynamic equilibrium should drive the conversion of all carbon species into C(s), with minor contributions from some unsaturated hydrocarbons. Yet measurements show this is not the case, even for residence time of the order of seconds. Instead, only a fraction of the carbon in methane is extractable as soot or CNTs [52]. The process is helped by the addition of iron introduced as a catalyst in various forms, which is presumed to speed up the process of conversion from fuel to solid carbon. In combustion fields, iron-containing compounds, *e.g.* iron pentacarbonyl ($Fe(CO)_5$) and ferrocene, are used to suppress the formation of soot in flames [96]. With metal-containing species present in the mixtures, iron nanoparticles formed due to decomposition of iron-containing species are found to restrain the growth of polycyclic aromatic hydrocarbons (PAHs) which are key intermediates to soot formation. And the addition of iron into combustion makes the size of soot crystals smaller than that without. This makes soot particles less stable and more easily oxidised in the presence of oxygen [97]. In the present context, iron particles appearing beyond 1500 K may promote CNT formation via a carbide-like complex.

3.2.3 Effect of atomic ratios

In this section we consider the role of each element (S, Fe, C) separately, whilst keeping other proportions constant. In the following sections, we consider variations in sulphur, iron and carbon proportions, relatively to a baseline case, shown always as the second column in the corresponding figures.

3.2.3.1 Variable sulphur content

The ratio of S/Fe was varied over four different levels: 0.2, 8 (baseline), 20 and 100, based on values used in reports of successful CNT synthesis at S/Fe ratios between 0.2 and 20 [52, 98, 99, 94].

Fig.3.4 shows the partition of C, Fe and S elements as a function of the S/Fe ratio by varying the relative amount of S whilst the other atomic ratios fixed at H:C:Fe = 45500:2000:1. Each column, from left to right, corresponds to the S/Fe ratio of 0.2, 8 (baseline), 20 and 100, respectively, and each row, from top to bottom, represents the normalised partition plots of C, Fe and S elements, respectively.

It is clear from the top row that the varying S/Fe ratio has a negligible effect on the elemental distribution profile of carbon atoms, except for a small amount of gas phase CS(g) which appears beyond 1800 K at S/Fe = 100.

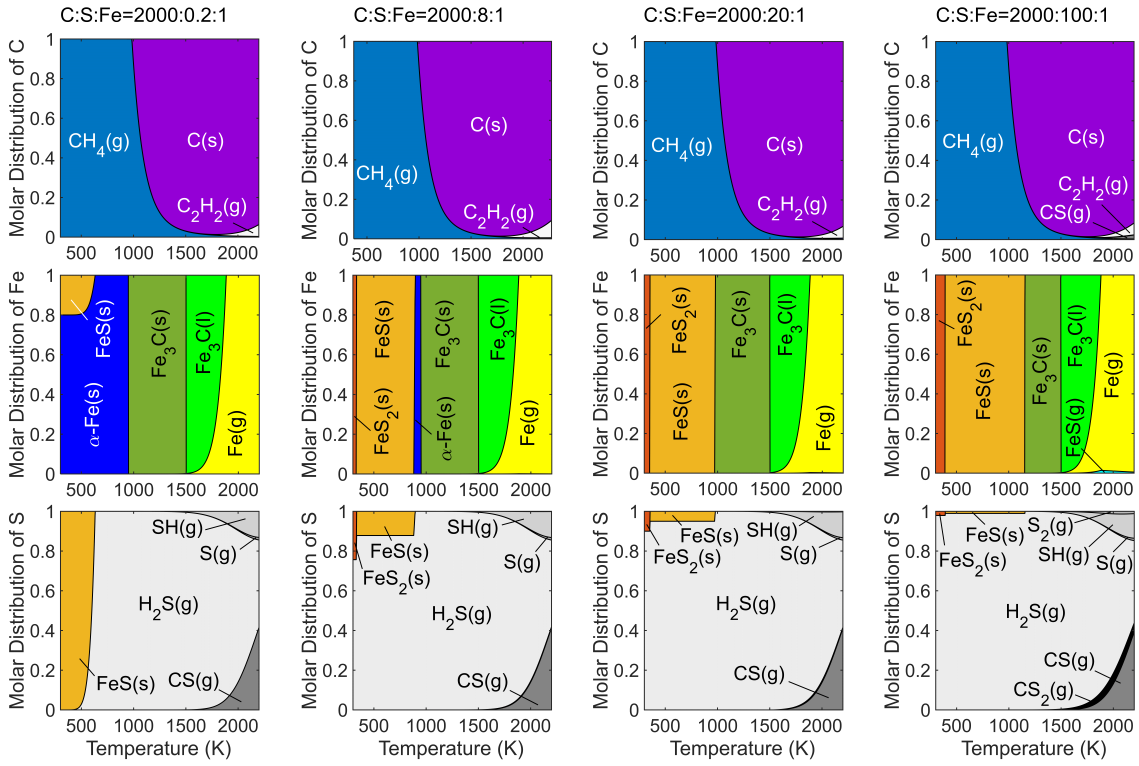

Fig. 3.4 Partition of C, Fe and S elements as a function of varying amounts of S at H:C:Fe = 45500:2000:1, between 300 K and 2200 K. Each column, from left to right, corresponds to the S/Fe ratio of 0.2, 8(baseline), 20 and 100, respectively, and each row, from top to bottom, represents the normalised partition plots of carbon, iron and sulphur elements, respectively.

The middle row shows that the increasing amount of sulphur lead to the suppression of α-Fe(s) formation, in exchange for a wider temperature range within which solid iron sulphides, FeS_2(s) and FeS(s), can exist prior to conversion into Fe_3C(s).

The bottom row shows only little change as a function of sulphur content beyond 1500 K: most S atoms end up as H_2S(g), with conversion primarily into gaseous species of CS(g) and SH(g) beyond that temperature. Some conversion of S into CS_2(g) and S_2(g) can be seen at the highest S/Fe ratios.

Solid iron sulphide compounds, FeS_2(s) and FeS(s), fractions are affected at low temperatures and up to a certain threshold temperature, which increases with the S/Fe ratio. The fraction of S taken up by by FeS_2(s) or FeS(s) decreases with sulphur content. From a thermodynamic perspective, S atoms favour bonding with iron atoms to form iron sulphides first, and after all available iron atoms are consumed, the remaining S atoms are converted into H_2S(g).

Current calculations do not incorporate thermodynamic data for potential non-ideal solubility of the various phases in the liquid or solid forms, and further calculations incorporating these distinctions, for the Fe-C-S system based on the data from [100] may further extend the analysis.

3.2.3.2 Variable iron content

We now consider the case where the relative amount of iron is varied, whilst the other proportions are fixed at H:C:S = 45500:2000:8, corresponding to S/Fe of 0.2, 8.0 (baseline), 20, and 100. The results are summarised in Fig.3.5. The plots are organised in a similar way as Fig.3.4.

Similarly to the discussion of methane pyrolysis in Section 3.2.1, the partition of carbon atoms for the thermal decomposition of methane in a hydrogen atmosphere is primarily determined by H_2/CH_4 ratios, and is therefore not affected much by the change of the relative amount of Fe (top row). The change in the sulphur partition map with increasing S/Fe ratios also resembles their counterpart on the bottom row in Fig.3.4.

The partition of Fe (middle row) can be compared to the corresponding plot in Fig.3.4: for increasing proportions of Fe (from the rightmost to the leftmost column), α-Fe(s) can exist up to around 1000 K for all cases. Further, the temperature range within which liquid Fe_3C(l) exists becomes wider given an increasing iron content (towards the left), so that and liquid iron, Fe(l), appears for the highest iron content on the leftmost column (C:S:Fe = 2000:8:40). The overabundance of iron allows for the saturation of the Fe_3C phase, thus allowing some of the excess Fe to precipitate in liquid form beyond about 2000 K.

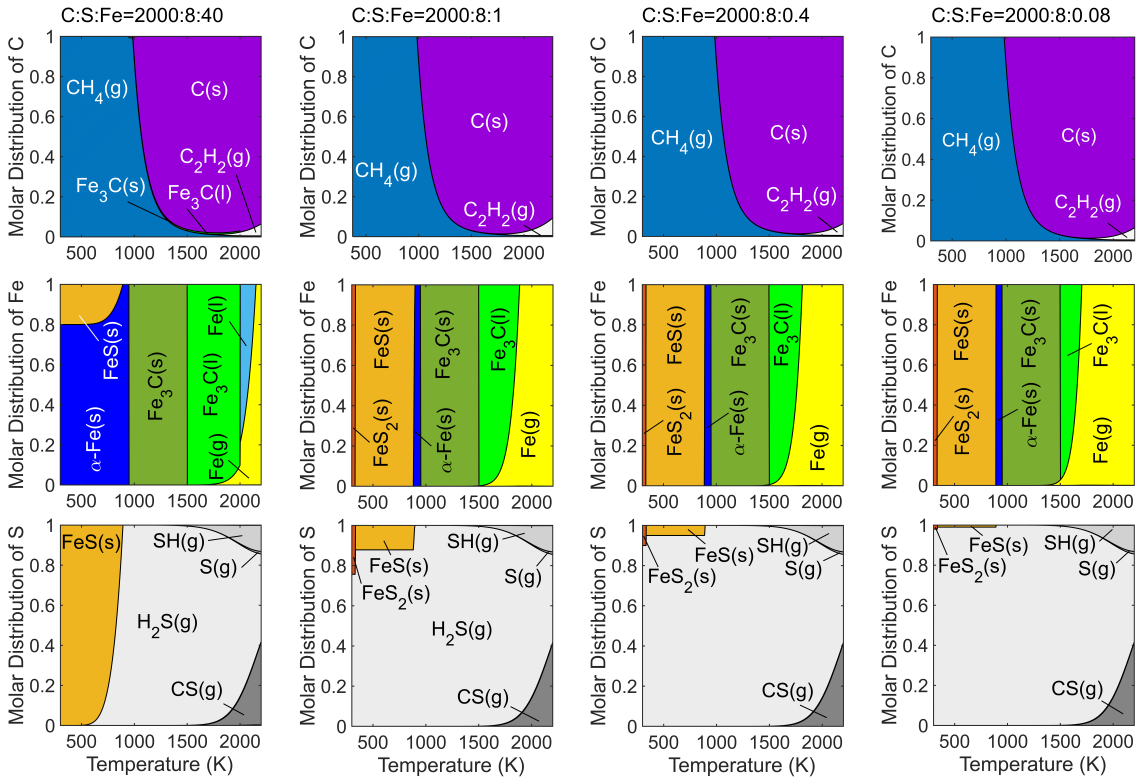

Fig. 3.5 Partition of C, Fe and S elements as a function of varying amount of Fe at H:C:S = 45500:2000:8, between 300 K and 2200 K. Each column, from left to right, corresponds to the S/Fe ratio of 0.2, 8 (baseline), 20 and 100, respectively, and each row, from top to bottom, represents the normalised partition plots of carbon, iron and sulphur elements, respectively. Notice that the changing variable, Fe, is *decreasing* from left to right in this case.

3.2.3.3 Variable carbon content

Finally, we vary the abundance of carbon relatively to the other elements, whilst keeping the ratio of H:S:Fe fixed at 45500:8:1. The results are summarised in Fig.3.6.

The main difference in the carbon partition (top row) is that as the ratio of C/H decreases (towards the left most columns), more of the carbon is converted into C_2H_2(g) at increasing temperatures rather than C(s). In addition, the thermal decomposition temperature for CH_4 and the maximum fraction of C atoms that convert into C(s) both decrease with increasing amount of carbon. This results from the direct change in the ratio of H/C, as discussed in Section 3.2.1.

The partition of Fe is unaffected by the change in carbon at high temperatures ($T > 1200$ K), but differences can be seen at the lower. The lowest temperature for solid Fe_3C(s) to form decreases with the increase of the amount of carbon, and this temperature appears to

coincide with the threshold decomposition temperature of CH_4. Hence, it can be deducted that Fe atoms are inclined to bond with C atoms to form solid iron carbide once C atoms become available. The lowest temperature for α-Fe(s) to form is found to be unchanged with the changing proportion of carbon, but α-Fe(s) vanishes for C/Fe proportions between 2000 and 5000 in favour of Fe_3C.

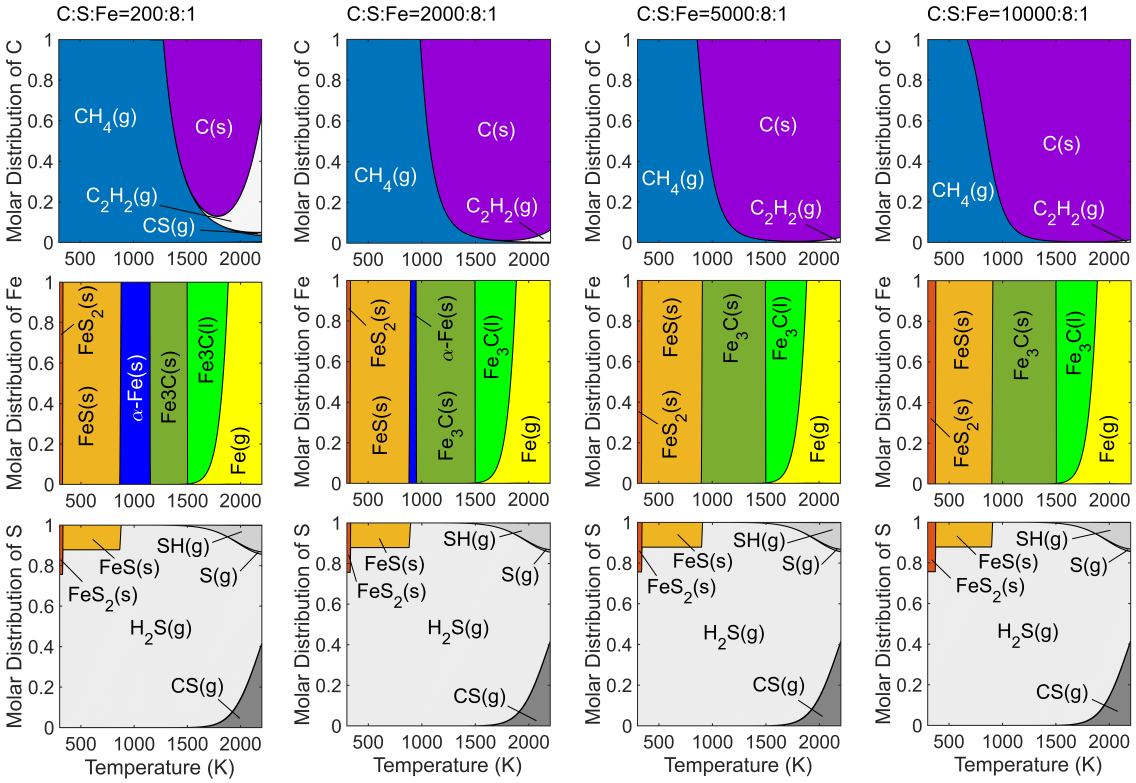

Fig. 3.6 Partition of C, Fe and S elements as a function of varying amount of C at H:S:Fe = 45500:8:1, between 300 K and 2200 K. Each column, from left to right, corresponds to the C/Fe ratio of 200, 2000(baseline), 5000 and 10000, respectively, and each row, from top to bottom, represents the normalised partition plots of carbon, iron and sulphur elements, respectively.

The partition profile of S is almost unchanged for all carbon proportions. By comparing with Fig.3.4 and Fig.3.5, it can be deduced that the upper limit temperature for solid FeS(s) to exist is only affected by the relative amount of sulphur, *i.e.* it elevates with the increase of the S/H ratio. This trend agrees with the experimental results and the theoretical predictions by Gspann *et al.*[52], which suggests that a higher S/H ratio leads to a higher temperature at which H_2(g) starts to extract S atoms from FeS(s) to form H_2S(g).

3.2.4 C-Fe-S ternary diagrams

The previous sections illustrate variations of equilibrium compositions as a function of temperature at the selected stoichiometries. However, a more familiar diagram for material scientists are diagrams that show how the condensed species (solid and liquid) appear in equilibrium at a fixed temperature, as a function of relative atomic abundance. Ternary diagrams have been traditionally used for the purpose [79]: for a fixed temperature, and three different atomic species, the equilibrium diagram offers the phase and species composition across the range of stoichiometries considered in the form of a triangular cross section. A point lying within this triangular coordinate system corresponds to a specific composition consisting of the three components–C, Fe and S in our case–with different proportions. The proportion of each component at any point within the triangle must sum up to a constant (normalised to unity in the present case). One of the commonly applied methods is the altitude rule where one can draw a vertical line from the point of interest down to the baseline edge opposite to the corner of the triangle corresponding to the element of interest. The ratio of the length of this line to the altitude of the triangle represents the proportion of the element of interest at this point.

Fig.3.7 shows the distribution of various condensed phases at three typical furnace temperatures as a function of varying amounts of C, Fe and S. The equilibrium calculations were performed at hydrogen atmosphere where the molar fraction of hydrogen atoms was kept fixed at 96 mol%, consistent with the baseline condition (see Table 2.1), while the molar fraction of C, Fe and S elements varies. Each letter represents a specific species, and uppercase and lowercase letters indicate solid and liquid phases, respectively.

From the previous sections, one expects the existence of four condensed-phase species at equilibrium in the range of 1373–1573 K, namely Fe_3C, γ-Fe, FeS and C(s). To be specific, the four condensed species are all in solid phase at 1373 K, while a change of phase from solid into liquid for FeS and Fe_3C can been seen at 1473 K and 1573 K, respectively. These species may exist on their own, except for C(s), or coexist at certain areas in the ternary diagram. Typical conditions for making CNTs usually lie at the lower right corner of the ternary diagram *i.e.* large carbon supply with minor input of sulphur and iron as catalysts. As a result, one expects simultaneous formation of both Fe_3C and C(s) if equilibrium is reached. Experiments have also identified the presence of γ-Fe(s) during CNT fibre formation [101–103], indicating that some locally iron-rich sites, corresponding to the areas at the upper corner of the triangle, may present as reactants in regions where the reacting flow is inhomogeneously distributed. Solid carbon, C(s), is found to coexist with either FeS or Fe_3C or both rather than with γ-Fe(s) at equilibrium over the temperature considered according to Fig.3.7, whilst γ-Fe(s) is present with Fe_3C or FeS, or both. As temperature increases,

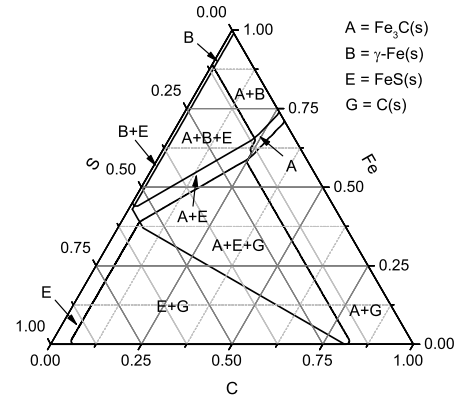

(a) 1373 K

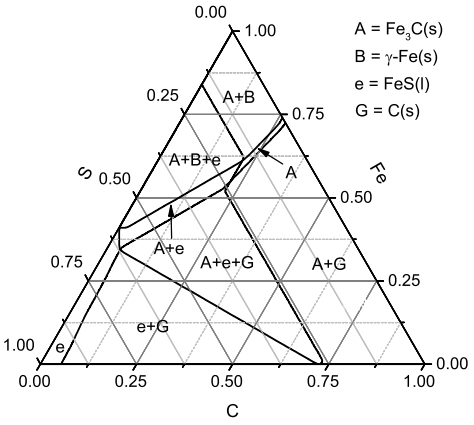

(b) 1473 K

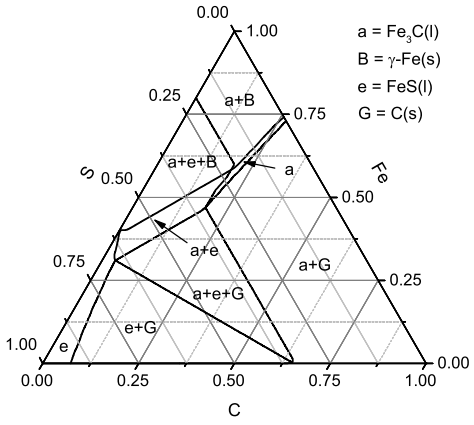

(c) 1573 K

Fig. 3.7 Distribution of condensed phases at equilibrium over varying proportions of C, Fe and S normalised to unity in a mixture consisting of 96 mol% H atoms at 1373 K, 1473 K and 1573 K (from top to bottom). The legend identifies each species and corresponding phase. Lowercase and uppercase letters correspond to liquid the solid phase, respectively.

the distribution pattern of the condensed phase species does not change much except for the phase change for both FeS and Fe_3C. The area where FeS exists shrinks markedly with temperature compared with other species, which results in an increased coexisting area for Fe_3C and C(s) as well as Fe_3C and γ-Fe.

3.2.5 Carbon nanotubes

The state of aggregation of carbon structures or the formation of carbon allotropes may change the thermodynamic properties of solid carbon to some extent. In this section we examine the expected differences in thermodynamic properties between CNTs and graphite.

Table 3.1 summarises the thermodynamic properties of different types of CNTs synthesised via various routes. According to the table, the standard enthalpy of formation at 298 K, Δh_f^0, is in general of the order of 10 kJ mol^{-1}, while the standard entropy of formation, Δs_f^0, is on average below 10 J mol^{-1} K^{-1}. Thermodynamic data for CNTs in literature are rather scarce, and the governing factors that determine the thermodynamic properties of CNTs have yet to be systematically investigated. However, Table 3.1 indicates that the estimates for Δh_f^0 and Δs_f^0 of CNTs produced by a variety of methods are relatively similar. Moreover, the estimated Gibbs free energies of CNTs are all higher than those of graphite, indicating that graphite is in general thermodynamically more favoured at room temperature and atmospheric pressure.

Table 3.1 Thermodynamic properties of carbon nanotubes

Samples	Structure	Catalysts	Δh_f^0 (kJ mol^{-1})	Δs_f^0 (J mol^{-1} K^{-1})
Gozzi [104]	SWCNTs, un-bundled	Cheap Tube (Brattleboro, VT)	9.5 ± 0.4	n/a
Levchenko [105]	SWCNTs, bundles of (10,10)	graphite, Ni/Co	7.0 ± 1	5.9
Gozzi [106]	MWCNTs, herringbone	CH_4, $NdNi_5$	9.0 ± 0.8	17.46 ± 0.09
Kabo [107]	MWCNTs, herringbone	hydrocarbon gas, Ni(NiO)/MgO	0.6 ± 0.9	6.225 ± 0.025
Cherkasov [108]	MWCNTs, herringbone	benzene,nickel(II) acetylacetonate	21.70 ± 1.32	n/a
Cherkasov [108]	MWCNTs, cylindrical	benzene, ferrocene	8.60 ± 0.52	n/a
Suslova [109]	MWCNTs, cylindrical	C_6H_14 and CH_3CN, Co/Mo-MgO	9.45 ± 0.01	n/a
Graphite [82]	planar layer	n/a	0	5.74

The specific heat capacity c_p^0 also needs to be estimated for the equilibrium calculations. Most of the current studies focus on low-temperature regions (below 298 K) [110–113], while only a few studies have considered the high-temperature behaviours [114, 107]. A theoretical study by Li *et al.* [115] suggests that c_p^0 of CNTs is primarily dependent on temperature, and only a weak function of chirality and tube length at high temperatures.They also found that tube diameter or the number of layers consisting of a nanotube has negligible influence on c_p^0. One theoretical study on CNTs predicted that c_p^0 of CNTs and graphite are indistinguishable beyond room temperature [116], and a series of experimental studies on CNTs by Pradhan *et al.* [112] showed that the c_p^0 of multi-walled CNTs (MWCNTs) and single-walled CNTs (SWCNTs) with different orientations were within 7% of those of graphite powder. Kabo *et al.* [107] used an adiabatic calorimeter to determine that the ratio of heat capacity of MWCNTs to graphite was 1.03 between 300 K and 370 K, and predicted that the specific heat capacity of MWCNTs resembles that of graphite beyond 370 K. On the grounds of these findings, we thus assumed the c_p^0 of CNTs and graphite the same within the range of temperatures considered. A complete picture of Gibbs free energy, g^0, of different CNTs can therefore be calculated accordingly from the coefficients shown in Table 3.1.

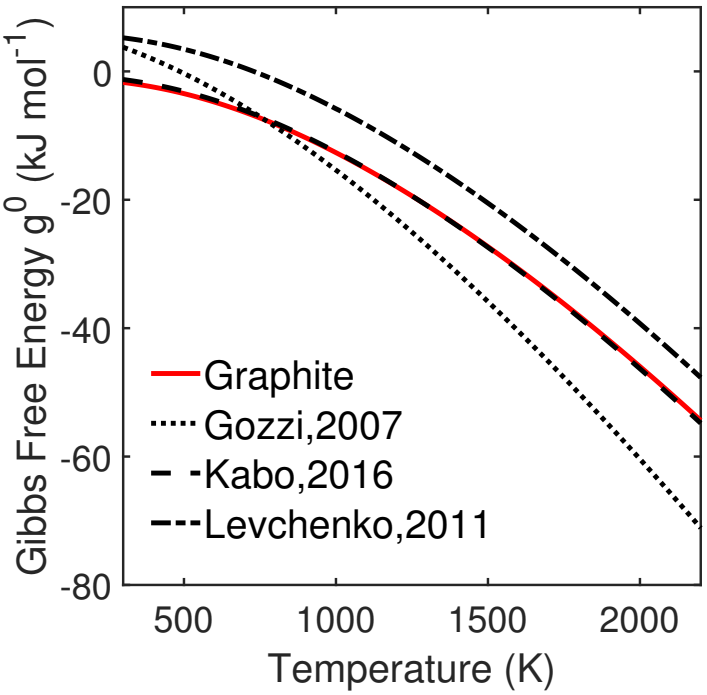

Fig. 3.8 Gibbs free energy g^0 of different CNTs and graphite between 300 K and 2200 K. Solid red line represents graphite [82], and dotted, dashed and dash-dot lines represent the CNTs by Gozzi [106], Kabo [107] and Levchenko [105], respectively.

Fig.3.8 illustrates the variation of Gibbs free energy g^0 of CNTs calculated from 3 different sources listed on Table 3.1, in comparison with graphite [82], between 300 K and 2200 K. The values for g^0 by Kabo *et al.*'s data [107] resemble most closely to those of graphite, whilst those from Gozzi *et al.* [106] deviate further, decreasing at a faster rate with temperature, and crossing over the value for graphite at around 750 K. These values are consistent with experimental results by Gozzi [106], where a spontaneous transformation from graphite to CNTs was found at $T > 704 \pm 13$ K. Values of g^0 measured by Levchenko *et al.* [105] look similar to those of graphite due to the negligible difference in Δs_f^0 (0.16 J mol^{-1} K^{-1}), but are in general higher than those of graphite by Δh_f^0 (7 kJ mol^{-1}).

Although CNTs demonstrate remarkable mechanical and electrical properties due to their regularity, thermodynamic properties are not very different to those of graphite based on what the figure illustrates. The use of graphite as a representation of all the graphitic carbon alltropes in our simulations is hence a reasonable and justified way to study the species partitions at equilibrium which has also been applied in other studies under the same assumption [78, 77]. A sensitivity analysis is provided at the following section to illustrate the limited changes due to the inclusion of CNTs in the equilibrium calculations.

3.2.6 Discussion

The existence of cementite phase, Fe_3C, and its role on CNT formation have been widely discussed in literature [101, 117, 103]. Yoshida *et al.* [117] reported that they had successfully observed CNT nucleation and growth on Fe_3C nanoparticles whilst using a CVD method with acetylene as the carbon source. These findings obtained by using *in situ* transmission electron microscopy (TEM), suggests that Fe_3C nanoparticles act as active catalytic sites through which carbon atoms diffuse to initiate CNT growth. Similarly, He *et al.* [103] observed the growth of CNTs on both α-Fe and Fe_3C nanoparticles in a plasma-enhanced CVD reactor. They reported that at 873 K (600 °C) only carbon nanofibres (CNFs) were observed on α-Fe and Fe_3C nanoparticles, whereas when temperatures increased beyond 923 K (650 °C), these nanoparticles became activated, and CNT growth was hence observed. In addition, they found that the growth rate of CNTs was higher on α-Fe nanoparticles than on Fe_3C, and attributed the observation to the higher diffusion rate of carbon atoms across the solid α-Fe nanoparticles and larger catalytic area.

Two curious coincidences appear at the temperature threshold where the CNT formation processes typically become possible: (a) the transition from the solid to liquid Fe_3C, and (b) the appearance of substantial iron vapour Fe(g), both around 1500 K. The transition suggests that the availability of the mobile phases may facilitate the process of reforming the hydrocarbons from the original C-H bonds into patterns more conductible to CNT

formation. Scanning electron microscope (SEM) images [118, 119] and energy dispersive X-ray spectroscopy (EDX) analysis [120] have shown that CNT fibres show iron-containing particles at the end or top of the fibres. This suggests that the transition from solid to liquid carbide could initiate the connection between the growth of CNTs towards the equilibration of the C(s) along the fibres. The study by Schaper *et al.* [121] supports the conjecture, as they observed an existence of quasi-liquid catalyst particles using TEM. They reported that carbon-saturated metallic nanoparticles melted just above 1133 K (860 °C), which is well below the bulk material melting point of either iron metal or carbide. It is hypothesised that iron carbide becomes supersaturated during CNT growth and acts as an intermediate that promotes the diffusion of C atoms into catalyst nanoparticles, thus helping well-ordered graphene layers to continuously segregate from catalytic surfaces.

The role of sulphur in CNT synthesis has also been widely studied, and a common understanding of its role is as a contaminant that reduces catalytic activity of most transition metals, even at very small concentrations [52, 122]. Such a poisoning effect is found to be beneficial for CNT nucleation and growth, as it may help promote the diffusion of C atoms through the surface of Fe nanoparticles as well as the assembly of C atoms onto graphene layers [49]. According to our simulation results, iron sulphide compounds, FeS_2(s) and FeS(s), are found from room temperature up to a certain point determined by S/H ratios, as discussed in Section 3.2.3.3. At lower temperatures, S atoms combine with available Fe to form iron sulphide solids preferably to other products, as shown in Fig.3.4 and Fig.3.5. Fig.3.7 also shows that FeS(s) occupies the majority of the triangle, and while leaving a smaller patch on the right containing no sulphides. As the temperature increases, FeS loses ground to Fe_3C, as shown in Fig.3.7.

3.2.6.1 Effect of carrier gases

The previous sections have discussed the effects of the stoichiometry around the range relevant for CNT formation. However, the nature of the furnace carrier gases may also play a critical role in the synthesis. Although most successful syntheses have been carried our in hydrogen atmosphere, recent studies suggest that the FCCVD process may also be performed using N_2 [46–48] or Ar [123] as the buffer gas. Such a result would indeed make the whole process significantly less expensive, as inert gases are much safer than hydrogen.

The simulations were carried out based at the baseline stoichiometry (H:C:S:Fe = 8000:2000:8:1) as indicated on Table 2.1, where H atoms originate only from the carbon source CH_4 and catalysts, thiophene and ferrocene. The molar fraction of H_2 originally used in a typical FCCVD reactor at the baseline stoichiometry was replaced by the same amount of inert gas, argon or nitrogen. The equilibrium results are summarised in Fig.3.9. These

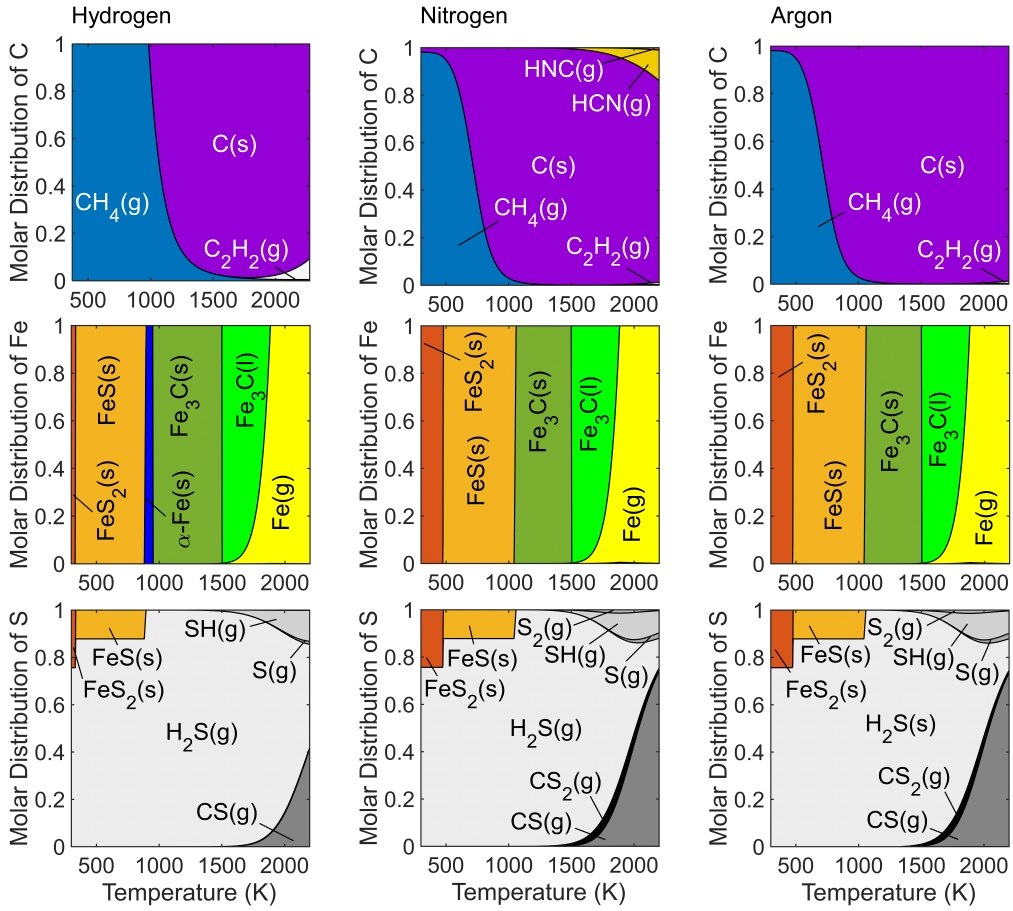

Fig. 3.9 Partition of C, Fe and S elements at the baseline stoichiometry of C:S:Fe = 2000:8:1 for different carrier gases. Left: hydrogen, middle: nitrogen and right: argon.

plots are arranged such that each column represents the partition of elements for each carrier gas, (left to right: H_2, N_2 and Ar) and each row shows how the elemental partition of C, Fe and S atoms from top to bottom, respectively.

The replacement of H_2 for inert gases significantly lowers the temperature at which CH_4 conversion into C(s) is favoured: as low as 300 K for Ar and N_2, compared with 1000 K for the original case with H_2. Given the lack of molecular H_2, it is not surprising that hardly any C_2H_2(g) is formed at high temperatures.

In addition, very high temperatures can also lead to thermal breakdown of N_2 into HNC(g) and HCN(g) as shown in the carbon partition plot for the N_2 case. In general, there are no substantial differences between the Fe and S partition maps compared to that for H_2; except that FeS(s) can survive at a higher temperature in either N_2 or argon environment at ~1000 K

while lower in H_2 at below 900 K. This leads to an absence of α-Fe(s) in Fe partition maps for both N_2 and Ar cases.

The lack of sensitivity to the bath gas under equilibrium conditions, compared to the experimental findings that the presence of hydrogen gas is necessary suggests that there may be kinetic effects at work. On the other hand, the experiments with nitrogen as a carrier gas remain to be reproduced by other laboratories, so perhaps there are additional unaccounted for effects that may also need to be properly discovered.

3.2.6.2 CNT property sensitivity analysis

In Section 3.2.5, we discussed the relatively small differences in Gibbs free energy between graphitic carbon and estimates for CNTs. Here we consider a sensitivity analysis to understand the effect of these different properties. The analysis was carried out at the baseline condition shown in Table 2.1, and graphite used to represent all carbon solid products was replaced by different CNTs. Based on the results, we find that the partition plot of Fe and S elements are hardly affected, while minor differences are found in the C partition plot.

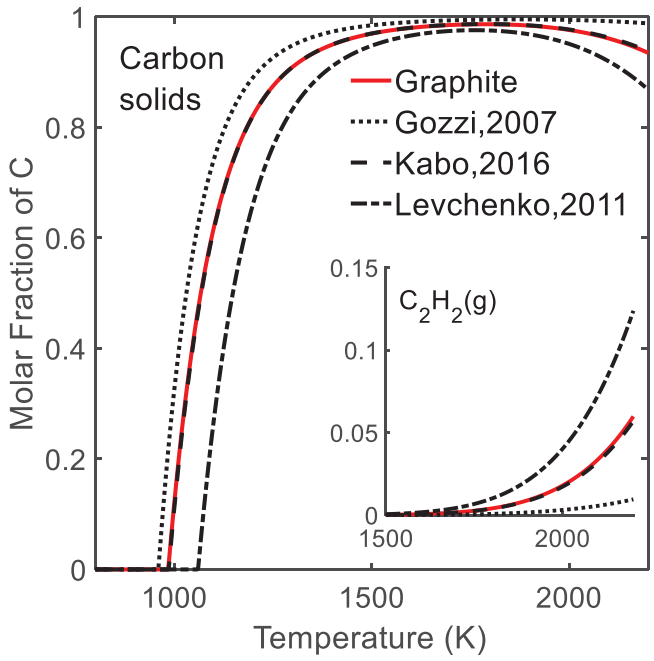

Fig. 3.10 Partition of C element into carbon solids (graphite or CNTs) and C_2H_2(g) as a function of temperature, at the baseline condition (H:C:S:Fe = 45500:2000:8:1). Solid red line represents graphite [82], and dotted, dashed and dash-dot lines represent CNTs by Gozzi [106], Kabo [107] and Levchenko [105], respectively.

Fig.3.10 illustrates the observed differences in the elemental partition of carbon into its major species, carbon solids C(s) and C_2H_2(g), among various graphitic carbon structures.

Generally, all carbon solid products start to form at around 1000 K and reach their maximum molar fractions at around 1800 K before decomposing into C_2H_2(g). C_2H_2(g) starts to appear as a major C-containing species at around 1500 K, and its occupation of carbon increases with temperature. The property estimates of CNT by Kabo [107] mostly resemble graphite as the formation curves for carbon solids, and the simulation results are identical to those of graphite. The values for properties obtained for CNTs by Gozzi [106] has the lowest Gibbs free energy values, and the corresponding molar fractions are therefore highest compared with other carbon sources. By referring to Fig.3.8, it is found that the g^0 values by Gozzi cross over that of graphite at around 750 K, and from that point onwards, the CNTs show lower g^0 than graphite. Hence these CNT structures become more thermodynamically favourable than graphite as the temperature increases, leading to a lower formation temperature and a higher molar fraction of C atoms compared with other carbon sources. The use of the values by Levchenko [105], on the other hand, leads to a higher threshold temperature compared with graphite. According to Fig.3.8, the g^0 of the CNTs by Levchenko is in general higher than that of graphite, 7 kJ mol^{-1} apart, due to a difference in $\Delta h_f^0 = 7$ kJ mol^{-1} at 298 K and a negligible difference in Δs_f^0 between the two.

Despite minor differences found in the carbon partition map, CNTs and graphite exhibit strong similarity in thermodynamic properties, which, as a result, makes the other elemental partition maps of Fe and S atoms hardly affected for various graphitic structures. Allowing for all forms of carbon structures in calculations leads to corresponding mixtures of graphite or types of CNTs according to their lowest equilibrium free energies, as also reported in [77]. Hence equilibrium predictions would predict that either CNTs or graphite will prevail at a given temperature, rather than coexist at certain temperatures at equilibrium in our predictions.

3.2.7 Summary

Thermodynamic equilibrium calculations have been carried out to study partition of elements over a range of stoichiometries under conditions similar to those in furnaces generating CNTs via a FCCVD method. The carbon atoms convert from CH_4 into C(s), represented by graphite, with small quantities of C_2H_2(g) at temperatures beyond 1600 K and high H/C ratios. A maximum conversion into C(s) is possible at around 1800 K for all stoichiometries considered. The temperatures at which conversion from CH_4(g) to C(s) is possible varies from 300 to 1600 K over the range considered, increasing with a power of the H/C ratio.

The partition map for Fe element reveals that at furnace temperatures between 1400 K and 1800 K, iron carbide (Fe_3C) is the main iron-containing species both in solid and liquid phases, followed by iron vapour Fe(g) at higher temperatures. Below these temperatures, Fe

atoms are thermally driven into solid iron sulphides FeS_2(s) and FeS(s), as well as α-Fe(s) for higher values of Fe/S. Sulfur partition is driven mostly towards H_2S(g) over the whole temperature range, with gaseous SH(g) and CS(g) emerging beyond 1450 K, and solid iron sulphides below 900 K. Experimental observations confirm the existence of these species in practical studies.

The species distribution for Fe and S elements within the typical furnace temperature region are not significantly affected by changing the baseline stoichiometry. Higher Fe/C ratios affect the presence or not of liquid Fe, and the S/H ratio mainly affects the highest temperature at which for FeS(s) exists.

Ternary diagrams of C, S and Fe elements at furnace temperatures between 1373 K and 1573 K reveal that only four condensed species, Fe_3C, γ-Fe, FeS and C(s), are expected to exist over different proportions of the three elements. All these species are in solid phase at 1373 K, while a change of phase from solid into liquid in FeS and Fe3C is seen at 1473 K and 1573 K, respectively. The operation conditions for making CNTs are located at the carbon-rich corner, which corresponds to the area where Fe_3C and C(s) coexist.

Replacement of H_2 by inert gases N_2 or argon, only lowers the threshold temperature for C(s) to form, reducing it from 1000 K in H_2 all the way down to 300 K for inert gases. Expected species and phase distributions for Fe and S elements are, not significantly affected at furnace temperatures.

A sensitivity analysis for different assumed properties of CNTs relatively to graphite shows small differences in the elemental partition for carbon, despite slight deviations of the formation temperature for CNTs from that of graphite. The distributions of Fe and S elements are not affected due to the strong similarity in thermodynamic properties between CNTs and graphite.

Comparisons between the calculated equilibrium distributions and observed products from FCCVD suggest that there are both significant differences and similarities between equilibrium findings and the relatively sparse and anecdotal observations. Clearly there is no full conversion between the source carbon and CNTs or graphite in practical systems, so the actual systems are far from equilibrium. On the other hand, the temperatures required for conversion from fuel to CNTs coincide with the transition temperature where Fe_3C becomes liquid, and vapour Fe(g) (and in some cases, Fe(l)) becomes available, which agrees with measurements of the availability of such species in sample CNT fibres and reactor walls.

It is of course clear that equilibrium studies cannot fully explain the complex mechanisms in CNT synthesis, and there is a need for kinetic studies to create a fully quantitative understanding the process. Nevertheless, equilibrium calculations provide the limit and ther-

modynamic direction of the processes, and are therefore useful signposts in the development of a more comprehensive theory.

3.3 C-H-Fe-S-O system

The previous section has studied the thermodynamic equilibrium of the system containing C, H, Fe and S elements, while there exist many cases where oxygen presents in CNT synthesis. Oxygen prevails in flame synthesis of CNTs and can originate from various sources including O_2, H_2O and carbon sources like ethanol. In a CVD synthesis the presence of oxygen is usually bound to carbon sources such as ethanol [34, 124, 42, 125] and isopropyl alcohol (IPA) [126]. Our primary objective is to understand the role of oxygen in the synthesis, and we start with an typical operating condition using ethanol as the carbon and oxygen source.

Table 3.2 summarises the experimental conditions used in a FCCVD method to produce CNTs from ethanol, which again uses ferrocene and thiophene as the catalyst precursors. Although various amounts of ferrocene and thiophene were used for CNT production, a similar range of proportions between the two precursors appears to have been used, typically between 0.2 wt.% and 4.0 wt.%. By converting this range into a molar ratio of sulphur to iron elements, S/Fe, the ratio was found to fall into the range of between 0.1 and 15. However according to literature, the S/Fe ratio that was most commonly practised at around 1.5, as specifically suggested by Motta *et al.* [49]. The injection rate of the feedstock for most of the studies varied from 5 up to 30 ml/hr, except for the work by Wang [46] who used an order of magnitude higher flow rate than the rest of the studies (120-600 ml/hr). The carrier gas is usually H_2, with flow rates typically ranges from 0.4 to 1.5 slpm, depending on the size of reactors. An exception again is the case by Wang *et al.* [46], which used N_2. The furnace temperature for these cases was maintained in the range between 1050 °C and 1300 °C.

Based on the above conditions, we perform equilibrium calculations with similar atomic ratios starting from H:C:O:S:Fe = 4500:550:270:1.5:1, and the sensitivity analysis is also considered based on this standard condition.

3.3.1 Ethanol pyrolysis in hydrogen

We first consider the pyrolysis of ethanol in a H_2 atmosphere, similar to the study of the pyrolysis of methane in the previous section as shown in Fig.3.1. Fig.3.11 presents the variation of the normalised number of moles of different species as a function of temperature between 1000 K and 2000 K, the range of interest, for the ethanol pyrolysis. The normalisation is performed with respect to the total amount of carbon atoms in the system. The

Table 3.2 Studies of FCCVD synthesis using ethanol, ferrocene and thiophene for CNT production.

Literature	Ferrocene (wt.%)	Thiophene (wt.%)	Injection rate (ml/hr)	Carrier flow rate (slpm)	T_f (°C)
Li [34]	0.23-2.3	1.0-4.0	5-15	0.4-0.8	1050-1200
Li [42]	0.25-2.5	0.5-2.5	5-30	0.4-1.5	800-1200
Motta [49]	2.3	1.5	7.5	0.5	1200-1300
Wang* [46]	-	-	120-600	0.3-0.5 (N_2)	1150-1300
Hoecker [94]	1.3	8.0	8	1.4	1300

* No data provided for ferrocene and thiophone.

results for different molar ratios of $\frac{H_2}{C_2H_5OH}$ from 0 (no H_2) to 100 are summarised in the figure, corresponding to Fig.3.11 (a)-(f), respectively. The ratio of $\frac{H_2}{C_2H_5OH}$ represents the initial molar ratios of the two species, as the input. The atoms coming from these species recombine and form different species based the given temperatures. H_2 is not shown, as it is the diluent species.

The results show that the species convert into H_2O, CH_4, CO (and H_2) and the graphitic carbon C(s) are the primary equilibrium species between 1000 K and 2000 K. Ethanol is not sufficiently stable at these temperatures, and does not appear as an equilibrium product. Minor species such as elemental H and C_2H_2 become visible at $\frac{H_2}{C_2H_5OH} > 10$ and high temperatures. Increasing H/C ratios naturally lead to a lower level of C(s) as a product. Instead C_2H_2 is favoured at higher temperatures, making up an increased fraction of the C atoms as $\frac{H_2}{C_2H_5OH}$ increases. Moreover the minimal temperature at which C(s) reaches 0.5 increases with elevated H_2 levels. The inset in Fig.3.1(a) shows the behaviour at lower temperatures, where C(s) starts to form and reach 0.5 at 700 K before achieving its maximum value (around 0.6) at 900 K. It then gradually decreases to 0.5 and remains fairly unchanged with the increase of temperatures. One can observe a similar trend for C(s) in the inserted plot in Fig.3.1.(b), but its peak value at 900 K slightly decreases to around 0.55 due to the increased H_2 level. Such a trend eventually disappears when $\frac{H_2}{C_2H_5OH}$ reaches 5, and a monotonic increase of C(s) can be observed at this ratio and beyond. The decrease of the quantity of C(s) from 900 to 1100 K in Fig.3.1.(a) and (b) is due to the rapid increase in CO in this range where CO competes with C(s) for carbon atoms. A delayed formation of C(s) due to higher H_2 levels is found in Fig.3.11, which has also been observed in the previous section regarding the pyrolysis of methane at different levels of H_2, as shown in Fig.3.1 and Fig.3.2. The pyrolysis study in the previous section suggests that the H/C ratio primarily controls the threshold temperature at which C(s) starts to form. By comparing the results

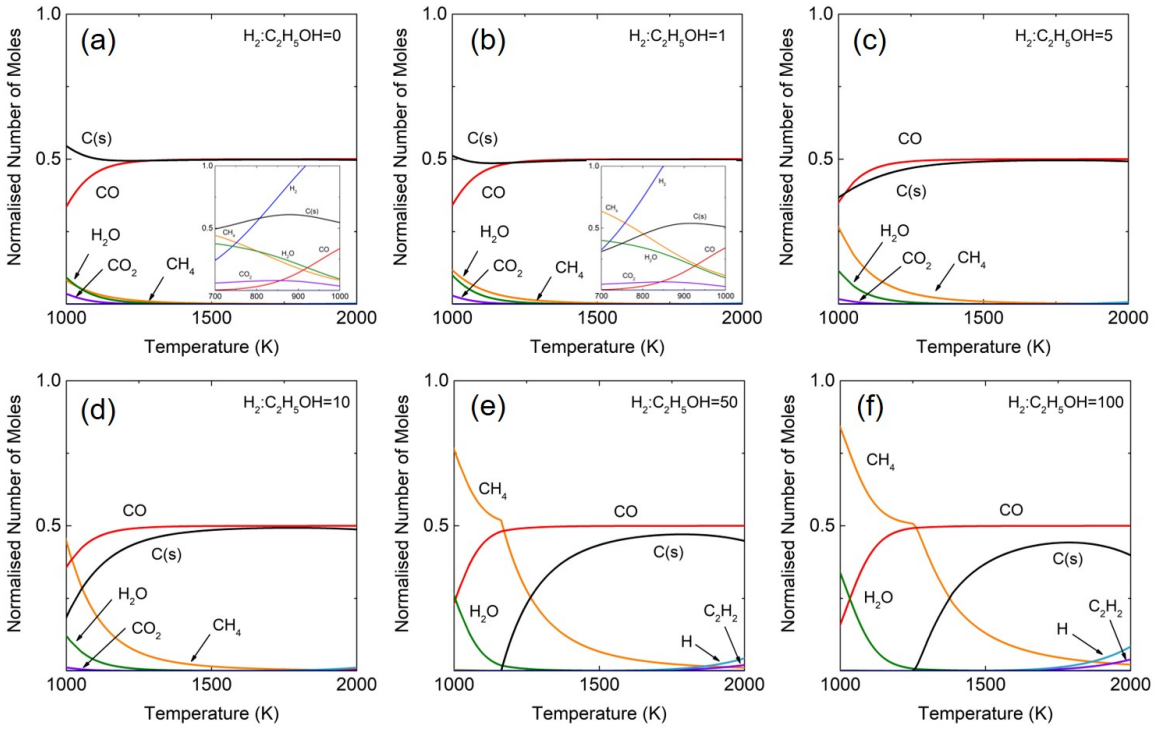

Fig. 3.11 Ethanol pyrolysis at different molar ratios of H_2/CH_4 from 0 to 100 between 1000 K and 2000 K. The number of moles for each species are normalised against the total number of moles of the system.

of the two carbon precursors (CH_4 and ethanol), it shows CH_4 is more thermodynamically stable at low temperatures ($T < 1000$ K) while ethanol seems not a stable species at any of the considered temperatures. Also it shows that the threshold formation temperature of C(s) seems unaffected by the presence of oxygen in the system while still being determined by the H/C ratio.

In contrast, the change in CH_4 as a function of temperature at different H_2 levels in the current ethanol pyrolysis study appears to deviate from previous findings due to the presence of oxygen. CH_4 is thermodynamically favoured at lower temperatures over most hydrocarbon species. The previous study shows the threshold decomposition temperature of CH_4 coincides with the threshold formation point of C(s), which are all determined by H/C ratios. Once oxygen becomes available, such a coincidence disappears when $\frac{H_2}{C_2H_5OH} > 1$, as CH_4 starts to decompose at a lower temperatures than that without oxygen given the same H/C ratio. Fig.3.11(e) and (d) explicitly present such changes. The discontinuity in the CH_4 curves coincides with the formation of C(s). The cause of the changed behaviour for CH_4 and C(s) appears is due to the formation of CO as oxygen is introduced.

For all the cases considered here, the levels of CO as a function of temperature is hardly affected by the change of H_2 levels, despite small differences induced by higher H_2 levels ($\frac{H_2}{C_2H_5OH} > 10$) below 1250 K. When temperatures elevate beyond 1250 K, CO reaches its maximum regardless of $\frac{H_2}{C_2H_5OH}$ ratios, as CO takes nearly all the oxygen atoms available at this temperature range regardless of the H_2 levels. Based on our observations, the threshold formation temperature for CO changes from 550 to 780 K as $\frac{H_2}{C_2H_5OH}$ increases from 0 to 20. Beyond this ratio, the threshold formation temperature of CO remains fixed even $\frac{H_2}{C_2H_5OH}$ increases to 100. This explains why CH_4 decomposes at lower temperatures than those cases without oxygen, as CO becomes thermodynamically more favoured as temperature increases and takes the carbon atoms from CH_4 before C(s) forms.

The oxygen-containing species are mainly CO, H_2O and CO_2 in the range of 1000 to 2000 K. As observed in the inserted plots shown in Fig.3.11.(a) and (b), H_2O consumes the majority of O atoms below 900 K, indicating O atoms are thermodynamically more favoured to combine with H to form H_2O at lower temperatures, despite the existence of a small amount of CO_2 in this range. With the increase in temperatures, CO emerges quickly from 700 K and soon surpasses H_2O, becoming the dominant O-containing species. The dissociation of H_2O at a given temperature decreases with the increase in $\frac{H_2}{C_2H_5OH}$ below 1250 K, while H_2O completely dissociates beyond 1250 K for all cases.

3.3.2 Elemental distribution at baseline condition

Fig.3.12 shows the calculated results of equilibrium elemental partitioning of C, O, Fe and S atoms as a function of temperature from 500 to 2000 K. Consistent with the oxygen-free calculations, the equilibrium elemental distribution for different atoms is plotted as an area plot format, and the total amount of each element is normalised to 1. The method of reading the area plots has been introduced in details in Section 3.2.2.

The plot on the top left of Fig.3.12 shows the elemental distribution of carbon at equilibrium as a function of temperature. It is found that CH_4 takes up all the C atoms from 500 up to 700 K. Beyond 700 K, a small fraction of C atoms starts to partition into CO and CO_2 until 820 K, where C(s) starts to form, resulting in a sharp decrease in the molar fraction of C atoms in CO_2. As the temperature increases, the molar fraction of C atoms taken up by CH_4 continues to decrease up to 1500 K, where C(s) and CO are seen to share nearly all of the C atoms in a 50:50 proportion.

The elemental distribution of oxygen is shown on the top right: H_2O remains the dominant species, consuming all O atoms up to 700 K, where CO and CO_2 start to form. When the temperature enters the typical furnace temperatures (1300–1600 K), CO replaces H_2O to become the dominant species binding with O atoms.

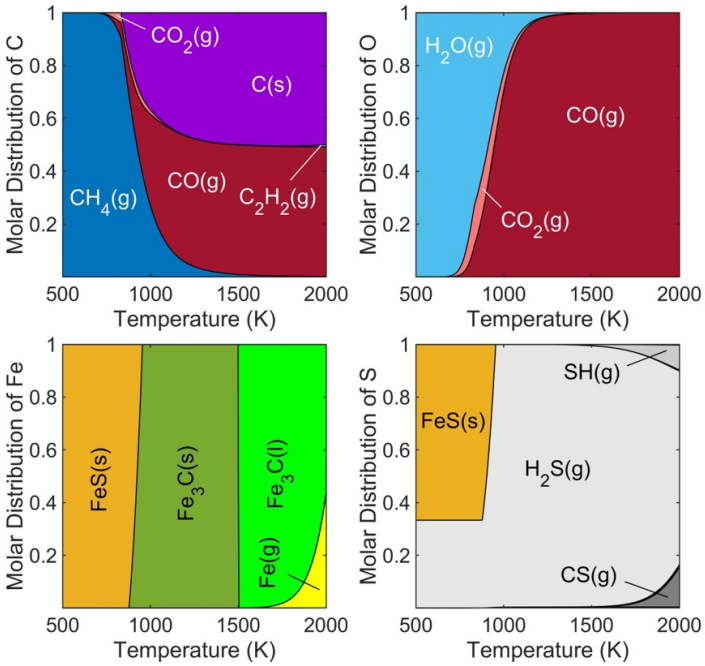

Fig. 3.12 Partition of C, O, Fe and S elements at equilibrium between 500 K and 2000 K at the baseline stoichiometry (H:C:O:S:Fe = 4500:550:270:1.5:1).

The general elemental distribution of Fe and S atoms with the variation of temperatures seems unaffected much by the presence of oxygen at these stoichiometries. Similarly to the results shown in the previous section in a C-H-Fe-S system, FeS(s) appears as the dominant species that occupies all Fe atoms at lower temperatures, in the present case below 870 K. As temperatures increase, Fe_3C(s) replaces FeS(s) as the dominant species until 1500 K where Fe_3C(s) transitions into Fe_3C(l) whilst the vapour phase iron Fe(g) starts to emerge. As for sulphur, H_2S prevails throughout the whole temperature range, and the only solid phase appears in the plot is FeS(s). Beyond 1500 K, SH(g) and CS(g) starts to form, exhibiting the same phenomenon as shown in the previous section of the C-H-Fe-S system.

Given the results shown above, it is found that the presence of oxygen in the equilibrium system primarily affects the elemental distribution of carbon due to the formation of CO, rather than Fe and S for the baseline case.

3.3.3 Effect of O/C ratios

In the present calculations, we varied the molar ratios of O to C atoms, while keeping the atomic ratios of other elements fixed at H:C:S:Fe = 4500:550:1.5:1.

Fig.3.13 summarises the distribution of species between solid and gas phases as a function of temperature from 800 to 2000 K, for different O/C ratios. The total number of moles of all

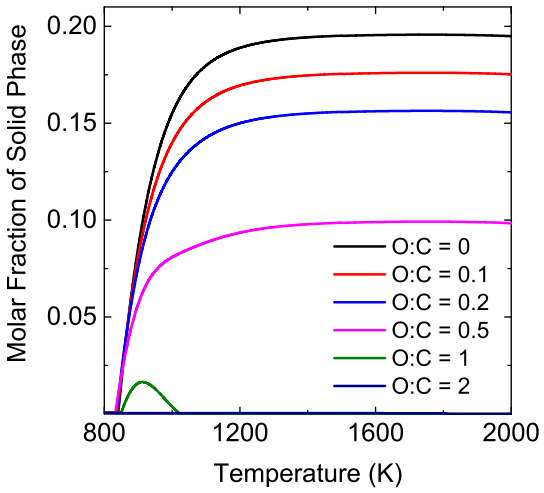

Fig. 3.13 Variation of molar fractions of solid species as a function of temperature for different O/C ratios at H:C:S:Fe = 4500:550:1.5:1. The total number of moles of all species in different phases formed at equilibrium over different temperature are normalised to unity, and the molar fraction of solid phase is calculated accordingly.

species in the system at a given temperature are normalised to unity, and the molar fraction of the solid phase is calculated accordingly. Based on our observations, C(s) is the dominant solid species, despite some minor contributions from Fe_3C(s) below 1500 K. Moreover, the threshold formation temperature for C(s) at all O/C ratios occurs at the same point (~830 K) as the H/C ratio is fixed for all the cases considered. The effects of the variation of O/C ratios are clear: as O/C increases from 0 to 2, the maximum molar fraction that the solid phase species reaches is seen to decrease from 0.19 to 0, as CO is formed rather than C(s), and eventually prevents solid carbon formation at O/C = 2.

Fig.3.14 illustrates the elemental distribution of C atoms as a function of temperature for different O/C ratios from 0.2 to 2.0. The carbon distribution plot at O/C = 0 closely resembles that shown in Fig.3.3 therefore not included in the figure. From the figure, one can clearly observe that the rise in O/C ratios largely vary the proportions of major carbon-containing species, C(s) and CO, at the high temperature range ($T > 1000$ K). The molar fraction of C atoms occupied by C(s) monotonically decreases with the increase in O/C ratios. Instead, CO competes with C(s) for C atoms and becomes the major carbon-containing species beyond O/C = 0.5. From O/C = 1.0 onwards, C(s) is no longer formed which is replaced by CO and CO_2. It can be inferred that CO is thermodynamically more favoured by C atoms rather than C(s) at high temperature zone ($T > 1000$ K). Therefore, the inclusion of oxygen in the system has a negative impact on the production of graphitic carbons from the perspective of thermodynamic equilibrium. Also observed in Fig.3.14 is an decreased decomposition

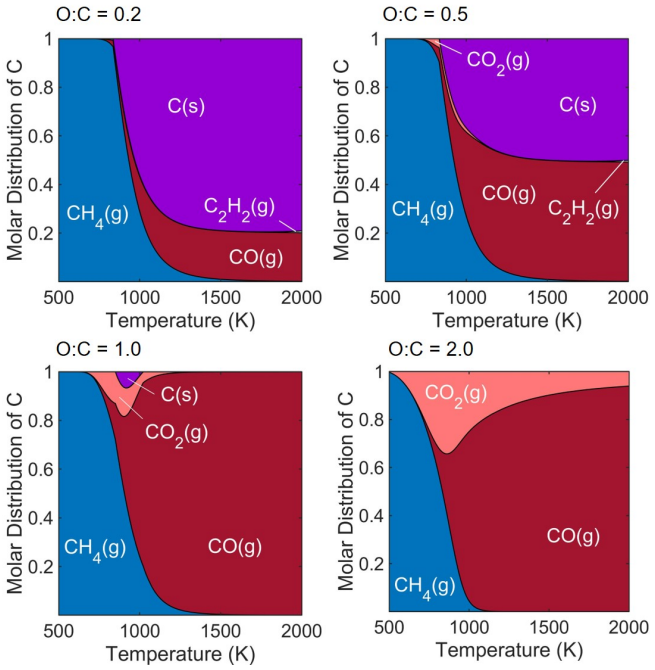

Fig. 3.14 Partition of C element as a function of temperature between 500 K and 2000 K for different O/C ratios from 0.2 to 2.0 at H:C:S:Fe = 4500:550:1.5:1.

temperature of CH_4 with the increase of O/C ratios. This is due to the fact that CO_2 starts to form at a low temperature as the O_2 level becomes higher.

More details regarding the impact of the change O/C ratios can be seen in Fig.3.15 where the elemental partitions of O and Fe atoms are depicted. The plots on the upper row illustrate the how O atoms partition into different O-containing species as temperature increases for different O/C ratios. For the cases with O/C<1, the molar distribution pattern remains hardly affected by O/C ratios, which closely resembles that with O/C = 1.0. As O/C increases beyond 1.0, the relative amount of O atoms exceeds that of C atoms which results in a alteration of the high-temperature profile of the partitioning of O atoms. According to the plots with O/C = 2.0 and 3.0, one can clearly see that H_2O, CO and CO_2 coexist over the high temperature range ($T > 1000$ K). And H_2O starts to occupy over a half amount of all O atoms when O/C exceeds 2.0. Furthermore, it can be inferred that O atoms are inclined to combine with C atoms form CO first, and then CO_2 at $T > 1000$ K. And after all C atoms are consumed, the rest of O atoms are thermodynamically driven to form H_2O. This case is of course not in general of much interest for CNT formation.

The plots on the bottom row in Fig.3.15 exhibit the elemental distribution of Fe atoms over different O/C ratios. When O/C is smaller than 1.0, the general pattern of the distribution of Fe atoms as a function of temperature appears unchanged, despite of the formation of

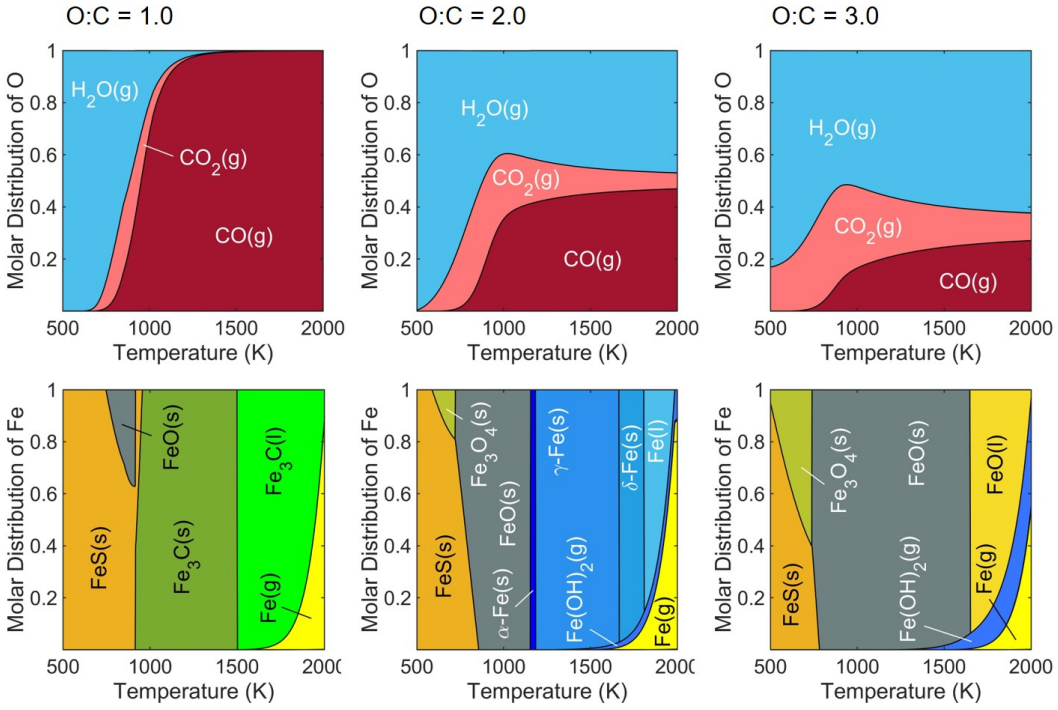

Fig. 3.15 Partition of Fe and O elements as a function of temperature between 500 K and 2000 K for different O/C ratios from 0.2 to 2.0 at H:C:S:Fe = 4500:550:1.5:1.

FeO(s) below 1000 K as indicated in the plot corresponding to O/C = 1.0. As O/C increases to 2.0, the elemtal distribution of Fe completely changes. Although FeS(s) still exists at a lower temperature below 800 K, a new solid species Fe_3O_4(s) is observed within a narrow temperature window between 590 K and 720 K. Then FeO(s) becomes a dominant species occupying all of the Fe atoms between 860 to 1150 K. From 1150 K onwards, solid elemental Fe is seen to appear and experience a complete phase transition from α-Fe(s), liquid Fe(l) and finally to vapour phase Fe(g). Therefore, one can infer from the plot that all O atoms convert into gas phase species, mostly in H_2O, CO_2 and CO, at $T > 1150$ K for C/O = 2.0. As O/C increases to 3.0, the phase transition of elemental Fe completely disappears, which is replaced by an extended formation window of FeS(s), ranging from 730 to 1650 K. Above 1650 K, one starts to observe the coexistence of liquid FeO(l), gas phase $Fe(OH)_2$ and Fe(g).

To the best of our knowledge, oxygen-containing carbon sources which were reported to be suitable for making CNTs using FCCVD all had O/C ratio no higher than 0.5. Among these species, the most frequently used was ethanol having O/C = 0.5 as shown in Table 3.2. Other sources such as diethyl ether $(C_2H_5)_2O$, polyethylene glycol $[–(CH_2\text{-}CH_2\text{-}O)_9]$, 1-propanol $CH_3CH_2CH_2OH$, acetone CH_3OCH_3, and ethylformate CH_3CH_2COOH were also reported to be viable for producing CNTs [34]. It must point out that these carbon sources all possess a O/C ratio no higher than 0.5. Although there exist some cases using

a mixed carbon sources that contained hydrocarbons and methanol for making CNTs [34], a study that uses methanol as the only carbon source to produce CNTs has yet been found. According to our present results, a rational explanation is likely due to the high O/C ratio in methanol. From Fig.3.13 and Fig.3.14, it clearly shows that the overall yield of graphitic carbons C(s) is hugely suppressed at O/C= 1.0, and therefore one shall not expect large mass production of solid carbon products by using the carbon source having such high O/C ratios.

3.3.4 Effect of S/Fe ratios

We now consider the effects of variation of S/Fe ratios on the elemental distribution of different atoms. The production of CNTs, particularly for producing CNT aerogels, is extensively affected by the relative proportions of catalytic precursors, ultimately the molar ratios of sulphur to iron, S/Fe. Following the same procedures described in Section 3.2.3.1 and 3.2.3.2, we varied the S/Fe ratios by either changing the relative amount of S or Fe while keeping the remaining elements fixed at the baseline proportion. According to Table 3.2, the S/Fe ratios of all the successful cases range from 0.1 up to 15. We hereby performed equilibrium studies for a range of S/Fe from 0.1 up to 20, which covered this region.

According to the results, the elemental partitions of C, O and S atoms are hardly changed by the variation of S/Fe ratios from 0.1 to 20, which closely resemble the corresponding plots at the baseline condition shown in Fig.3.12. The only noticeable variation observed is the formation of FeS(s) in the sulphur plots whose variations with different S/Fe ratios follow the trends as illustrated in Fig.3.4 and Fig.3.5, and are therefore not shown again.

While variations in the distributions of Fe element can be discerned. Fig.3.16 presents the variation of the elemental partition of Fe between 500 K and 2000 K for S/Fe ratios from 0.1 to 20. The plots on the top row were calculated by varying the relative amount of S atoms while keeping the remaining elements fixed at the baseline proportion of H:C:O:Fe = 4500:550:270:1; those at the bottom row were obtained by varying the amount of Fe while keeping the other elements fixed at H:C:O:S = 4500:550:270:1.5. Generally, the Fe distribution profile appears alike given at the same S/Fe ratio. Below S/Fe = 1.0, Fe_3O_4(s) and FeO(s) seem to form in a sequence as temperatures increase up to 900 K. When S/Fe exceeds 1.0, the iron oxides are placed by FeS(s) and completely disappear from the plots.

The Fe partition profile at high temperatures ($T > 1000$ K) for all the cases considered are hardly affected by the presence of oxygen. A transition from Fe_3C(s) to liquid Fe_3C(l), and the appearance of vapour phase iron Fe(g) can be clearly seen with the increase of temperature. The formation profile of Fe(g) is seen to vary with S/Fe ratios in the plots at the bottom row where Fe becomes fully vaporised at a decreased temperature with the increase of S/Fe ratios. This is due to the correlation between the temperature-dependent saturated

vapour pressure of Fe and its actual amount present in the system. As S/Fe increases, the proportion of Fe reduces, which makes Fe more easily vaporised at a lower temperature.

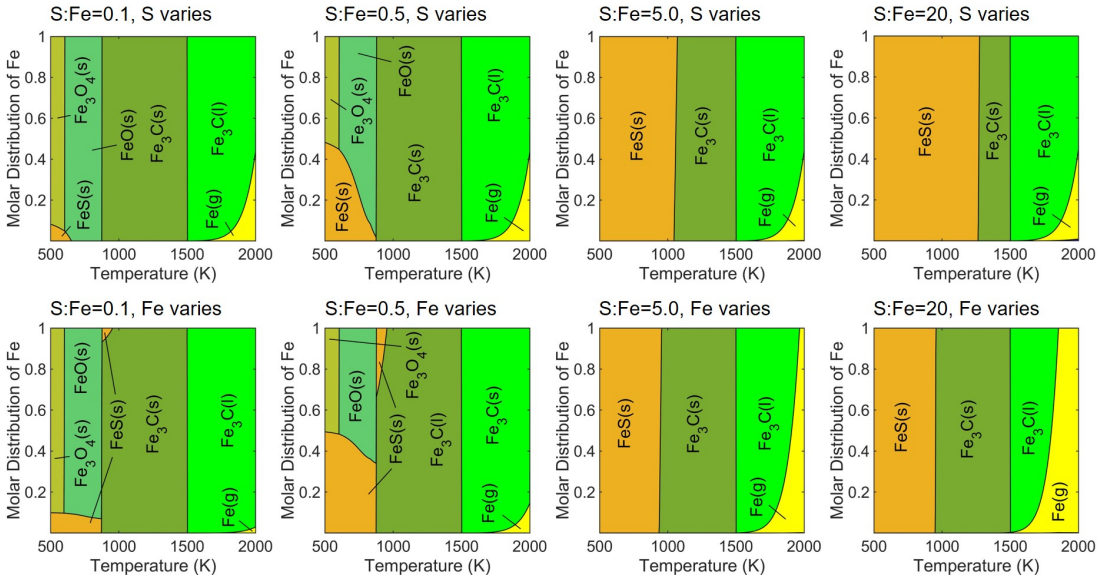

Fig. 3.16 Partition of Fe element as a function of temperature between 500 K and 2000 K for different S/Fe ratios from 0.1 to 20. Top row: the relative amount of S varies from 0.1 to 20 corresponding to the S/Fe ratio from 0.1 to 20, respectively, at H:C:O:Fe = 4500:550:270:1. Bottom row: the relative amount of Fe varies from 15 to 0.075 corresponding to the S/Fe ratio from 0.1 to 20, respectively, at H:C:O:S = 4500:550:270:1.5.

3.3.5 C-H-O ternary diagrams

The previous results focus on the elemental distribution of different atoms fixed element proportion over a range of temperatures. While the changes brought by the variation of the elemental proportions at a fixed temperature is also of great interest. For a system containing oxygen at equilibrium, the liming factor for making solid graphitic carbon has been found to be the O/C ratio rather than Fe or S elements.

Fig.3.17 depicts the equilibrium distribution of graphitic carbon C(s) with varying proportions of H, C and O elements for different temperatures from 1073–1573 K (800–1300 °C). The shaded area indicates the region where C(s) cannot be produced. As observed from the diagram, the shaded area slightly increases with the elevation of temperatures from 1073 to 1273 K beyond which the area change starts to cease. It shows that C(s) can be produced on the upper-left part of the ternary diagram, which takes half of the triangle area. Within this zone, O/C ratios are nowhere higher than 1.0, which is consistent with our findings described in Section 3.3.3. Thereby, this diagram provides a guideline for the synthesis of graphitic

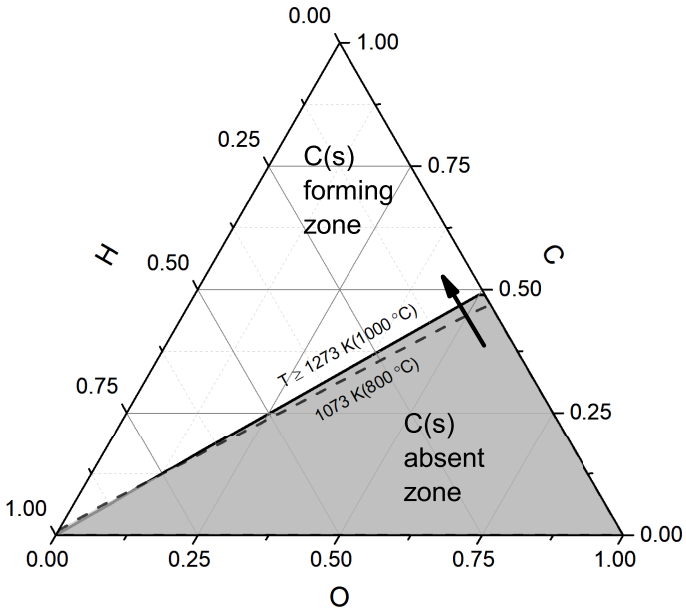

Fig. 3.17 Ternary diagram for the distribution of solid graphitic carbon C(s) over different temperatures in a C-H-O system at atmospheric pressure. The shaded area indicates the region where no C(s) can be formed.

carbon materials where a oxygen-containing carbon source with a O/C ratio lower than 1.0 is recommended.

It is worth of mentioning that other researchers have investigated the equilibrium distribution of graphite in a C-H-O system while using different numerical software [80, 79]. Our results regarding the C(s) formation show exact agreement with theirs. Apart from using graphite as the representation for all carbon solid products for the calculations, CNTs shown in Table 3.1 with available data of thermodynamic properties have also been used for the producing the C-H-O ternary diagram. It is found that the calculated boundary lines that separate the C(s) forming and absent zones by using different graphitic carbon allotropes (graphite or CNTs) overlay exactly, and therefore we choose Fig.3.17 as a representation for all graphitic carbon products.

3.3.6 Summary

Thermodynamic equilibrium calculations have been performed for a C-H-Fe-S-O system. A baseline condition was chosen based on the work by Motta *et.al* [49] who used ethanol as the carbon source that introduced oxygen into the synthesis. The pyrolysis of ethanol in various levels of H_2 has been studied, and the results show that CO and C(s) are the two major

species at temperatures above 1000 K. And the increase in H_2 results in an increase of the threshold formation temperature and a reduced yield for C(s) at a given temperature. With the presence of oxygen, carbon atoms are thermodynamically driven to form CO first at elevated temperatures, particularly at $T > 1000$ K, rather than C(s). Therefore, the elevated O/C ratios in the system result in a reduced yield of C(s) which eventually vanishes at O/C$>$ 1.0. The elemental distributions of Fe and S atoms are hardly affected by the presence of oxygen at O/C$<$ 1.0, despite the formation of some iron oxides (FeO(s) and Fe_3O_4) at $T < 1000$ K. However these solid oxides disappear at increasing S/Fe ratios beyond 1.0. More importantly, the elemental distribution profiles at high temperatures ($T > 1000$ K) for both Fe and S are not affected by the existence of oxygen given a O/C ratio below 1.0. Instead, they exhibit similar pattern as those shown in a C-H-Fe-S system: a transition from Fe_3C(s) to liquid Fe_3C(l) and an emergence of iron vapour Fe(g) with the increase of temperatures in iron partitioning; H_2S(g) takes the dominant majority of S atoms at $T > 1000$ K in sulphur partitioning. An isothermal equilibrium study of the formation of graphitic carbon products with varying amounts of C, H and O elements has been performed. The results provide a guideline for the choice of carbon sources that an oxygen-containing carbon source with a O/C ratio lower than 1.0 is recommended for making graphitic carbon materials.

3.4 Conclusion

In this chapter, we have investigated the synthesis process via a FCCVD method by virtue of thermodynamic equilibrium calculations. Two equilibrium systems, the C-H-Fe-S and the C-H-Fe-S-O sets, have been studied in detail. Thermodynamic properties of different CNTs produced via various methods are compared against that of graphite, and only slight deviations are found in the threshold conversion temperature at which CNTs or graphite starts to form. The elemental distributions of Fe and S atoms were not affected. For the system comprising C, H, Fe and S elements only, iron carbide (Fe_3C) is found to be the primary iron-containing species that exists in solid and liquid phases within the furnace temperature range (1400–1800 K), while iron vapour Fe(g) is seen to emerge at higher temperature region ($T > 1500$ K). Sulphur tends to partition into H_2S(g) over the whole temperature range, and gaseous SH(g) and CS(g) are seen beyond 1450 K. Solid phase FeS(s) exist from 300 K up to 1100 K, and its upper temperature limit of existence is determined by the S/H ratio. Ternary diagrams of C, S and Fe elements at the furnace temperature region reveal that Fe_3C, γ-Fe, FeS and C(s) are the four condensed-phases species that may be expected during the synthesis.

When oxygen is added into the equilibrium system, the overall yield of C(s) is expected to reduce as CO is a more thermodynamically favoured carbon-containing species at the furnace temperature region than C(s). The production of C(s) is primarily determined by O/C ratios where no C(s) is be formed at equilibrium if O/C exceeds 1.0. Moreover, the elemental distributions of Fe and S are hardly affected by the presence of oxygen, specifically at the furnace temperature region, if O/C is smaller than 1.0. This result is of particular interest as it provide the guideline for the choice of the carbon source for the material synthesis. It must be pointed out that the equilibrium calculations cannot alone explain the complex mechanisms in CNT synthesis, and there is a need for kinetic studies to provide a more detailed and quantitative understanding. However, the present equilibrium studies provide the limit and guidelines for the synthesis of graphitic materials from the perspective of thermodynamics, which are useful for extending our knowledge of the whole process.

Chapter 4

Flame Synthesis of CNTs: Experimental Design and Characterisation

4.1 Introduction

The previous chapters have illustrated numerical studies of CNT synthesis in FCCVD systems, with a focus on species distributions at thermodynamic equilibrium. Although these results improve our understanding of the production process, the fundamental knowledge of the inception and growth of CNTs is still quite limited. To further extend our understanding of CNT synthesis, we herein design a premixed combustion apparatus in parallel to a FCCVD system. A series of experiments were carried out, and CNTs were successfully produced using premixed H_2/air flames at atmospheric pressure. This chapter describes the design of the combustion system, the experimental procedures for the synthesis and the materials characterisation techniques.

4.2 Experimental setup

4.2.1 Flame system design

The general assembly of the flame system is shown in Fig.4.1. This apparatus consists of four major components: 1) a premixed flame burner, 2) a diluter (exhaust unit), 3) a flow supply system, and 4) a sampling unit.

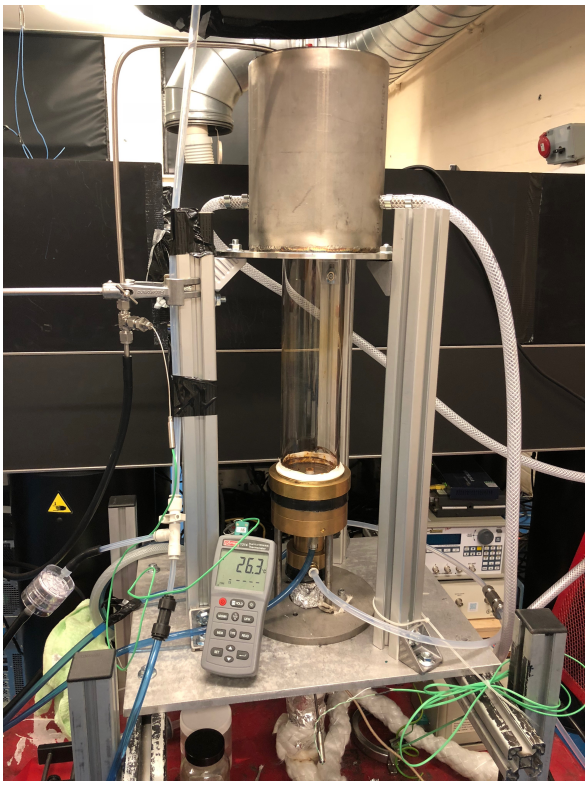

Fig. 4.1 Image of the general assembly of the flame synthesis apparatus.

4.2.1.1 Flat flame burner

A flat flame burner used for the CNT synthesis is depicted in Fig.4.2. The premixed H_2/air flames, providing heat sources for the synthesis, was stabilised on a porous sintered copper plate of 50 mm outer diameter with a porosity of ~75%. Besides, a concentric ring of copper foam of 70 mm outer diameter and 53.5 mm inner diameter was designed for co-flows, which was however not in use for the present study. An alumina tube (Almath Crucibles Ltd., recrystallised alumina 99.7% purity) of 10 mm outer diameter and 6 mm inner diameter was installed at the centre of the burner for the injection of carbon sources and catalyst precursors. The alumina tube was installed 5 mm above the burner surface, purposely designed to be apart way from the premixed flame fronts to avoid the burnout of the centrally injected reactants. A water cooling jacket to remove heat from the burner was designed in the middle of the burner body. H_2/air mixture gases were supplied from the bottom passing through the effusion holes inside the burner body and the porous burner plug before burning out in the premixed flames. To prevent hot reactant gases from leaking into working environment, a clear fused quartz tube of 75 mm outer diameter and 70 mm inner diameter (Robson Scientific, SiO_2 99.995%)

was installed on top of the burner plug and properly sealed by using a PTFE sealing strip (RS Pro White PTFE Tape, maximum operating temperature 260 °C).

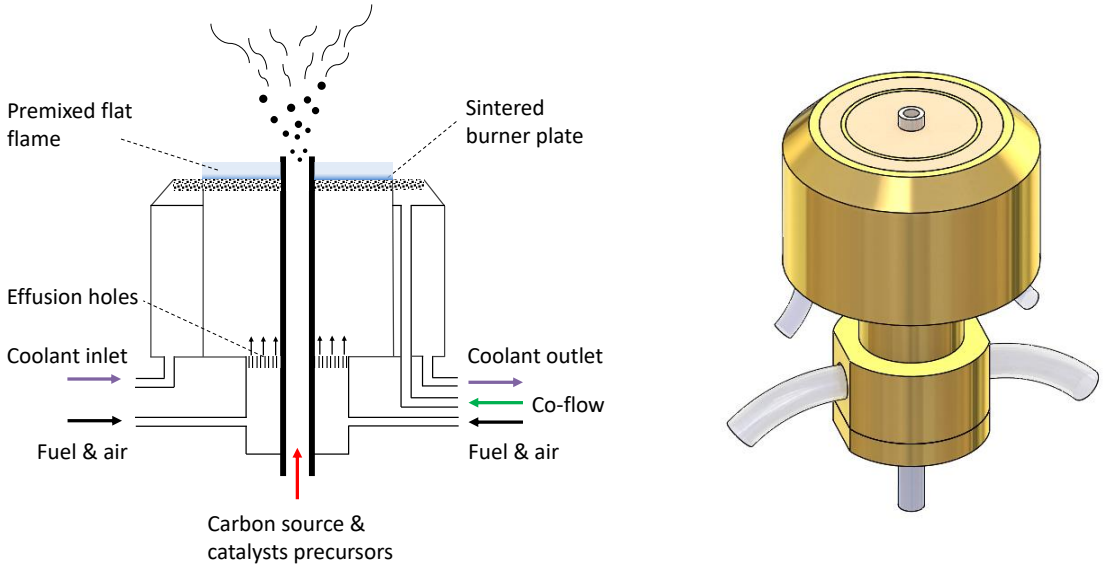

(a) (b)

Fig. 4.2 Schematic of the flat flame burner: (a) section view and (b) 3-D view.

4.2.1.2 Diluter

A diluter installed above the burner, downstream of the post-flame region was used for to: 1) heavily dilute the reactant flows (particularly unburnt H_2 gases) to form a homogeneous exhaust mixture where the concentration of H_2 shall be everywhere below its lower flammability limit (4 vol.% in air), and 2) to maintain a positive pressure difference to avoid the entrainment of air into the flame system, and 3) to cool the quartz tube by generating cold jets via orifices. Fig.4.3 illustrates the design of the diluter. Inside the diluter, 104 small orifices of 3 mm in diameter are evenly distributed on the surface of the exhaust duct. Cold N_2 gases are supplied via the two ports on the outer surface of the diluter. These inert gases enter the diluter chamber and are forced passing through the small orifices before mixing with the hot reactant gases. A 2.5 mm gap between the diluter and the quartz tube is purposely designed to leave enough room for the thermal expansion of the quartz tube. In addition, 32 orifices are placed at the bottom through which cold N_2 gases are flushed against the quartz tube to cool the tube and also prevent the entrainment of air into the diluter.

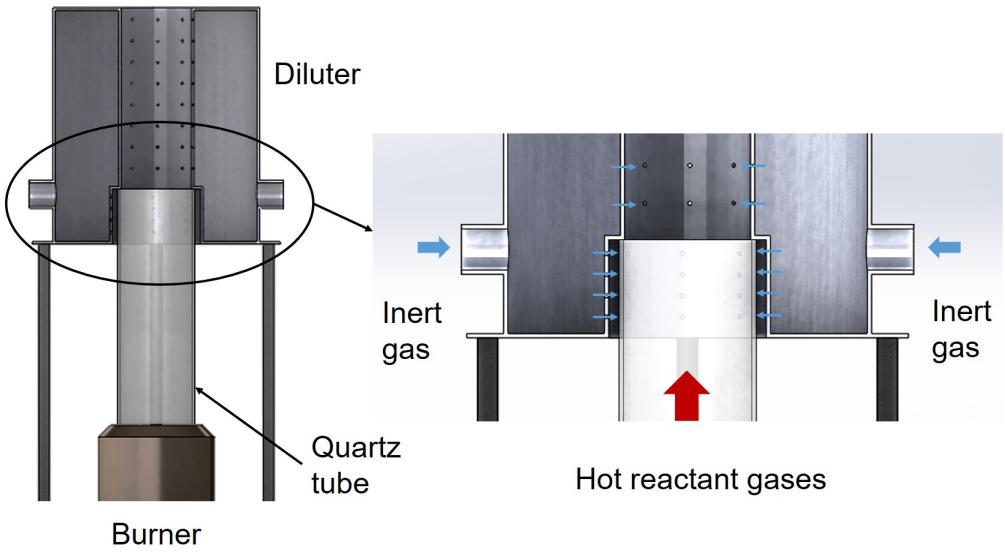

Fig. 4.3 Schematic of the diluter for exhaust disposal.

4.2.2 Flow supply system

A precise supply of both gases and reactants is critical to a successful CNT synthesis. Fig.4.4 describes the details of how gas flows and reactants are fed into the premixed flame burner. In the present study, H_2/air mixtures were used to produce premixed flat flames, while a tiny amount of CH_4 (~0.4 vol.% in mixtures) was used for helping researchers visualise the premixed flames, as a safety precaution. The fuel and air gases were initially mixed in a pipeline over a short distance before entering the mixing chamber at the bottom of the burner. Argon was the agent to carry the vaporised carbon source and catalysts into flames, whilst N_2 was for diluting the post-flame products before discharging to the exhaust. To achieve a precise regulation of all gas flows and catalysts, mass flow controllers (Alicat Scientific) were used in the system.

One of the key components of the setup is the liquid injection unit as shown in Fig.4.4. In the current study, ethanol was used as the carbon source and the solvent for dissolving various mass fractions of ferrocene (the iron catalyst precursor) and thiophene (the sulphur catalyst precursor). The feedstock was injected by a syringe pump (World Precision Instruments) at a range of injection rates $\dot{q}$ into a house-made atomiser. The atomised solution then sequentially entered the heated pipeline and the central tube of the burner. An stream of argon flow was directed into the atomiser to carry the atomised feedstock through the pipeline. To effectively vaporise the liquid droplets, the atomiser and the pipeline was heated and maintained at 100 °C at which ethanol (boiling temperature at 78.37 °C), thiophene (boiling temperature at 84

°C) and ferrocene (sublimation temperature $\geq$ 100 °C) can fully transform into gas phase. The temperature of the vaporised feedstock and the carrier gas were *in situ* monitored by a thermocouple inserted inside the pipeline, just below the bottom of the burner, to ensure the injected feedstock was fully vaporised.

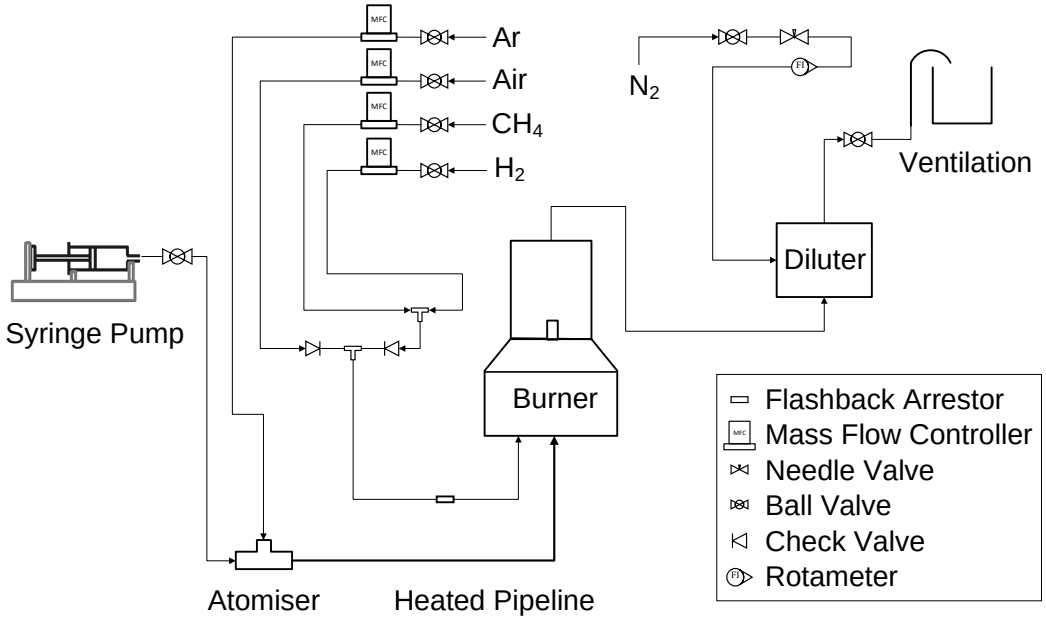

Fig. 4.4 Schematic of the flow supply system for the CNT synthesis.

4.2.3 Sampling unit

In order to determine and characterise the solid species formed in the post-flame region, a sampling unit was designed to collect the as-produced materials as shown in Fig.4.5. A stainless steel tube (6 mm outer diameter and 3 mm inner diameter), used as the sampling probe, was inserted all the way through the reacting region a few centimetres below the bottom of the diluter to avoid the disturbance by the diluting gases. The height of the probe head relative to the burner surface, or height above burner (HAB), is adjustable, while it was fixed at 230 mm HAB for the present study. A thermocouple was installed at the upstream of the sampling unit for *in situ* monitoring the flow temperatures to prevent overheating of the sampling unit.

Directly connected to the filter holder was electrically conductive rubber tubes which possess flexibility and ease of assembly characteristics. A cold finger device was designed to remove water vapour formed during the synthesis. As shown in Fig.4.5, this device consists

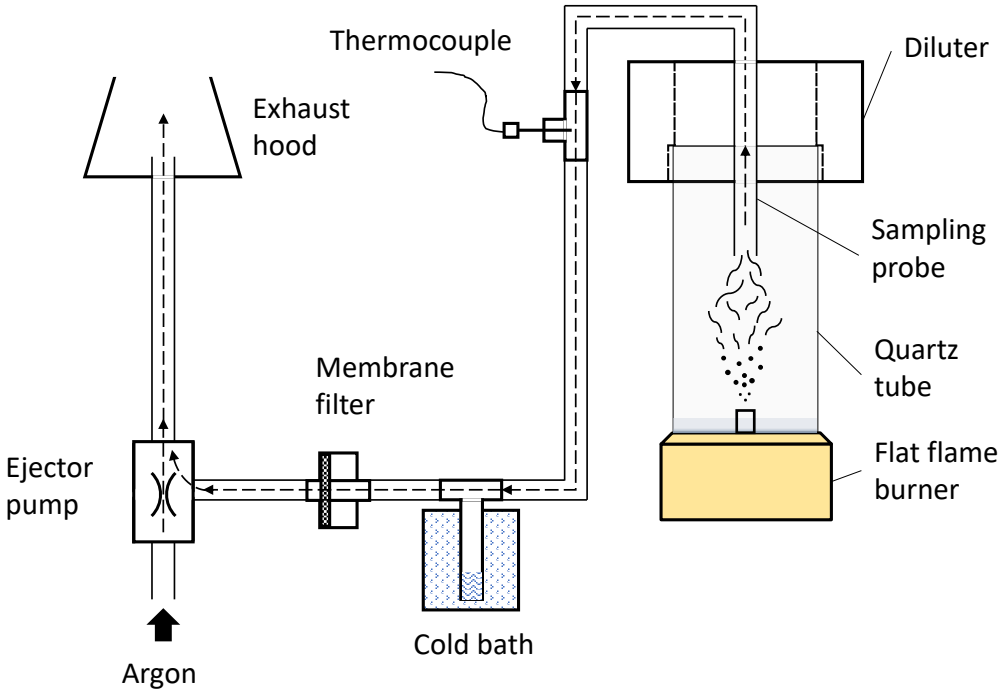

Fig. 4.5 Schematic of the sampling unit.

of a tee pipe fitting with one port connected with a long stainless steel tube inserted into a cold bath filled with ice. This creates a localised cold site, which helps effectively condense and reduce water vapour from the sampling flow. The solid products formed during the synthesis were collected on the PTFE membrane filters (SKC Ltd, pore size 0.45 μm) installed inside the filter holder. The PTFE filters possess many advantages particularly for the current application as they are chemically inert to acids, bases and solvents, and are hydrophobic which make them ideal for aerosol sampling in damp environments.

The current process used rich premixed H_2/air flames for CNT production, the flows in the post-flame region therefore contained a certain fraction of unburnt H_2 gas. As a result, normal vacuum pumps become unsuitable for the current application, as unburnt H_2 gas may arouse explosion concerns when encountering oxygen, even in a small quantity. Instead, we chose to use an ejector pump, an cost-effective method, to generate vacuum in the sampling unit that drove the post-flame flows through the pipeline.

The ejector pump (SMC ZH05L-X267) has a 0.5 mm orifice and a capacity of creating vacuum pressure up to -48 kPa given a supply air pressure of 4.5 bar. The operating principle of an ejector is based on Bernoulli's Principle which states that the pressure of a flow decreases with the increasing of its velocity and vice versa. Accordingly, a pressure difference in an ejector is achieved by a built-in nozzle with a small orifice, which accelerates

the primary flow passing through the diffuser, and, hence, creates a vacuum pressure that drives the secondary flow into the devise. Based on the principal the flow rate of the sampling stream is in proportional to the vacuum pressure created inside the ejector, therefore a mass flow controller was used to regulate the driving flow to adjust the vacuum pressure. The exhaust was discharged to the extraction. Due to the existence of flammable gases in the sampling flow, we used argon instead of air as the driving flow to extract the sampling stream. A calibration was carried out for the unit. Fig.4.6 illustrates the change of the driven gas flow rate as a function of that of the driving gas flow (argon) where the dot symbol represents the measured data. To avoid disturbing the reactant flows, we chose 10 slpm as the driving gas flow rate which led to a driven gas flow rate at 1.7 slpm. It is worth noting that the accumulation of solid particles/CNTs on the membrane filter leads to an increased pressure drop across the filter, thus gradually reducing the sampling flow rate over time.

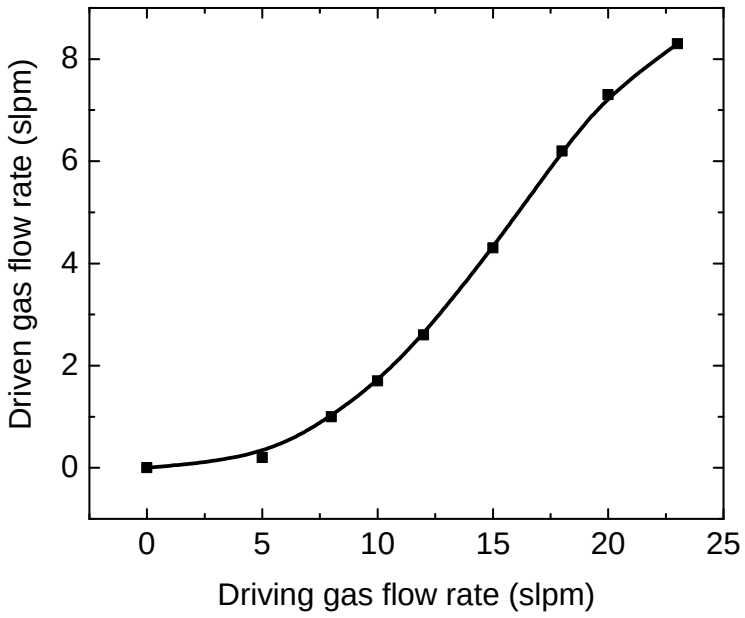

Fig. 4.6 Variation of driven gas flow rates (sample streams) as a function of driving gas flow rates (argon) at 25 °C.

4.3 Experimental procedures

4.3.1 Feedstock preparation

Prior to the flame synthesis, feedstocks containing different proportions of ethanol (VWR, Ethanol absolute $\geq$ 99.8 %), ferrocene (Sigma-Aldrich, assay $\geq$ 98%) and thiophene (Sigma-Aldrich, assay $\geq$ 99%) were prepared. Ethanol was used as the carbon source and the solvent for dissolving catalyst precursors, ferrocene and thiophene. Since the proportion of each constituent was on a mass basis, we chose 30 g as the benchmark for each feedstock. These ingredients were sequentially added to a 50 ml vial and carefully weighed out on a digital balance to the exact amount. Then the vial was properly sealed and put into a hot bath at 30°C and sonicated for 10 min to help dissolve the catalyst precursors. The well-dispersed feedstock was then added into a glass syringe mounted on the pump to be used for the following synthesis.

4.3.2 Flame ignition

H_2 is a highly reactive and flammable gas with a flame speed much higher than most of the hydrocarbon fuels. A direct ignition of premixed H_2/air mixtures in an open atmosphere may be risky and shall be avoided as it may cause unwanted leakage of highly flammable H_2 gases to the working environment, arousing safety concerns. In order to minimise hazards, we designed a multi-step ignition procedure. A stoichiometric CH_4/air mixture was firstly ignited and stabilised on the premixed flame burner, and then H_2 was gradually added into the flame whilst reducing the CH_4 supply until the target equivalence ratio ϕ of the H_2/air mixture was achieved.

Prior to ignition, a flammable gas detector (Crowcon Gasman Portable Detector) was put adjacent to the diluter as a safety precaution. Next, CH_4/air mixtures at the stoichiometric point (CH_4 typically supplied at 1.3 slpm) were fed from the bottom of the burner, and were then ignited from the top of the diluter as shown in Fig.4.3 using a butane torch. Once the mixture was successfully ignited, the flame quickly propagated through the diluter and the quartz tube and then stabilised on the burner plate. After that, N_2 gases were flushed into the diluter chamber at 40 slpm, a rate sufficient to dilute exhaust gases. Then the critical step comes the addition of H_2. According to stoichiometry, the oxygen consumption ratio of H_2 to CH_4 equals to 1:4 for a complete combustion. In order to maintain ϕ at 1.0, we gradually decreased the supply of CH_4 at a step of 0.2 slpm whilst increasing H_2 at 0.8 slpm until the flow rate of CH_4 was regulated at 0.1 slpm. The flow rates of H_2 and air were then tuned to the target condition. Since pure H_2 flames feature a faint blue colour which is hardly

to be observed, we therefore intentionally left 0.1 slpm CH_4 (~0.4 vol.% in mixture) in the mixture to make the flame visible. Such safety measure allows the experimenter to quickly observe any unexpected extinction or quenching of flames and take measures immediately to minimise the risk of hazards. The contribution of CH_4 was taken into account in the calculation of equivalence ratios of the flammable mixtures.

4.3.3 Synthesis procedures

After premixed H_2/air flames were established on the burner, the syringe pump was set to the target feeding rate and started to pump the feedstock into the pipeline. Meanwhile, argon, typically at $\dot{V}_{Ar} = 0.1$ slpm, entered the atomiser and drove the feedstock droplets passing through the heated pipeline and the central tube for the subsequent synthesis. As shown in Fig.4.7, the vaporised ethanol and ferrocene mixtures carried by argon entered the post flame region of the premixed H_2/air flames where the primary species was post-flame products H_2O and N_2. The faint blue ring sitting on top of the burner plate was the premixed H_2/air flame doped with a tiny amount of CH_4, while the glowing reddish flow corresponded to the pyrolysis region. The as-produced materials were sampled by a stainless steel probe located on the top of pyrolysis region (fixed at 230 mm HAB), just below the diluter. Further downstream, the hot mixtures were heavily diluted by N_2 gases in the diluter chamber before being discharged to the exhaust.

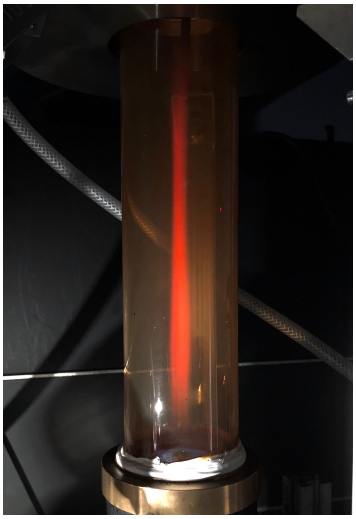

Fig. 4.7 Image of the pyrolysis region of the CNT synthesis process at $\phi = 1.05$ (H_2=7 slpm and air=16.7 slpm). The feedstock consisted of 1.0 wt.% ferrocene and 99.0 wt.% ethanol, and was injected at 0.5 ml/min and carried by argon at 0.1 slpm. The red colour was a result of the radiation from the heated oxidised iron and nanomaterials.

4.3.4 Experimental conditions

One of the main advantages of using premixed flames for the CNT synthesis is the flexibility of altering equivalence ratios ϕ. This facilitates the control of the synthesis temperature widely accepted as a critical parameter that determines the inception and formation of CNTs [75]. The equivalence ratio ϕ in the present study is defined as the ratio of actual fuel to air ratio, normalised by the stoichiometric value $\frac{(m_f/m_a)}{(m_f/m_a)_s}$. Therefore, $\phi = 1$ represents stoichiometry whereas fuel-rich and fuel-lean correspond to $\phi > 1$ and $\phi < 1$, respectively. As introduced in the previous sections, high temperatures are essential for CNT synthesis, particularly for producing SWCNTs by a FCCVD method, where a temperature above 1100 °C is usually required [51, 34]. Another important parameter is residence time τ, a key factor that controls the growth of CNTs. In the furnace region ($T > 1000$ °C), τ is usually of the order of seconds [41], whereas τ in a flame system is typically of hundreds of milliseconds.

In order to avoid excessive oxidation of the carbon source and catalyst precursors, operating conditions were constrained to rich premixed regions where $\phi \geq 1.0$. Although computed adiabatic flame temperatures (see Fig.5.4) are well beyond the synthesis temperature, 1150–1450 °C [49], heat loss to the surrounding environment must be taken into account in the practical scenarios. Most of the heat transfer is from the hot gases to the burner coolant, as well as natural convection around the quartz tube. We started with $\phi = 1.0$ for the H_2/air mixtures while trying to minimise the overall mixture flow rates to get a longer τ that matches the order of seconds achieved in a FCCVD method, although longer τ may also lead to a higher overall heat loss.

Since many parameters of the system may affect the synthesis in various ways, a parametric study on the process was performed. We categorised these parameters into four groups: synthesis temperatures, residence time, carbon loading and catalyst concentrations. To create a relatively stable region for the pyrolysis at the central region to avoid shear instabilities of the injected stream with the surrounding gases, we attempted to match the existing velocity of the central stream with the surroundings. The carrier gas flow and the liquid injection rate were adjusted to at 0.1 slpm and 0.5 ml/min, respectively, which led to a velocity of 27 cm/s at 100 °C for the centrally injected flow, comparable to 55 cm/s of the surrounding flow velocity given a post-flame temperature at 1400 °C. These conditions were used as the baseline for the following parametric studies.

As for the recipe of the carbon source and catalyst precursors, we used one of the most popular practises in a FCCVD process–ethanol as the carbon source, and ferrocene and thiophene (in Chapter 6) as the catalyst precursors [34, 125, 42, 49, 94] (see Table 3.2).

4.4 Numerical analysis

The 1-D burner stabilised flame was simulated using Cantera software. Here we briefly introduce the governing equations for the computational analysis, and a detailed mathematical descriptions can be found in Ref.[76]. In the Cantera software tools, flames are considered as an axisymmetric stagnation flow, which can be described by the following equations:

Continuity:

$$\frac{\partial \rho u}{\partial z} + 2\rho V = 0 \tag{4.1}$$

where ρ and u are the mixture density and the axial velocity, respectively; v is the radial velocity and $V = v/r$ is the scaled radial velocity.

Radial momentum conservation:

$$\rho u \frac{\partial V}{\partial z} + \rho V^2 = -\Lambda + \frac{\partial}{\partial z}\left(\mu \frac{\partial V}{\partial z}\right) \tag{4.2}$$

where Λ is the pressure eigenvalue ($\frac{d\Lambda}{dz} = 0$), and μ is the dynamic viscosity.

Energy conservation:

$$\rho c_p u \frac{\partial T}{\partial z} = \frac{\partial}{\partial z}\left(\lambda \frac{\partial T}{\partial z}\right) - \sum_k j_k c_{p,k} \frac{\partial T}{\partial z} - \sum_k h_k W_k \dot{\omega}_k \tag{4.3}$$

where λ and c_p are the heat conductivity and the specific heat capacity at constant pressure, respectively; $c_{p,k}$, j_k, h_k, W_k and $\dot{\omega}_k$ are specific heat capacity, the diffusive mass flux, enthalpy, molecular weight and the molar rate of production of species k, respectively.

Species conservation:

$$\rho u \frac{\partial Y_k}{\partial z} = \frac{\partial j_k}{\partial z} + W_k \dot{\omega}_k \tag{4.4}$$

where Y_k is the mass fraction of species k.

4.5 Raman spectroscopy

Raman spectroscopy has been widely used as a fast and effective tool for identifying CNTs, as their spectra exhibit distinct features which differentiate themselves from other species and various carbon allotropes. The radial breathing mode (RBM) at low Raman shift frequencies together with the G-band at higher frequencies is identified as the two dominant Raman features, whereas other features such as the disorder/defect induced D-band may also be observed in spectra of CNTs [127]. Above all, the RBM, a result of the coherent radial

vibration of C atoms, are identified as the unique signature to CNTs, occurring at frequencies in the range of 120–350 cm^{-1} and for SWCNTs of diameter of 0.7–2 nm [127].

The Raman spectroscopy analysis in the present study was carried out at ambient pressure and room temperature using a 532 nm wavelength laser of a Raman spectroscopy system (HORIBA; model: XploRA PLUS). Samples were placed on a glass slide under a 50x objective and the Raman spectra were recorded in the range of 50–3000 cm^{-1} for an acquisition time of 20 s with 2 scans. If not explicitly stated otherwise, the analysis for each sample was performed at 3 random locations, and the obtained Raman spectra at these locations were then normalised against their respective global peak value. An averaged Raman spectrum for each sample was obtained accordingly and re-constructed by doing a baseline correction.

Besides, other techniques including scanning electron microscopy (SEM), transmission electron microscopy(TEM) and energy dispersive X-ray (EDX) were also applied for characterising the nanomaterials.

Chapter 5

Synthesis of CNTs in Premixed Hydrogen/Air Flames: A Parametric Study

5.1 Introduction

We here demonstrate a controlled way of producing CNTs using premixed H_2/air flames at various ϕ at atmospheric pressure. This method exhibits potential scalability for CNT production owing to its simple floating catalyst characteristics, and it also facilitates theoretical modelling for studying the synthesis due to its 1-D flame structure. A systematic parametric study on the process is detailed in the present chapter. We categorised these parameters into four groups: synthesis temperatures, residence time, carbon loading and catalyst concentrations.

5.2 Results and discussion

5.2.1 Background signals

As described in Chapter 4, the as-produced nanomaterials were collected on PTFE membrane filters via the sampling unit; these materials together with the supported PTFE substrate were then directly analysed by Raman spectroscopy. Here we examine the background Raman spectrum of an unused PTFE filter prior to the subsequent analysis of the materials collected from the synthesis.

Fig.5.1 shows the normalised Raman spectrum of the membrane filters used for collecting materials produced in the flame. Although the spectrum exhibits multiple sharp peaks in the range of 200 to 1400 cm^{-1}, it must be pointed out that their the actual intensities are quite small and do not interfere with the featured peaks of CNTs if they exist in the collected samples. Moreover, the featured Raman peaks of CNTs are normally located at ~1340 cm^{-1} for the D-band, ~1590 cm^{-1} for the G-band, and 120–350 cm^{-1} for the RBM. Hence if there exist CNTs in the samples, they can be easily distinguished from the PTFE background.

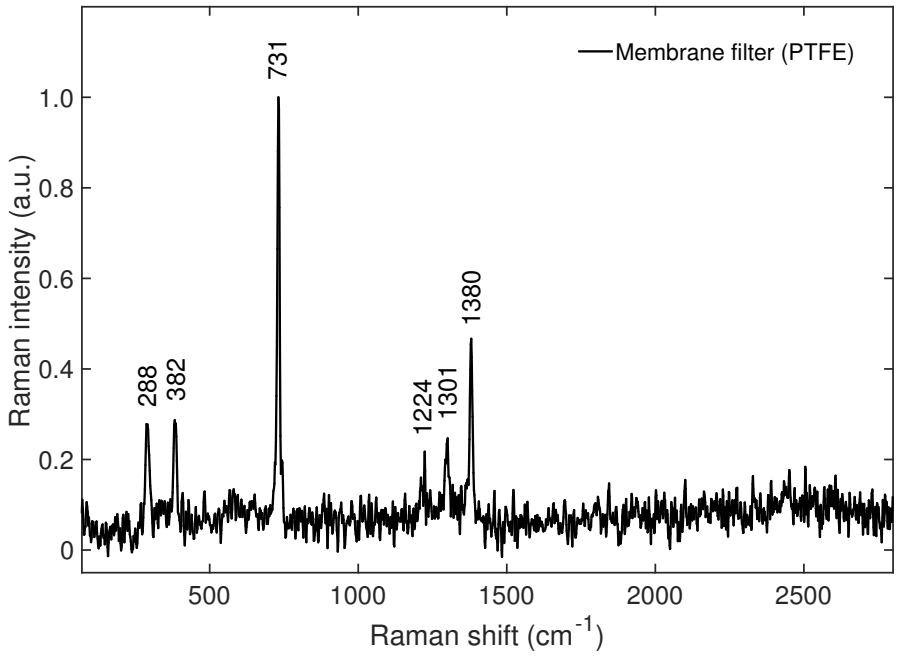

Fig. 5.1 Normalised Raman spectrum of an unused PTFE membrane filter.

5.2.2 Effect of equivalence ratios

In the current study ϕ was adjusted by varying the flow rate of air while keeping the fuel supply fixed (7 slpm H_2 and 0.1 slpm CH_4), and the experimental conditions for the study are listed in Table 5.1. Besides, the carrier gas flow and the liquid injection rates were set to 0.1 slpm and 0.5 ml/min, respectively. The solution used for the synthesis consisted of 99 wt.% ethanol and 1 wt.% ferrocene. Products synthesised in the post flame region at different ϕ were collected on a PTFE membrane filter for 3 min via the sampling unit whose probe was placed at HAB $= 230$ mm.

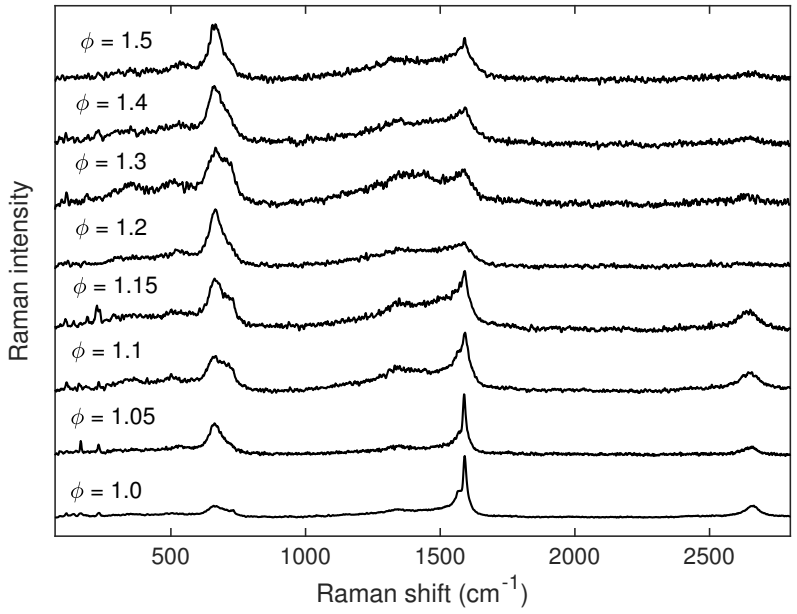

(a)

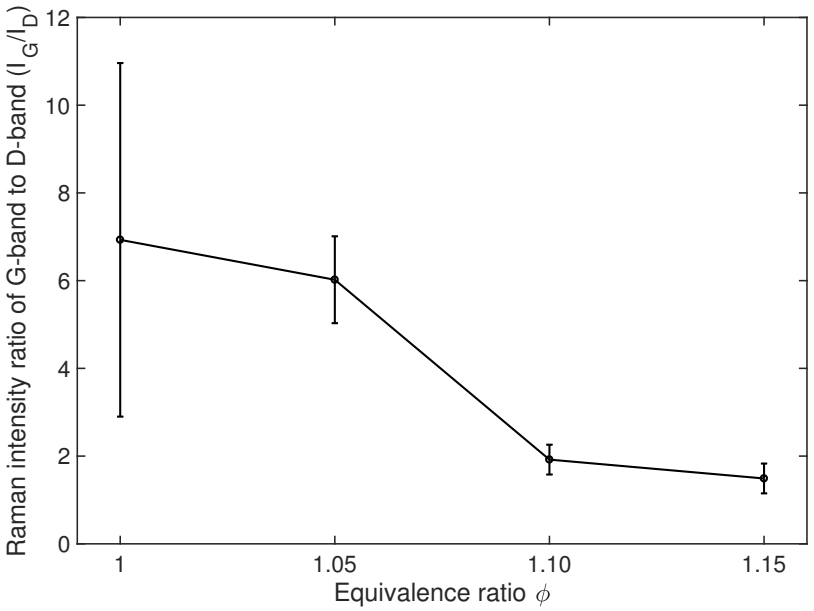

(b)

Fig. 5.2 (a) Normalised Raman spectra of the samples produced at different equivalence ratios ϕ from 1.0 to 1.5, and (b) variation of Raman intensity ratio of G-band to D-band as a function of different ϕ. The feedstock consisted of 99.0 wt.% ethanol and 1.0 wt.% ferrocene, and was injected at 0.5 ml/min and carried by argon at 0.1 slpm.

Table 5.1 Experimental conditions for the study of the effect of equivalence ratios ϕ

Test No.	Equivalence ratio ϕ	H_2 (slpm)	Air (slpm)
A1	1.0	7	17.5
A2	1.05	7	16.7
A3	1.1	7	16
A4	1.15	7	15.3
A5	1.2	7	14.6
A6	1.3	7	13.5
A7	1.4	7	12.6
A8	1.5	7	11.7

5.2.2.1 Raman spectroscopy analysis

Fig.5.2.(a) shows the normalised Raman spectra of samples collected at different ϕ from 1.0 up to 1.5. Generally, it is seen that the Raman spectra at ϕ between 1.0 and 1.15 exhibit distinct features of CNTs compared with other conditions. These features include the RBM at the lower frequency range of 120–350 cm^{-1}, G-band at ~1590 cm^{-1}, and high intensity ratio of the G-band to D-band, I_G/I_D. The broad band at around 670 cm^{-1} is believed due to the existence of magnetite (Fe_3O_4) in the sample whose Raman spectra have been studied in Ref.[128, 129]. While a shoulder alongside this peak at 731 cm^{-1} attributes to the background signal from the PTFE substrate. According to the figure, it shows that the Raman signals from the samples attenuate with the increase of ϕ. And this indicates a decreased yield of the solid materials, as evidenced by the appearance of the "shoulder" at 731 cm^{-1}. In contrast, as ϕ gets closer to the stoichiometric point, or higher temperatures, the spectra for $\phi = 1.0$ and 1.05 stand out for a much better signal-to-noise ratio and a higher I_G/I_D ratio, with the RBM distinctively observed at $\phi = 1.05$. Generally the G-band is found much less pronounced beyond $\phi = 1.15$, meaning that graphitic carbon allotropes such graphite or CNTs cease to form beyond this point and may be replaced by amorphous soot particles or iron oxide nanoparticles as indicated by the diminishing G-band and an enhanced band of magnetite.

A closer examination of the intensity ratio I_G/I_D over different ϕ between 1.0 and 1.15 is illustrated in Fig.5.2.(b). The figure shows the variation of the mean I_G/I_D ratio as a function of different ϕ with their respective standard deviations. The I_G/I_D ratio is widely used as an index to reflect the purity and defect density of CNTs [127]. The value at each ϕ corresponds to an averaged I_G/I_D ratio calculated from two separate experiments for the same condition over 6 different sites on each sample. According to the figure, I_G/I_D decreases with the increase of ϕ from 6.9 at $\phi = 1.0$ to 1.5 at $\phi = 1.15$, whilst the associated standard deviation

exhibits the same trend, decreasing from 3.8 at $\phi = 1.0$ to 0.33 at $\phi = 1.15$. The reason for the larger unsteady deviation at high temperatures is unclear, but could be a result of fluctuating temperatures and stoichiometries in the slowly flapping flame.

To further understand the effects of ϕ on the synthesis of CNTs, the normalised Raman spectra of the samples produced at ϕ from 1.0 to 1.15 were deconvoluted into five Lorentzian peaks in the range of 1000–2000 cm^{-1}, as shown in Fig.5.3. The deconvolution was performed using a Gaussian-Lorentzian fitting function, a typical method applied for analysing Raman spectra of CNTs [130]. The composite fitting curve, represented by the black thick line, shows an excellent agreement with the Raman spectra over different ϕ. The goodness of fit for the Raman spectrum at each ϕ was indicated by the R^2 value, the coefficient of determination, which was above 0.98 for all the fittings ($R^2 = 1$ indicates a perfect fit). From the figure the Raman spectra for all the cases are deconvoluted into five bands which can be categorised into two regions: G-band and D-band. The G-band is composed of two peaks: G^- and G^+ peaks. In comparison to that of graphite, which has only a single Lorentzian peak at 1582 cm^{-1}, the G-band of CNTs, particularly for SWCNTs, normally comprises two main components: G^- and G^+ at 1570 cm^{-1} and 1590 cm^{-1}, respectively [127]. The G^+ feature is associated with the vibrations of carbon atoms in the direction of the axis of a CNT, the G^- feature, on the other hand, is a result of the vibration of carbon atoms along the circumferential direction of a CNT [127]. From the figure, one can see a clear variation of the normalised intensity of the G^- and G^+ features over different ϕ. Specifically, the Raman spectrum at $\phi = 1.05$ possesses the highest G^+ peak (~0.8) compared with the other Raman spectra, which decreases with the increase of ϕ for rich cases ($\phi > 1.05$). In contrast, the intensity of the G^- peak increases with ϕ, leading to a decreased G^+/G^- intensity ratio.

Apart from the G-band, the deconvolution of the D-band into three different peaks is shown in Fig.5.3. The rise of the D-band of a CNT Raman spectrum is associated with defects or disorder in the materials, and its intensity is mainly a result of the D4, D, and D3 components at ~1200 cm^{-1}, ~1340 cm^{-1} and ~1500 cm^{-1}, respectively [131]. While their actual frequencies depend on carbon structures and also the laser excitation wavelength. The D3 and D4 peaks can only be observed in soot or amorphous carbonaceous materials [131], whereas the D peak is widely seen in many carbon allotropes except for diamond. The rise of the D peak, as the most prominent peak in the D-band, attributes to the vibration of disordered graphitic lattice [131, 132]. On the shoulder of the D feature, the D4 and D3 peaks are usually observed at lower and higher frequencies, respectively. The former is believed to be a result of the stretching vibrations of polyene-like structures and ionic impurities [133, 132] while the latter has links with the amorphous contents presenting in soot such as organic molecules and fragments [133, 131]. Generally, the normalised intensity

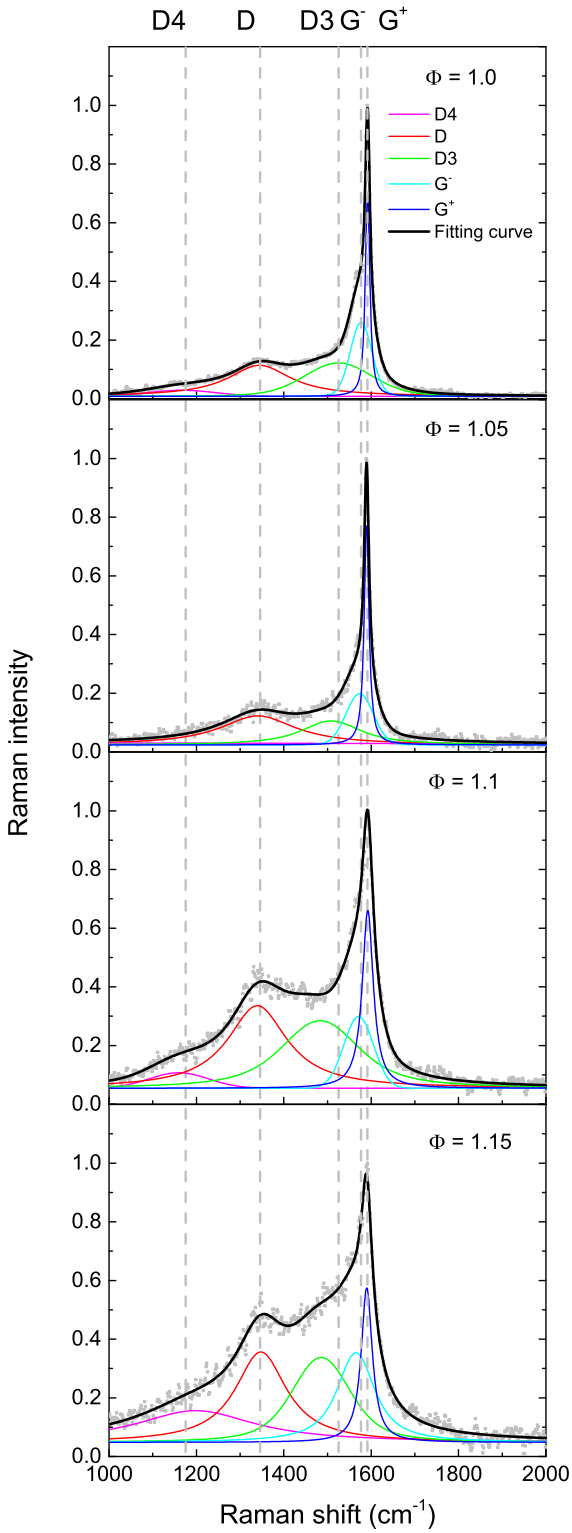

Fig. 5.3 Normalised Raman spectra (shaded dot) and their spectral deconvolution into Lorentzian peaks in the wavenumber range from 1000 to 2000 cm^{-1} for ϕ from 1.0 to 1.15.

of the D-band comprising the three featured peaks increases with the increasing ϕ, indicating a inversely proportional relationship with temperature. While the normalised intensity of the D4 peak keeps increasing as ϕ increases, in contrast to the other D peaks, which may indicate an increased proportion of olyene-like structures or ionic impurities formed in the materials.

5.2.2.2 Calculation of flame temperatures

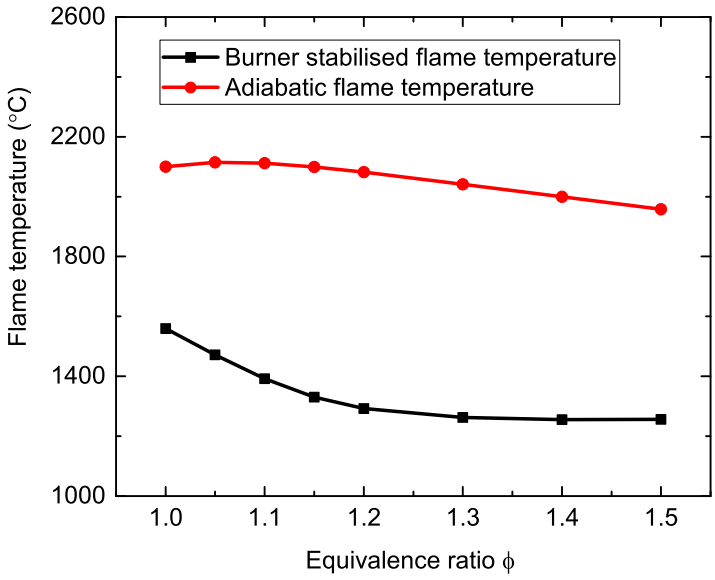

Fig. 5.4 Calculated adiabatic and burner stabilised flame temperatures as a function of equivalence ratios. The burner stabilised flame temperatures were calculated based on the conditions shown in Table 5.1 given an inlet temperature of 25 °C and at atmospheric pressure.

To further understand the variation of I_G/I_D ratios over different ϕ, the knowledge of flame temperatures is a necessity. Fig.5.4 shows the variation of the calculated adiabatic and burner stabilised flame temperatures as a function of different ϕ. In the current study, ϕ was changed by varying the air flow rate while keeping the fuel supply fixed. Hence the overall flow rate of mixtures, or the mass flux $\dot{m}$ at each ϕ was changed accordingly. As a result, the burner stabilised flame temperature decreases steadily with the increase of ϕ. This is due to the change in the mass flux $\dot{m}$ of the mixture, which controls the heat loss to the cold burner: the higher the mass flux, the lower the calculated percentage heat loss to the burner for a fixed input surface temperature of 25 °C.

Fig.5.2 has shown that that the flame temperature is a dominant parameter controlling the quality of the produced CNTs. More specifically, there exists an apparent threshold temperature of ~1200 °C above which the desired Raman features of CNTs start to emerge, which corresponds to $\phi = 1.15$. This threshold is consistent with the results suggested by the FCCVD process where SWCNTs mostly start to form beyond 1100 °C. In addition, from Fig.5.2(b), it is found that the I_G/I_D ratio decreases in proportion to the increase in ϕ, which is related to the flame temperature.

5.2.2.3 SEM analysis

Fig.5.5 shows the SEM images of samples collected at HAB = 230 mm during flame synthesis at $\phi = 1.0 - 1.1$, corresponding to the conditions of Test A1 to A3 in Table 5.1, respectively. The samples were coated with a thin film of gold/palladium (Au/Pd) alloy by sputtering–a routine treatment prior to a SEM inspection–to improve conductivity of the sample surface. This procedure prevents the materials from overcharging, thus helping achieve a better resolution of the images. Except that, no other treatments were performed on the samples. From the figure, one can clearly observe the variation of the morphology of samples produced at different ϕ, and the existence of CNTs (indicated by arrows) and nanoparticles formed during the synthesis. In general, the majority of the as-produced nanomaterials is crystalline nanoparticles of characteristic size of 20–100 nm, and CNTs are loosely distributed upon them. At $\phi = 1.0$ and 1.05, CNTs are seen to exist on or beneath the nanoparticles, tending to form a net or web-like structure (see Fig.5.5.(a)-(d)). Instead, one starts to see loosely-bonded nanoparticle aggregates prevailing in the solid products at $\phi = 1.1$. Theses aggregates tend to stack together and form large clumps in which CNTs are likely embedded underneath, reflecting the highly limited quantity of CNTs formed at this condition.

After closer examination of the images, the diameters of CNTs or CNT bundles formed at $\phi = 1.0$ and 1.05 were determined using a built-in measurement tool provided by the SEM system. It is found that the diameters of the CNTs formed at both conditions are of the order of ~10 nm, whilst their lengths can vary from 10 nm up to 1 μm. However the measured results should be treated only as a reference rather than an accurate number due to the intrinsic limitations of SEM technique. The measurements of SEM images are usually performed manually and may be affected by parameters such as contrast, brightness and resolution of a image. A more accurate measurement technique for nanoparticles and CNTs can resort to transmission electron microscopy (TEM), which is a highly sophisticated but more expensive method for characterising nanomaterials.

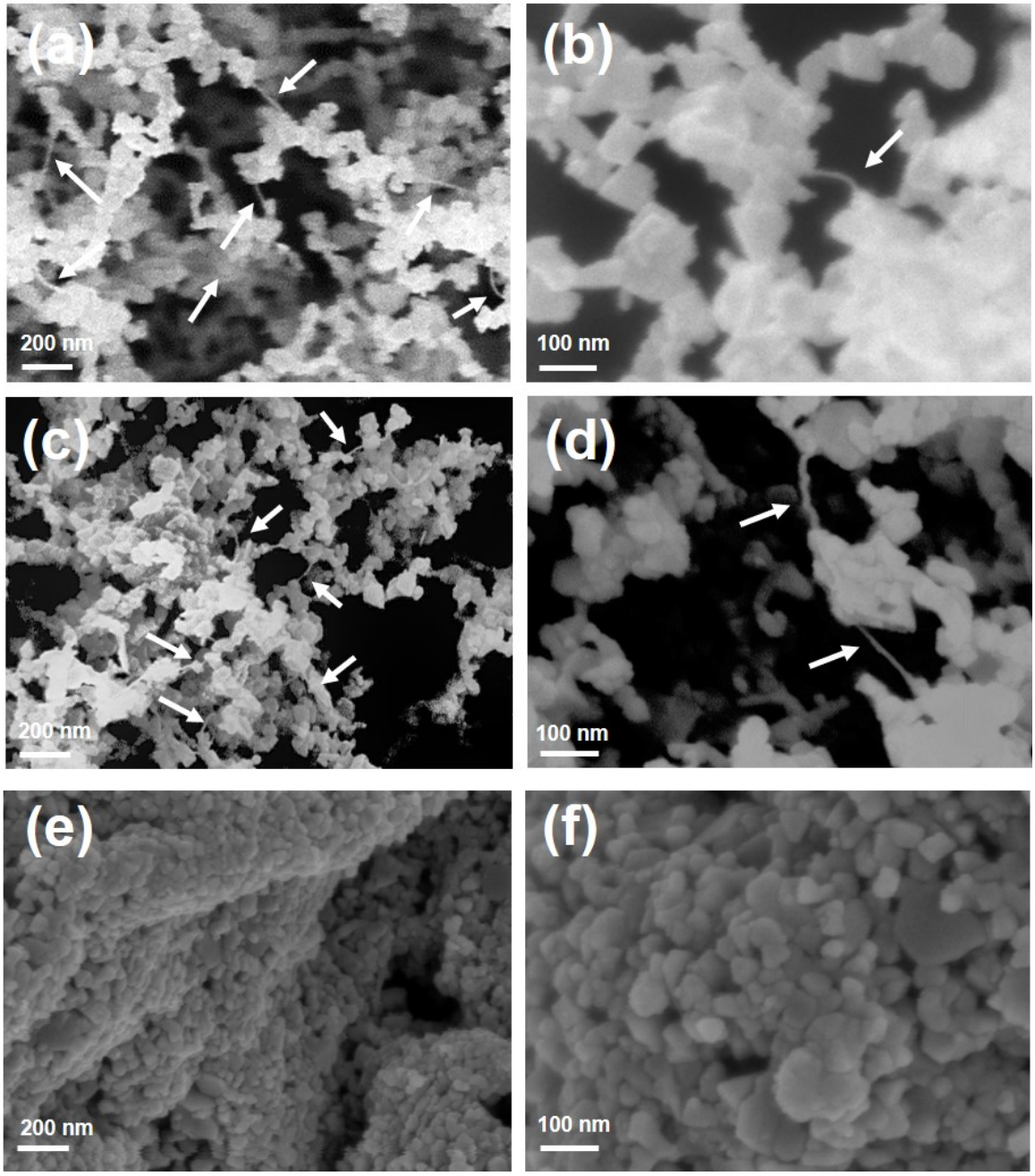

Fig. 5.5 SEM images of the nanomaterials produced at different ϕ: (a)–(b) at $\phi = 1.0$, (c)–(d) at $\phi = 1.05$ and (f)–(e) at $\phi = 1.1$.

The crystalline nanoparticles formed during synthesis exhibit different shapes including triangle, sphere, square and diamond as shown in Fig.5.5. The composition of these particles are believed to be a mix of elemental iron, iron oxides, and other compounds. There likely exist a large proportion of Fe_3O_4 (magnetite) nanoparticles which are evident by the Raman spectra in Fig.5.2. The size of nanoparticles formed at different ϕ are generally around ~50 nm, maybe larger or smaller. However, the distribution pattern of these nanoparticles is seen to vary with ϕ. At smaller ϕ, *e.g.* 1.0 and 1.05, these particles are radially bonded into small clusters which seem to participate in constructing the web-like structures with CNTs. Therefore it results in a filamentous morphology rather than stacking into clumps as shown in Fig.5.5.(e) and (f) at $\phi = 1.1$. The causes for this phenomenon may attribute to a higher yield of CNTs at $\phi = 1.0$ and 1.05 than the other conditions due to a higher synthesis temperature as shown in Fig.5.4. These CNTs produced in a larger quantity are more easily entangled to form a web with nanoparticles attached.

5.2.2.4 EDX analysis

In order to identify the elements present in the materials, we carried out an analysis using the energy dispersive X-ray (EDX) while doing SEM. Fig.5.6 shows the EDX spectrum and the SEM image of the area where EDX was performed. From the spectrum, C, F, O, Fe, Au and Pd elements are identified. Since the analysis was conducted directly on the PTFE filters, F element was therefore detected as the PTFE has the chemical formula of $(C_2F_4)_n$ comprising both C and F elements. The appearance of Au and Pd elements is due to the sputtering coating as described in Section 5.2.2.3.

Table 5.2 presents the weight and atomic fractions of each element identified by EDX. It shows that Fe occupies the majority of the mass of the materials, nearly half of the total weight. while in terms of atomic fractions, C, O ,F and Fe elements become comparable. However, limitations of the standard EDX restrict our quantitative investigation on these elements, particularly C, O and F. This is due to the fact that quantitative measurements by EDX of light elements with atomic number smaller than 11 becomes considerably difficult as the X-rays generated from these atoms are generally at low energies, and thus are prone to absorption by surrounding environment [134]. Therefore, the above results shall only be used as a qualitative analysis which can only show the existence of these elements rather than their actual proportions.

Table 5.2 EDX results for the materials produced at $\phi = 1.1$ corresponding to the experimental condition A3 in Table 5.1.

Element	Weight %	Standard deviation σ	Atomic %
C	8.96	1.16	22.66
O	14.16	0.34	26.90
F	14.09	0.64	22.53
Fe	45.57	0.79	24.79
Pd	3.56	0.3	1.02
Au	13.66	0.47	2.11

5.2.3 Effect of feedstock injection and carrier flow rates

The previous section has discussed the impacts of ϕ of the premixed H_2/air flames on the synthesis, and it is found that the synthesis temperature is a key parameter for a successful CNT formation. While the feedstock injection rate, or the carbon loading, and the carrier gas flow rate may also influence the CNT production. We therefore carried out a series of experiments to investigate how the variation of the injection flow rate $\dot{q}$, or carbon loading, and the carrier flow rate $\dot{V}_{Ar}$ might affect the CNT production.

Table 5.3 Experimental conditions for the study of the effect of injection rates $\dot{q}$. The H_2/air flame was fixed at $\phi = 1.05$ and the feedstock consisted of 99.0 wt.% ethanol and 1.0 wt.% ferrocene.

Test No.	$\dot{q}$ (ml/min)	$\dot{m}_C$ (g/min)	$\dot{V}_{Ar}$ (slpm)	u_c (slpm)	$u_c/u_b{}^*$
B1	0.1	0.08	0.1	12.8	0.2
B2	0.3	0.24	0.1	19.9	0.4
B3	0.5	0.39	0.1	27.0	0.5
B4	0.7	0.55	0.1	34.1	0.6
B5	1.0	0.79	0.1	44.7	0.8
B6	1.5	1.18	0.1	62.5	1.1
B7	2.0	1.58	0.1	80.2	1.5

* u_b: surrounding flow velocity.

Table 5.3 lists the experimental conditions for the present study. Premixed H_2/air flames at $\phi = 1.05$ were used as the heat source and the feedstock consisting of 99.0 wt.% ethanol and 1.0 wt.% ferrocene was injected through the central tube at different rates. The argon flow was fixed at 0.1 slpm to carry the vaporised ethanol and ferrocene mixtures into the synthesis region. The central flow velocity u_c was calculated given the central tube of 6 mm inner diameter and at 100 °C. The velocity of the surrounding bath flow coming out of the

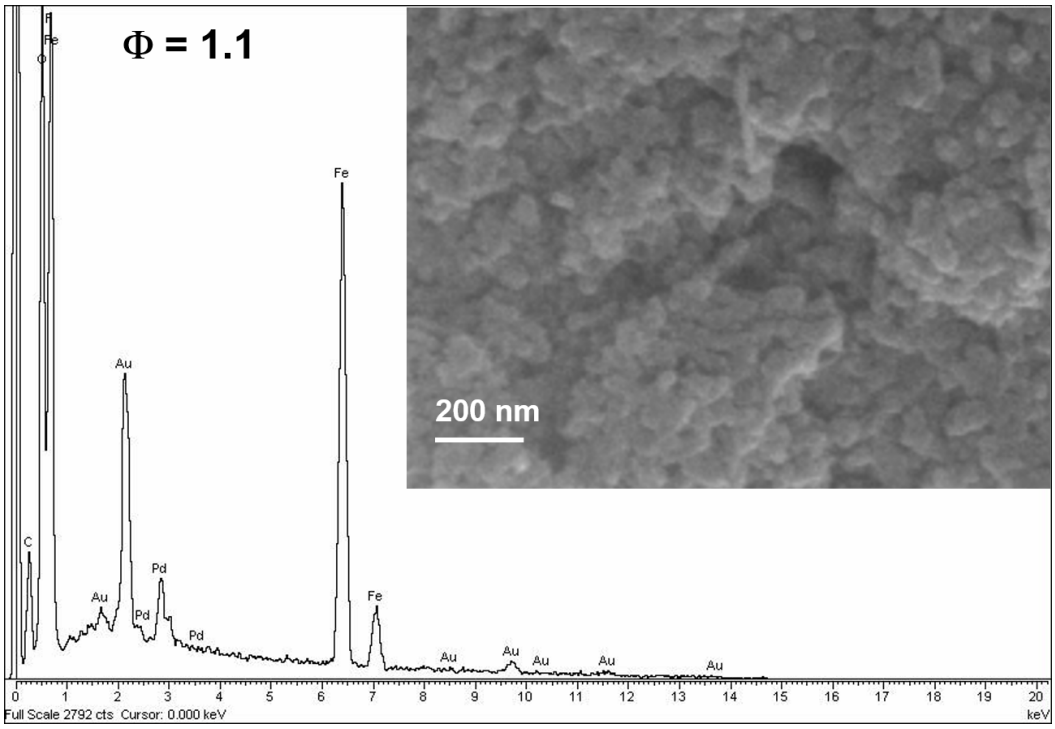

Fig. 5.6 EDX spectrum and SEM image of the nanomaterials produced at $\phi = 1.1$.

premixed flame u_b was calculated based on the condition of Test A2 shown in Table 5.1, given a flame temperature of 1400 °C and the quartz tube of 70 mm inner diameter, which was hence determined as 55 cm/s.

5.2.3.1 Feedstock injection rate

Fig.5.7.(a) shows the normalised mean Raman spectra of the materials produced at different injection rates $\dot{q}$ from 0.1 up to 2.0 ml/min. In general, the G-band and the RBM can be seen at all $\dot{q}$ with varying I_G/I_D ratios, except for that at $\dot{q} = 0.1$ ml/min where neither the Raman features of CNTs nor those of carbon allotropes can be observed. However, the case at $\dot{q} = 0.1$ ml/min is still of particular interest, as it emphasises the ease of formation of magnetite, and possibly other forms of iron oxides, as the peak at 670 cm^{-1} associated with magnetite stands out rather than that of CNTs at this condition. The optimum condition at which the Raman spectrum possesses the most distinct features of CNTs occurs at $\dot{q} = 0.5$ ml/min compared with the "worst" case at $\dot{q} = 0.1$ ml/min. The band associated with magnetite at 670 cm^{-1} are observed for all $\dot{q}$ of different normalised intensities, while it has the lowest normalised intensity at $\dot{q} = 0.5$ ml/min, followed by $\dot{q} = 0.3$ ml/min. Beyond $\dot{q} = 0.5$ ml/min, the Raman spectra share a similar pattern where a broadened G-band and an enhanced D-band are clearly seen. The increase of the D-band is due to the existence of defects or amorphous

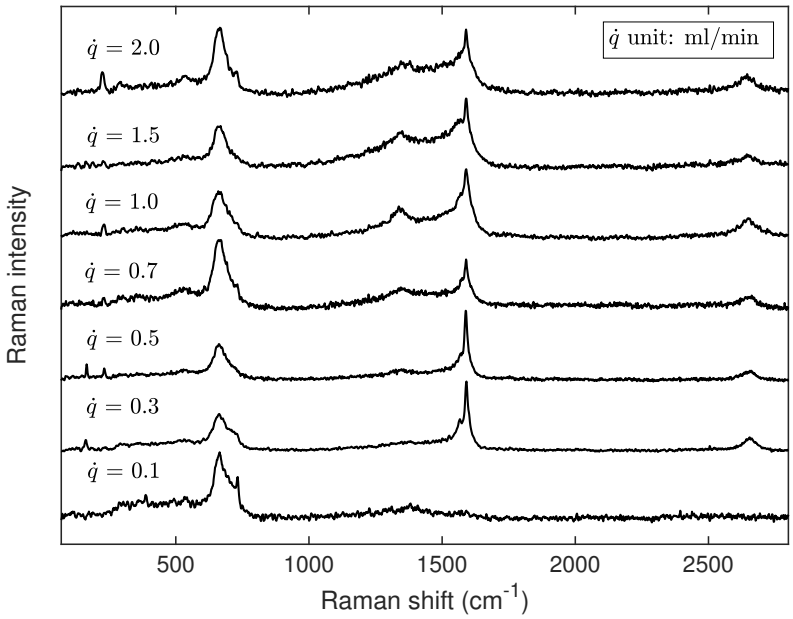

(a) Raman spectra over different injection rates $\dot{q}$ (ml/min).

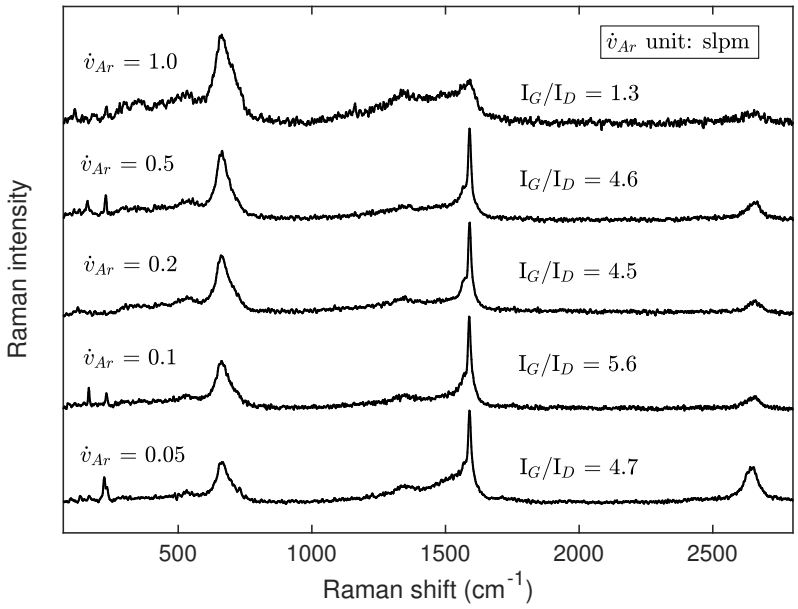

(b) Raman spectra over different carrier gas flow rates $\dot{V}_{Ar}$ (slpm).

Fig. 5.7 Normalised Raman spectra of the samples produced at $\phi = 1.05$ as a function of (a) different injection rates $\dot{q}$ from 0.1 to 2.0 ml/min, and (b) different carrier gas flow rates $\dot{V}_{Ar}$ from 0.05 to 1.0 slpm. The feedstock used for the synthesis consisted of 99.0 wt.% ethanol and 1.0 wt.% ferrocene.

carbon impurities. Moreover, the signals from the nanomaterials at $\dot{q} > 0.5$ ml/min are seen to attenuate compared with those at 0.3 ml/min and 0.5 ml/min, providing an indication of an decreased yield of CNTs at higher $\dot{q}$. Furthermore, the normalised intensity of the featured peak of magnetite at around 670 cm^{-1} becomes more pronounced at $\dot{q} > 0.5$ ml/min, signalling an increased yield of iron oxides.

The findings above show a threshold value of $\dot{q}$ at ~0.5 ml/min. Below this point, there is an increased proportion of CNTs over iron oxides with the increase of $\dot{q}$, while a decreased production of CNTs shall be seen if above 0.5 ml/min. And the cause of this likely attributes to the shortened residence time τ due to the higher flow velocities shown in Table 5.3. The variation of $\dot{q}$ inevitably results in a change of the central flow velocity u_c, and thus the u_c/u_b ratio. Since the change of the ratio is accompanied by the variation of carbon loading $\dot{m}_C$, it is hard to determine whether it is u_c/u_b or $\dot{m}_C$ that mostly affects the CNT synthesis. Therefore, we carried out a further experimental study by changing the flow rate of the carrier gas $\dot{V}_{Ar}$ while keeping $\dot{q}$ fixed at 0.5 ml/min, or the carbon loading $\dot{m}_C$ at 0.39 g/min, to answer the question above.

5.2.3.2 Carrier flow rate

Table 5.4 Experimental conditions for the study of the effect of carrier gas flow rates $\dot{V}_{Ar}$. The H_2/air flame was fixed at $\phi = 1.05$ and the feedstock consisted of 99.0 wt.% ethanol and 1.0 wt.% ferrocene.

Test No.	$\dot{V}_{Ar}$ (slpm)	u_c (cm/s)	u_c/u_b*
C1	0.05	22.4	0.4
C2	0.1	27.0	0.5
C3	0.2	36.2	0.7
C4	0.5	64.0	1.2
C5	1.0	110.2	2.0

* u_b: surrounding flow velocity.

Table 5.4 lists the experimental conditions of the study. The carrier flow rate $\dot{V}_{Ar}$ was varied from 0.05 up to 1.0 slpm, with u_c/u_b changing from 0.4 to 2.0, respectively. The ϕ of the H_2/air flame and the composition of the feedstock injected into the flame were kept unchanged. Fig.5.7.(b) shows the normalised Raman spectra of nanomaterials synthesised at different $\dot{V}_{Ar}$. In general, the variation of $\dot{V}_{Ar}$ shows little effect on the CNT synthesis at $\dot{V}_{Ar} < 1.0$ slpm. These Raman spectra exhibit a similar pattern with the Raman features of CNTs clearly being observed, and the associated I_G/I_D ratios are all at around 5.0, which indicates a production of CNTs with a possible good quality. In contrast, the Raman

Table 5.5 Experimental conditions for the study of the effect of mass flux $\dot{m}''$. The H_2/air flame was fixed at $\phi = 1.05$ and the feedstock consisted of 99.0 wt.% ethanol and 1.0 wt.% ferrocene.

Test No.	H_2 (slpm)	Air (slpm)	CH_4 (slpm)	Total flow rate $\dot{V}$ (slpm)	Mass flux $\dot{m}''$ (kg m^{-2} s^{-1})
D1	3.5	8.4	0.05	11.9	0.13
D2	5.3	12.5	0.08	17.9	0.19
D3	7.0	16.7	0.10	23.8	0.26
D4	10.5	25.0	0.15	35.7	0.39

spectrum at $\dot{V}_{Ar} = 1.0$ slpm shows poorer features of CNTs, pointing out a decreased yield of nanomaterials and an increased proportion of amorphous carbon.

Compared with the previous study, it shows that $\dot{V}_{Ar}$ has negligible impact on the CNT synthesis compared to $\dot{q}$ (directly associated with $\dot{m}_C$ shown in Table 5.3) given at the same u_c/u_b. Therefore, one can conclude that the CNT synthesis is primarily controlled by $\dot{q}$ rather than $\dot{V}_{Ar}$ within the range considered here. However, large u_c/u_b (> 1.2) either induced by the change of $\dot{m}_C$ or $\dot{V}_{Ar}$ should be avoided as it leaves little τ for the central stream to absorb heat and pyrolyse at the hot region, resulting in the formation nanoparticles rather than CNTs.

5.2.4 Effect of mass fluxes

Another important parameter controlling the combustion synthesis is the overall flow rate $\dot{V}$, or the mass flux $\dot{m}''$, of the H_2/air mixtures. Not only does it determine the residence time of the reacting flows but it also affects the heat loss to the cold burner, and thus the actual flame temperature. We thereby started with the mixture at $\phi = 1.05$ consisting of 3.5 slpm H_2 and 8.4 slpm air. Again, the mixture was doped with a tiny fraction of CH_4 (~0.4 vol.% in mixtures) as a safety precaution. This mixture led to an estimated τ of ~1 s in the post-flame region, given a 250 mm length quartz tube with a 70 mm inner diameter at 1200 °C.

Table 5.5 shows the experimental flow conditions for the study of the influence of $\dot{m}''$. Test D1 is the standard condition, corresponding to the lowest overall flow rate, whereas the overall flow rate of Test D2–D4 are 1.5, 2 and 3 times of the standard condition, respectively.

Fig.5.8 shows the normalised Raman spectra of the as-produced samples at conditions listed in Table 5.5. Generally, the Raman signals from the as-produced materials shown on the spectra increase with the increase of $\dot{V}$, or $\dot{m}''$, and the background noise becomes diminished from Test D3 onwards. It is seen that the spectrum of Test D1 shows the "poorest" shape compared with those of the other conditions. At this condition, neither the G-band

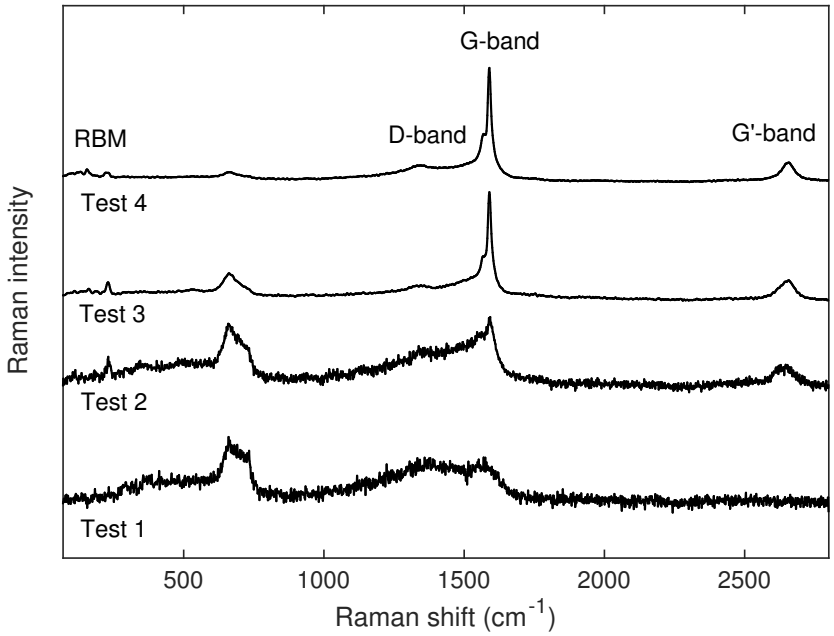

Fig. 5.8 Normalised Raman spectra of the samples produced at different $\dot{m}''$ as listed in Table 5.5 at $\phi = 1.05$. The feedstock consisted of 99.0 wt.% ethanol and 1.0 wt.% ferrocene. Test D1 indicates the standard condition which corresponds to the smallest $\dot{m}''$ of 0.13 kg m^{-2} s^{-1}, whereas Test D2, D3 and D4 have an increased overall flow rate corresponding to 1.5, 2 and 3 times of the standard value, respectively.

(~1590 cm^{-1}) nor the D-band (~1350 cm^{-1}) can be clearly observed, let alone the RBM at lower frequencies. The band associated with magnetite at ~670 cm^{-1} and an shoulder at 731 cm^{-1} originating from the PTFE substrate indicate a lowered overall yield and an absence of CNTs in the products. With the increase of $\dot{m}''$, the feature peak originated from the PTFE substrate at 731 cm^{-1} diminishes, and the CNT Raman features *i.e.* the G-band, D-band, RBM and G'-band start to appear. Meanwhile the normalised intensity of the band of magnetite decreases markedly as $\dot{m}''$ increases. It appears that higher $\dot{m}''$ favours the formation of CNTs rather than the opposite. The Raman intensity ratios of the G-band to D-band, I_G/I_D, were determined for D3 and D4 as 8.33 and 10.0, respectively, showing that Test D4 produced a better quality of CNTs than Test 3.

To understand the causes for this variation, we resorted to the 1-D flame computational analysis, and the burner stabilised flame temperatures were hence calculated for the mixtures as listed in Table 5.5. The boundary conditions were set to an inlet temperature of 25 °C, and at atmospheric pressure. Fig.5.9 summaries the calculated burner stabilised flame temperatures T_b as a function of different $\dot{m}''$. It shows that T_b increases monotonically with the increase of $\dot{m}''$. Therefore, the premixed flame temperature in Test D4 with $\phi = 1.05$

has a temperature of ~1600 °C. This temperature is more favourable for producing CNTs not only in a larger quantity but also of longer lengths. Moreover, it helps moderate the proportions of CNTs against nanoparticles, producing CNTs with fewer nanoparticles and thus a higher I_G/I_D ratio, compared to the other conditions. The above findings show that the flame temperature dominantly controls the inception, growth and the quality of CNTs during the combustion synthesis, while the residence time τ seems to be a secondary parameter compared to flame temperatures.

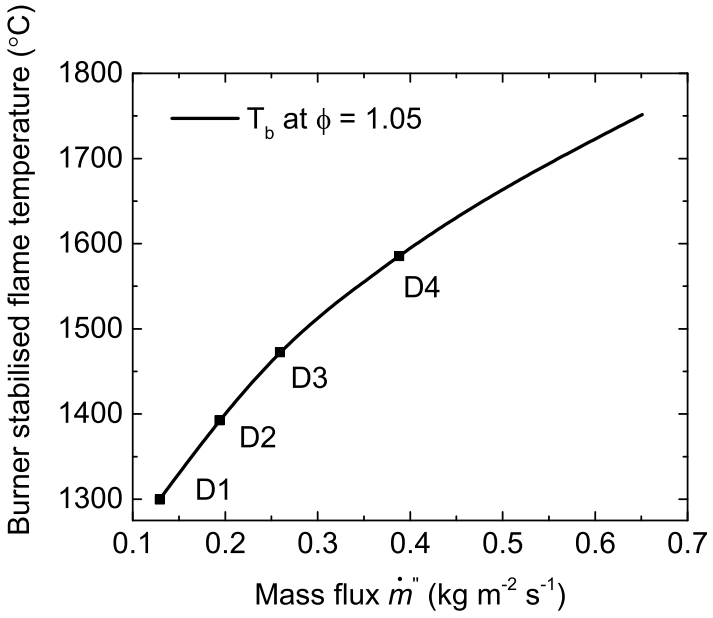

Fig. 5.9 Variation of burner stabilised flame temperatures T_b as a function of different mass flux $\dot{m}''$ at $\phi = 1.05$ and atmospheric pressure, and at an inlet temperature of 25 °C.

A detailed examination of the materials collected at different $\dot{m}''$ was carried out using SEM. Fig.5.10 shows the SEM images of the materials collected at Test D2-D4, corresponding to Fig.5.10.(a)–(c), respectively. The morphology of the products synthesised at Test D1 highly resembles that of Test D2, and therefore not included in the figure. Generally, these images clearly exhibit the change in morphology of the materials with the increase of $\dot{m}''$. At Test D2, the mean flow velocity in the synthesis region is of the order of 50 cm/s, yielding a residence time τ of ~0.5 s in the hot zone. The relatively longer τ at Test D2, however, leads to a production of solid nanoparticles in various shapes instead of CNTs as observed in Fig.5.10.(a). These particles tend to accumulate into thick and dense clumps, making it extremely difficult to find even a single CNT fibre. Although the Raman spectrum reveals that there exist some graphitic carbon structures in the samples as the G-band and G'-band are seen from the spectrum, the SEM images, however, show that the synthesis

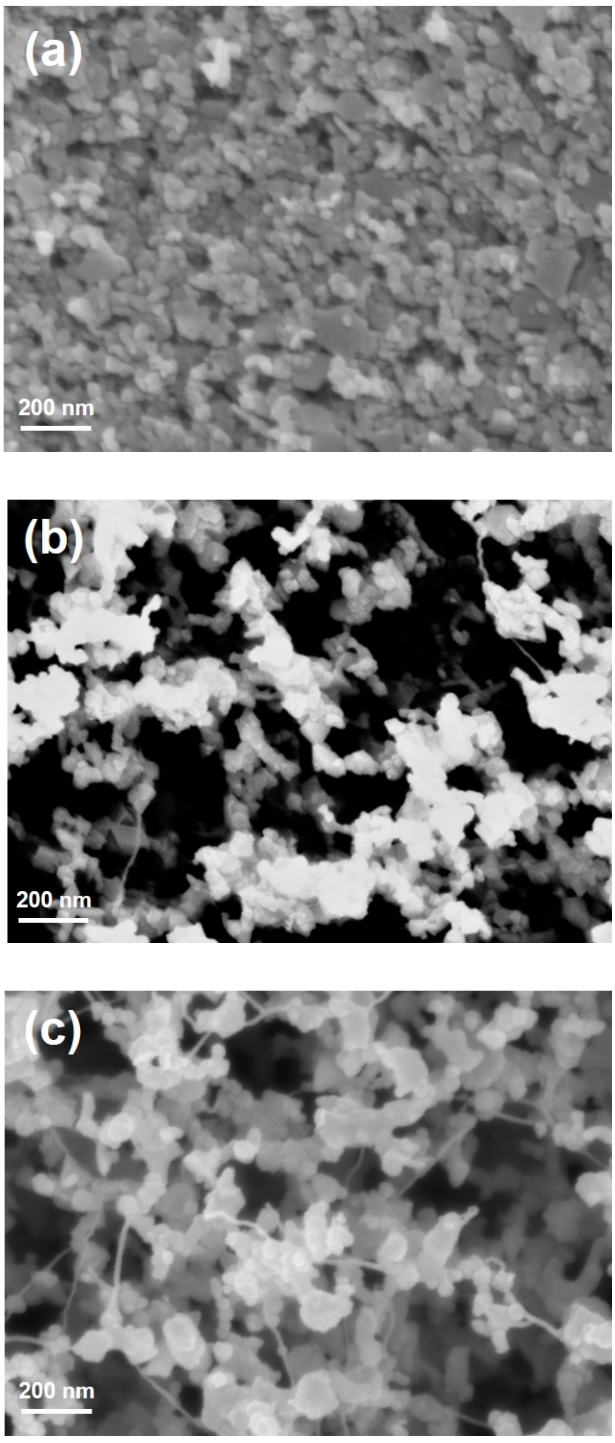

Fig. 5.10 SEM images of the samples produced at $\phi = 1.05$ over different $\dot{m}''$ from Test D2–D4 in Table 5.5, corresponding to (a)–(c), respectively. The feedstock consisted of 99.0 wt.% ethanol and 1.0 wt.% ferrocene. .

of CNTs is not favoured at this condition. In contrast, one can observe CNTs at Test D3 and D4, although τ at these conditions are generally shorter, 0.45 s and 0.3 s, respectively. The morphologies of samples collected at the two conditions share a similar pattern where CNTs form a web-like structure with nanoparticles attached. This type morphology is rather different from those produced at a lower flow rate, indicating an increased yield of CNTs at a higher rate. More specifically, it appears that the overall yield of CNTs formed at Test D4 are even larger than that at Test D3. As seen in Fig.5.10.(c), CNTs are more easily detected and distributed more densely than at Test D3. Moreover, the web-like structure is more clearly observed in contrast to those shown in Fig.5.10.(b). According to the direct measurements on the SEM images, it is found the diameters of the CNTs in Fig.5.10.(b) and (c) are all of the order of 10 nm, while the later posses much longer lengths.

5.3 Conclusion

In this study, we have successfully demonstrated the feasibility of producing CNTs using the floating catalyst flame synthesis method on the present experimental setup. Premixed H_2/air flames at different ϕ were used as the heat source, while carbon and iron were supplied by ethanol and ferrocene, respectively. The results are summarised as follows:

1. Flame temperatures are key to a successful CNT synthesis, and operating at ϕ close to the stoichiometry point is highly recommended. In addition, a rich mixture ($\phi > 1$) was found more favourable for producing CNTs as no oxygen was left in the pyrolysis zone, thus avoiding rapid oxidation of the catalyst nanoparticles and also reducing the tendency of making soot.

2. The effects of feedstock injection and carrier gas flow rates were investigated, and it was found that the CNT synthesis is less sensitive to the variation of the velocity ratio of centrally injected feedstock to the surrounding hot gases, u_c/u_b, due to the change of carrier gas flow rates. Rather, the carbon loading $\dot{m}_C$, or the liquid injection rate $\dot{q}$, has a much greater influence on the synthesis. An optimum range of carbon loading $\dot{m}_C$ was found to be 0.2–0.4 g/min.

3. The mass flux $\dot{m}''$, or the total flow rates $\dot{V}$ of the H_2/air mixtures was found to largely influence the synthesis of CNTs via a change in temperature. The quantity and the length of the CNTs were found to increase with the increase of $\dot{m}''$, in spite of shorter residence times. With the assistance of the numerical calculations, the cause was found due to the elevated flame temperature T_b as a result of the increased $\dot{m}''$. The influence of residence time appears to be negligible compared with the change in temperature.

Chapter 6

Flame Synthesis of CNTs: A Study of Catalyst Precursors

6.1 Introduction

The previous chapter has discussed the effects of flame temperatures, residence times and carbon loading on the synthesis of CNTs. Here, we consider how the variation of the proportions of catalyst precursors in the feedstock might affect the CNT production.

It is widely acknowledged that catalyst precursors are key to the successful synthesis of CNTs. Metal precursors typically in the form of metallocenes such as ferrocene, cobaltocene, and nickelocene are the most frequently used catalyst reactants for producing CNTs [135]. The role of these catalysts has been extensively studied. The widely-accepted consensus on the role of these metal precursors is that the breakdown of these precursors liberates nanoparticles whose surfaces contain many active catalyst sites suitable for the inception and growth of CNTs. In addition, non-metal catalyst precursors are also used in many studies for promoting CNT production, among which thiophene has been found as an effective addition, particularly in CVD processes[135, 41, 98, 136]. However, to the best of our knowledge, rarely has the role of sulphur in CNT production been investigated in combustion synthesis scenarios. The following questions arise: does adding sulphur (thiophene) into a combustion system for CNT production have the same effectiveness as that in a CVD reactor? And what might be the differences between these two processes regarding the addition of ferrocene and thiophene?

Herewith we carried out investigations of the role of all the catalyst precursors used in the present study, ferrocene and thiophene, by varying their respective proportions in the

ethanol solvent (the carbon source), and equivalence ratios ϕ of the premixed H_2/air flames to study their impacts on combustion synthesis of CNTs.

6.2 Experimental

The details of the premixed flame burner and the related apparatus have been described in Chapter 4. In the present study, premixed H_2/air flames doped with a small amount of methane (0.4 vol.% in mixtures as a safety precaution) were used to provide the heat for the CNT synthesis, and the background flame equivalence ratios ϕ were varied from 1.05 up to 1.2 to study the effect of ϕ on the synthesis. The feedstock injected through the central tube consisted of ethanol as the carbon source and the solvent for dissolving catalyst precursors. Varying amounts of ferrocene (Sigma-Aldrich) and thiophene (Sigma-Aldrich) were added and mixed in the solvent for the subsequent study of their role in the CNT synthesis. The feedstock and the carrier gas flow were fixed at $\dot{q} = 0.5$ ml/min and $\dot{V}_{Ar} = 0.1$ slpm, respectively. This combination of parameters has been found as an optimal conditions by the parametric study in Chapter 5. The products synthesised in the post-flame region were collected on a PTFE membrane filter for a controlled period of time via the sampling unit at a fixed HAB = 230 mm. The as-produced solid materials on the filters were then analysed by various techniques including Raman spectroscopy, scanning electron microscopy and transmission electron microscopy.

6.2.1 Ferrocene study

Feedstocks containing 6 different mass fractions of ferrocene y_{Fe} were used, corresponding to F1–F6 with y_{Fe} from 0.1 to 3.0 wt.% as listed in Table 6.1. Prior to the synthesis experiments, the feedstock sealed in plastic containers was sonicated for 15 min in a warm bath (~35 °C) to assist with the full dissolution of ferrocene powder in the ethanol solvent. Premixed H_2/air flames were used to provide heat to the synthesis and their equivalence ratios ϕ were varied from 1.05 to 1.2 for each feedstock study, corresponding to the flow rates of A2–A5 listed in Table 5.1 in Chapter 5. The sampling time for each condition was 2 min. For the Raman spectroscopy, the Raman signals were collected at three different locations on the filter in the wavenumber range of 70–2800 cm^{-1}. Each Raman signal was normalised against its global peak value, and the resulting normalised Raman spectra at all three different sites were then averaged, yielding the mean Raman spectrum for the subsequent analysis and comparisons.

Table 6.1 Experimental conditions for the study of ferrocene with varying mass fraction y_{Fe} in feedstock. ϕ was varied form 1.05–1.2, and the feedstock was injected at 0.5 ml/min and carried by argon at 0.1 slpm.

Feedstock No.	Ethanol (wt.%)	Ferrocene (wt.%)
F1	99.9	0.1
F2	99.7	0.3
F3	99.5	0.5
F4	99.0	1.0
F5	98.0	2.0
F6	97.0	3.0

Table 6.2 Experimental conditions for the study of thiophene with varying mass ratios of sulphur to iron elements, $m_{S/Fe}$. ϕ was varied from 1.05–1.2, and the feedstock was injected at 0.5 ml/min and carried by argon at 0.1 slpm.

Feedstock No.	$m_{S/Fe}$	Thiophene (wt.%)	Ferrocene (wt.%)	Ethanol (wt.%)
S0	0	0	1.0	99.0
S1	0.1	0.1	1.0	98.9
S2	1.0	1.5	2.3	96.2
S3	2	1.6	1.0	96.4
S4	5	2.0	0.5	97.5
S5	10	2.0	0.25	97.75

6.2.2 Thiophene study

We started the experimental investigation of the role of sulphur by using the feedstock containing various proportions of ferrocene and thiophene which were all dissolved and mixed with the ethanol solvent. The details of the feedstock used for the study are listed in Table 6.2. Each feedstock was injected at a rate of 0.5 ml/min and carried by a stream of argon at $\dot{V}_{Ar} = 0.1$ slpm. Premixed H_2/air flames at $\phi = 1.05 - 1.2$ were used to supply heat for the synthesis and the as-produced samples were then collected at HAB = 230 mm on the PTFE membrane filters for 6 min via the sampling unit before being characterised by various techniques. The data processing for the Raman spectra of all the samples followed the same procedure as those described in Section 6.2.1.

For the TEM study, the collected materials on the PTFE filter was firstly immersed in pure ethanol (VWR Chemicals Ethanol absolute $\geq 99.8\%$) and sealed in a glass vial before being sonicated for 5 hrs at 30 °C. After that, the PTFE filter was taken out, and the well-dispersed solution was used for the following TEM analysis.

6.3 Results and discussion

6.3.1 Effect of iron catalyst

This section summarises the results of the samples produced using different feedstocks containing varying y_{Fe} and at different ϕ. The properties of the as-produced materials were characterised by different techniques, which are illustrated in the following sections.

6.3.1.1 Raman spectroscopy analysis

The materials collected on the PTFE filters were first taken for examinations by Raman spectroscopy, which is a fast and reliable tool for identifying the presence of CNTs. Fig.6.1 shows the normalised mean Raman spectra of samples produced using different feedstocks with varying y_{Fe} at ϕ from 1.05 to 1.20 in the range of 70–2800 cm^{-1}.

At $\phi = 1.05$, which corresponds to the highest synthesis temperature (~1400 °C based on the modelling results), the Raman spectra for all the feedstocks look very similar. The sharp and distinct G-band at ~1590 cm^{-1} and the RBM feature at lower wave numbers (< 300 cm^{-1}) can be clearly observed on all the Raman spectra, showing the evidence of CNTs. In addition, the band associated with magnetite at 670 cm^{-1} also appears for all the conditions, and its normalised intensity shows a weak proportional relationship with y_{Fe} *i.e.* a higher y_{Fe} leads to a higher normalised intensity. This may indicate an increased yield of iron oxides with the increase of y_{Fe}. Moreover, based on the observations, there is little evidence showing a discernible relationship between the changes in the normalised intensity of the D-band, or the intensity ratio of G-band to D-band, I_G/I_D, and the the change of y_{Fe}. As seen in Fig.6.1.(a), the materials produced at $y_{Fe} = 3.0$ wt.% have the highest I_G/I_D ratio, 5.71, compared with the lowest $I_G/I_D = 2.33$ at $y_{Fe} = 2.0$ wt.%. However, it must be pointed out that I_G/I_D and the shape of the Raman spectra are affected by the uncertainty originated from the choice of sites where Raman spectroscopy is performed as CNTs may not be homogeneously distributed on the filter. It can still be deduced that there is no strong evidence showing the link connecting the Raman signatures of CNTs with y_{Fe} of the feedstock within the range considered.

A similar indifference to y_{Fe} is apparent at richer ϕ, as shown in Figs.6.1.(b)–(c). The general shape of the Raman spectra for different y_{Fe} appears unchanged, and is primarily determined by ϕ *i.e.* the flame temperatures rather than y_{Fe}. Generally, the CNT Raman features become weaker with the increase of ϕ from 1.05 to 1.2 as indicated by the decreased I_G/I_D and the increased normalised intensity of the band associated with magnetite. Also can be seen is the rise of the Raman peak associated with the PTFE filters at 731 cm^{-1} and

1380 cm^{-1} (shown in Fig.5.1) in Fig.6.1.(b) and (c), particularly for the spectra with lower y_{Fe}. This indicates a lowered yield of nanomaterials, both iron oxides and carbon solids, at these conditions because the background signal coming from the PTFE filter stars to appear and interfere with the results.

The effect of varying y_{Fe} in the feedstock using ethanol as the carbon source on CNT synthesis has also been studied in FCCVD synthesis. According to the literature, it is reported that a composition where ferrocene mass fraction y_{Fe} falls in the range of 0.2–2.5 wt.% [34, 42] while using ethanol as the solvent is suitable for making CNTs, even aerogels, albeit small amount of thiophene is doped in these studies. Given the fact that y_{Fe} in has little impact on the synthesis of CNTs within the range of y_{Fe} considered here, one may conclude that as long as there exists a iron precursor in a carbon source, a fraction of the precursor, large or small, can decompose into catalyst nanoparticles for the inception of CNTs given at a suitable synthesis temperature. The leftover iron atoms, on the other hand, preferably combine with oxygen to form iron oxides, appearing in relatively large quantity in the as-produced samples, due to the presence of H_2O.

6.3.1.2 Bright-field microscopy

Fig.6.2 shows the light microscopic images of samples depositing on the PTFE membrane filters, which were taken by using an x50 objective equipped in the Raman spectroscopy system. The samples shown in Fig.6.2.(a) were produced at $\phi = 1.05$ over different y_{Fe} in the range of 0.1–3.0 wt.%. The shadowed/dark sites indicate the presence of solid deposits while the bright area are the surface of the PTFE substrates. In general, the morphology of deposits on the membrane filters varies with different y_{Fe}. The distribution of deposits at $y_{Fe} = 0.1$ wt.% resembles that at 1.0 wt.% in a way that small clusters of products in dotted shape are evenly distributed on the substrate, whereas the latter is more densely stacked. When y_{Fe} reaches 2.0 wt.%, one observes deposits in a short stripe-like shapes, which become more densely packed into large stripes at 3.0 wt.%.

Fig.6.2.(b) illustrates the distribution pattern of samples on the filters produced at different ϕ from 1.05 to 1.20 using the feedstock F6 with y_{Fe} = 3.0 wt.% (see Table 6.1). These images, as a typical representation of the morphology change over different ϕ, show the changes of the overall yield with the increasing ϕ from a qualitative perspective. At ϕ = 1.05, the deposits are shaped into large and dense stripes, exhibiting a porous-like texture. As ϕ increases (temperatures decrease), the deposits become less densely packed and break into tiny spots. From these images, it can be deduced that the yield of solid products decreases with the increase of ϕ, indicating the flame temperature is a dominant factor not only controls

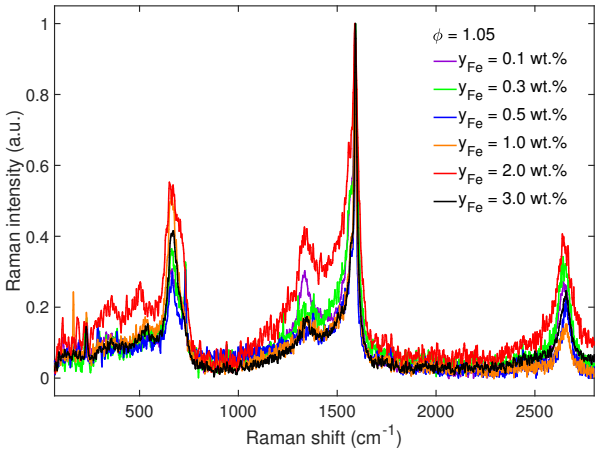

(a)

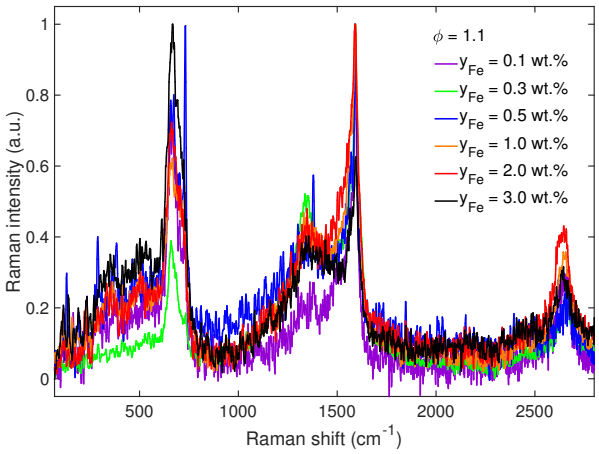

(b)

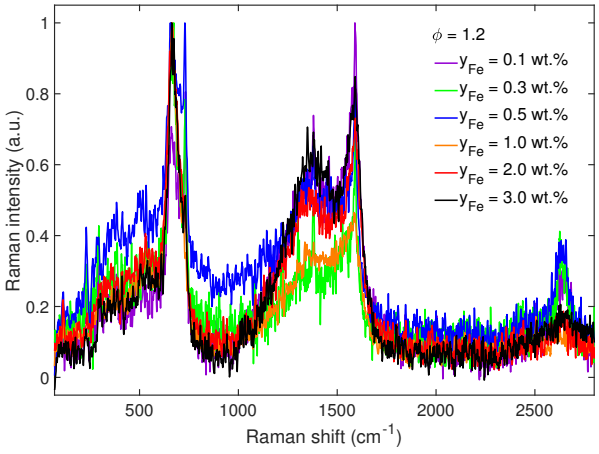

(c)

Fig. 6.1 Normalised Raman spectra of the samples produced using the feedstock containing various mass fractions of ferrocene y_{Fe} at different ϕ of (a) 1.05, (b) 1.1 and (c) 1.2.

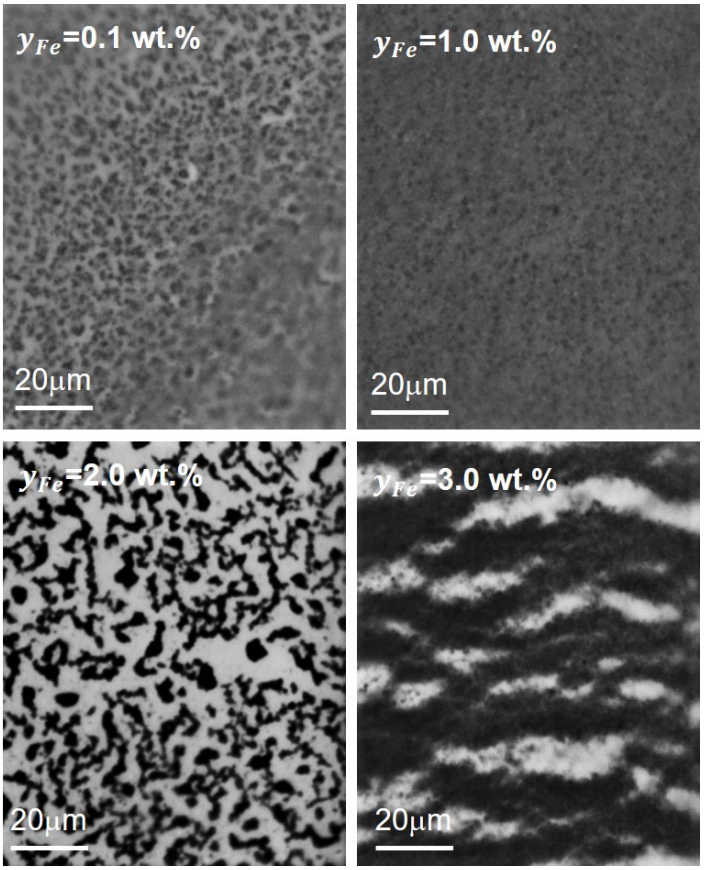

(a) Bright-field microscopy images of the samples for different y_{Fe} at ϕ = 1.05.

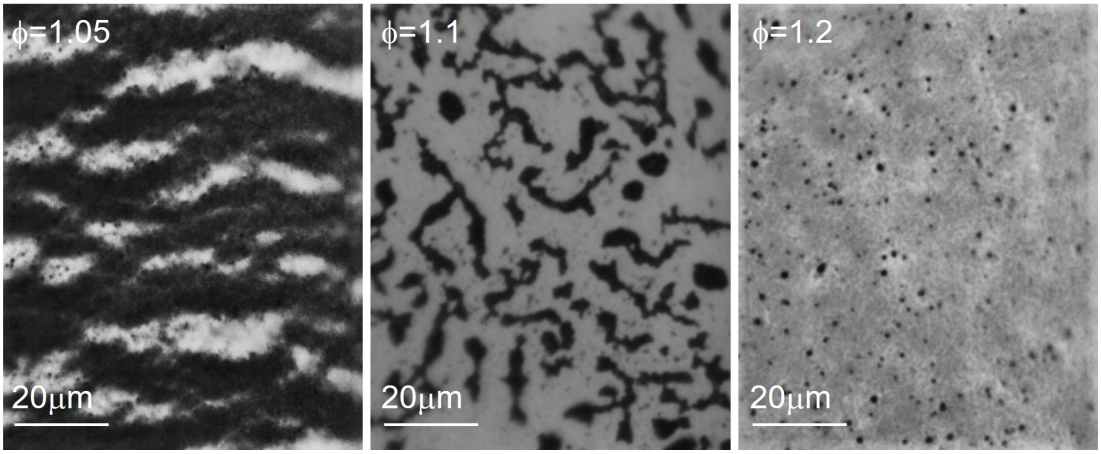

(b) Bright-field microscopy images of the samples for different ϕ at $y_{Fe} = 0.3$ wt.%.

Fig. 6.2 Bright-field microscopy images of the samples collected on the PTFE membrane filters. (a) Images of the samples produced at $\phi = 1.05$ using the feedstock with different mass fractions of ferrocene y_{Fe}. (b) Images of the samples produced at different ϕ from 1.05–1.2 using Feedstock F6 (3.0 wt.% ferrocene and 97.0 wt.% ethanol).

the CNT inception but also affects the yield of all solid products including CNTs and iron oxides.

However caution must be taken when analysing these microscopic images, as water vapour still exists downstream of the sampling flows even after passing through the cold finger device designed to remove them. Therefore the leftover water vapour may condense on the surface of the hydrophobic PTFE filter, washing out a fraction of samples. It may thus cause a change of the sample's morphology and hence misrepresent the yield.

6.3.1.3 SEM analysis

The SEM analyses were performed for the samples with various y_{Fe} produced at $\phi = 1.05$ to examine their morphology on a nano scale. From Fig.6.3, the morphology of the solid products formed at various y_{Fe} share a common feature in the distribution pattern: a web-like structure. Such phenomenon has already been discussed in Chapter 5 where only at temperatures beyond ~1300 °C (corresponding to $\phi = 1.15$) can this structure be seen by SEM. Higher temperatures not only result in an increased yield of CNTs but also promote the entanglement of these carbon products, leading to the formation of the "scaffolding" structure. This upholds the solid aggregates or particles that are likely to be either iron oxides or elemental iron nanoparticles.

By comparing the SEM images in Fig.6.3, the variation of y_{Fe} appears to have little impact on CNT production, and no significant changes of the number density of CNTs in the solid products are clearly observed. Rather, there seems a positive correlation between y_{Fe} and the overall yield of solid products including nanoparticles and CNTs, as these solids are seen more closely packed at higher y_{Fe} according to the SEM images, identical to what has been suggested in Fig.6.2. This may be caused by the increased iron input as y_{Fe} increases, leading to the formation of both nanoparticles and CNTs. Due to the limitations of the SEM system, the physical properties of CNTs produced with varying y_{Fe} cannot be precisely determined. However, the direct measurement made by SEM on the images show that the diameters of CNTs synthesised at all the conditions are of the order of 10 nm, and their lengths can vary from 10 nm up to 1 μm. But no direct evidence is found to suggest a positive correlation between the physical properties of CNTs and y_{Fe} based on the current examination.

6.3.1.4 Summary

The the role of the iron catalyst, ferrocene, in the flame synthesis has been studied. Its mass fraction y_{Fe} in ethanol was varied from 0.1 up to 3.0 wt.% and ϕ was shifted from 1.05 to 1.20

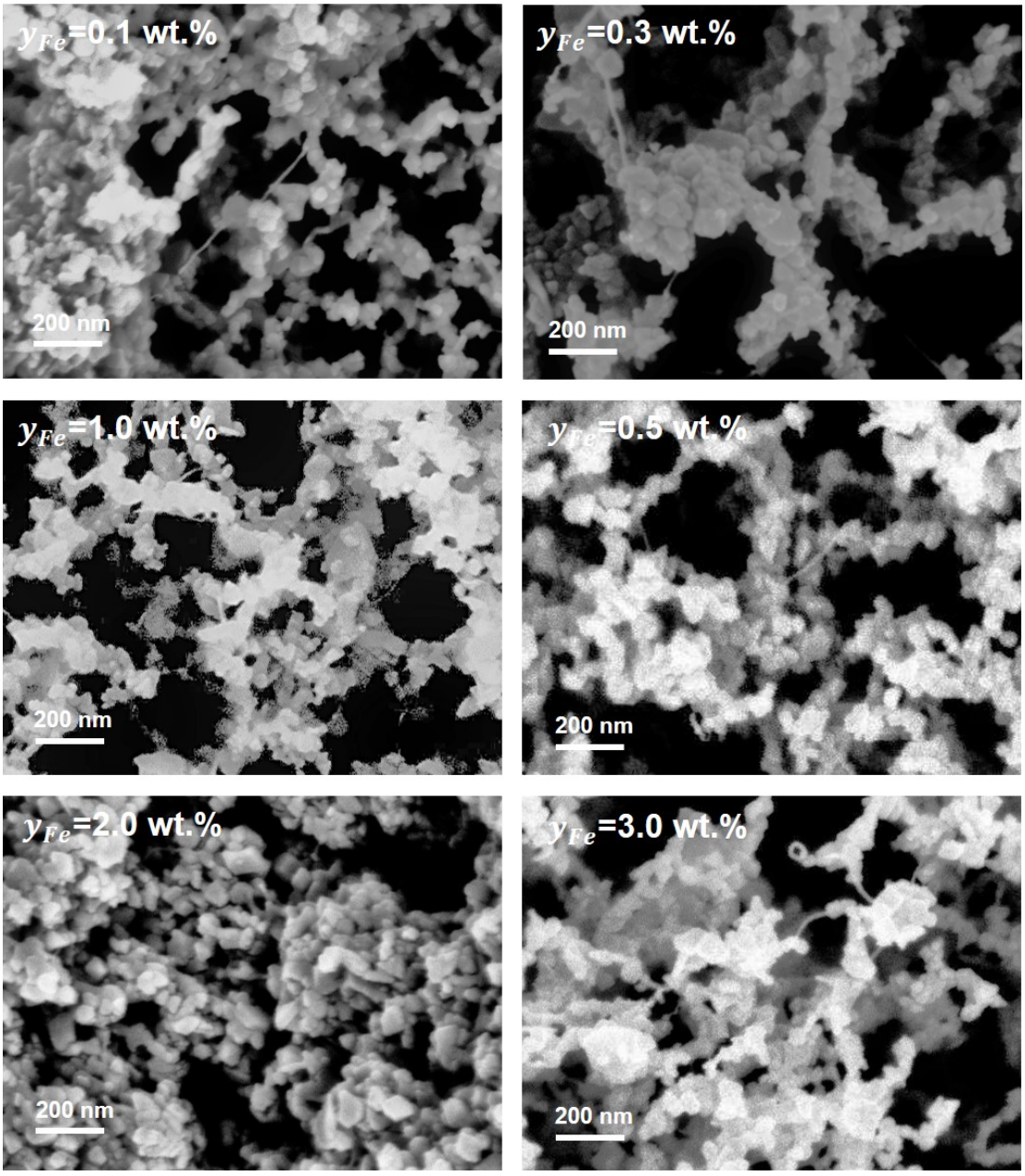

Fig. 6.3 SEM images of the samples collected on PTFE membrane filters. (a) Images of samples produced at ϕ = 1.05 using feedstocks containing different mass fractions of ferrocene y_{Fe}. (b) Images of the samples produced at different ϕ from 1.05 to 1.2 using Feedstock S6 (3.0 wt.% ferrocene and 97.0 wt.% ethanol).

to study the impact of change on the synthesis. The as-produced sample were collected on the PTFE membrane filters and characterised by Raman spectroscopy, bright-field microscopy and SEM. The results show that with the addition of ferrocene, CNTs can be successfully synthesised for different y_{Fe}, but preferably at higher temperatures *i.e.* above 1300 °C as suggested by theoretical estimations. This temperature range is consistent with the results reported by FCCVD studies where 1150–1450 °C is found to be ideal for SWCNT formation [49]. But the varying y_{Fe} from 0.1 to 3.0 wt.% shows no direct effect on improving CNT production since no marked change of the CNT number density in the as-produced materials is observed. Furthermore, little evidence is found regarding the correlation between the variation of y_{Fe} and the CNT physical properties such as length and diameter. However, there appears a positive correlation of the overall yield of solid products with the increase of y_{Fe} due to an increased iron input.

6.3.2 Effect of sulphur catalyst

The addition of sulphur into CNT production has been widely applied particularly in FCCVD synthesis as it has been found to help promote the formation of CNTs, and even aerogels [42, 34, 94, 137, 138]. Rarely, however, has there been much investigation on the sulphur addition as a catalyst in flame synthesis of CNTs. Here, we investigate the role of sulphur in flame synthesis by adding thiophene, the sulphur precursor, to the feedstock to study whether sulphur can help promote the production of CNTs.

6.3.2.1 Raman spectroscopy analysis

Fig.6.4 summarises the Raman spectra normalised over each respective maximum intensity, for samples synthesised in premixed H_2/air flames at ϕ from 1.05 to 1.20 using the feedstock with various sulphur-to-iron mass ratios, $m_{S/Fe}$, from 0 to 10. Based on the observations on Fig.6.4.(a), the effect of sulphur addition is found to be strong at very low levels of sulphur addition. Generally, the Raman spectra of samples produced at various $m_{S/Fe}$ appear alike at $\phi = 1.05$,while those with sulphur share a more similar Raman features compared to that without: a comparable I_G/I_D ratio at around 3.5, an intensified RBM and second order G'-band, and a lowered peak associated with magnetite at 670 cm^{-1}. Also observed in Fig.6.4.(a) is the emergence of the band at ~1920 cm^{-1} on the Raman spectra of samples produced with thiophene ($m_{S/Fe} > 0$). This band, called iTOLA, is recognised as a double-resonance Raman feature of CNTs which is not normally seen in graphite [127]. This mode can shift from 1864 to 2000 cm^{-1} with the increase of laser excitation energy E_{laser} from 1.58 to 2.71 eV [139]. In addition, the normalised intensity of iTOLA band remains fairly

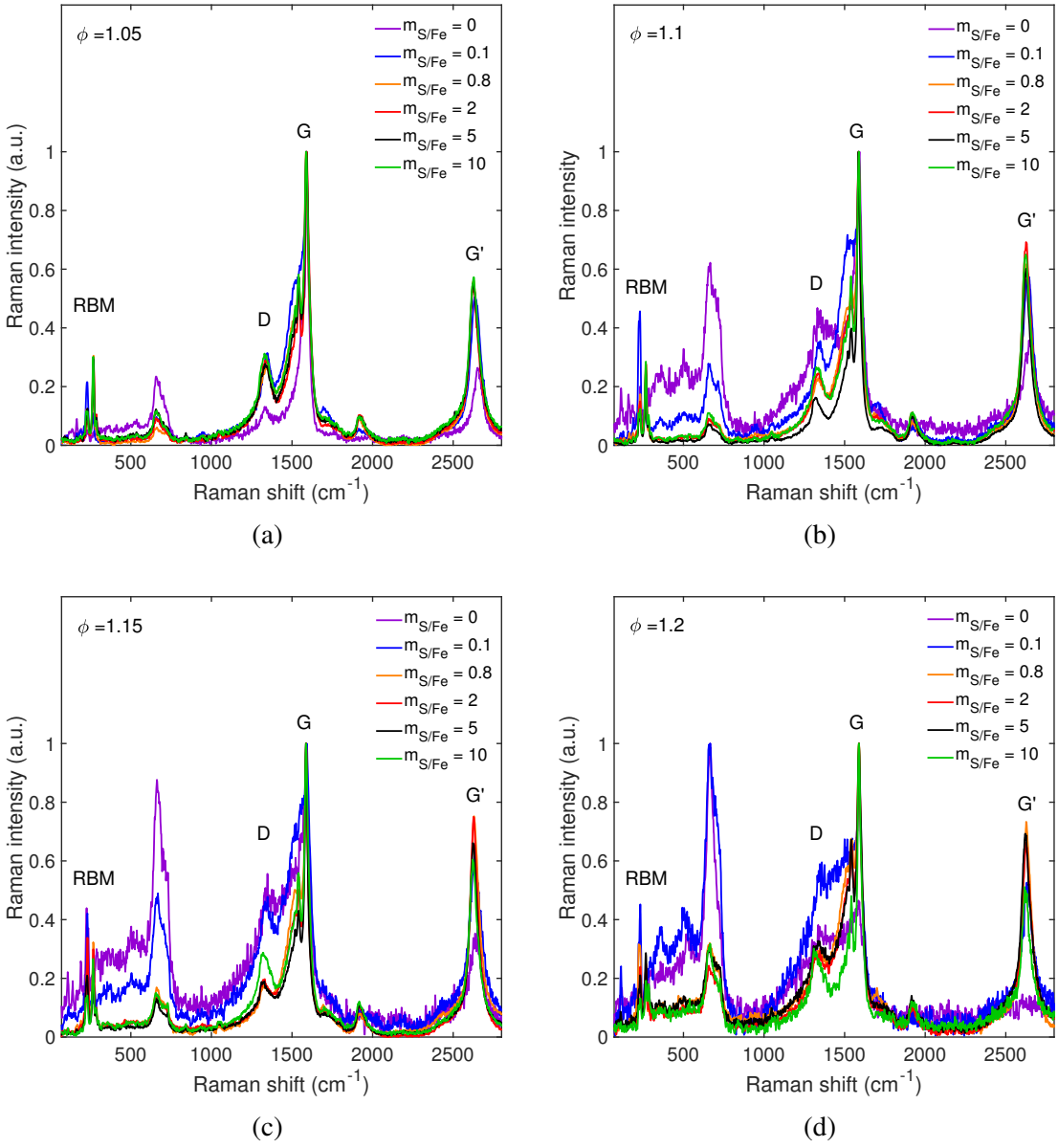

Fig. 6.4 Normalised Raman spectra of the samples produced using feedstocks with varying mass ratios of sulphur to iron $m_{S/Fe}$ at different equivalence ratios ϕ of (a) 1.05, (b) 1.10, (c) 1.15 and (d) 1.20.

unchanged at ~0.1 of the maximum for all samples at $m_{S/Fe} > 0.1$ regardless of the change of ϕ.

The influence of varying $m_{S/Fe}$ on the characteristics of the Raman spectra of the as-produced materials starts to become more pronounced at higher ϕ. As it has already been found that temperatures are key to the CNT synthesis, it is seen from Fig.6.4.(b) that the samples produced without sulphur ($m_{S/Fe} = 0$) are more sensitive to the change in temperatures compared with those with. Specifically, for samples produced without sulphur, its I_G/I_D ratio plunges from 7.7 down to 2.2 (see Table 6.3) as ϕ increases from 1.05 to 1.10. The addition of sulphur appears to help retain the CNT Raman features of the samples as ϕ changes, particularly for those with higher $m_{S/Fe}$. Table 6.3 summarises the I_G/I_D ratios for all the samples collected in the present study, and shows that the I_G/I_D ratio for samples with $m_{S/Fe} = 0.1$ only drops slightly from 3.2 to 2.8 as ϕ increases from 1.05 to 1.10, indicating an enhanced resistance to the drop of temperatures compared with the samples without sulphur (I_G/I_D drops from 7.7 to 2.2). Moreover, beyond $m_{S/Fe} > 0.1$, an increase in I_G/I_D is seen, in particular for $m_{S/Fe} = 5$ where I_G/I_D increases over 70% from 3.6 to 6.2. A further increase in ϕ to 1.15 results in poorer CNT Raman features for both $m_{S/Fe} = 0$ and 0.1. In contrast, only a minor variation in I_G/I_D is seen for the rest of samples where one can see a moderate increase for those with $m_{S/Fe} = 0.8$ and 2 while a small decrease for 5 and 10. For $\phi = 1.20$, CNT features start to disappear for the zero sulphur case whilst they can still be found on samples at $m_{S/Fe} = 0.1$. But for higher sulphur levels, the Raman spectra of the samples resemble those at $\phi = 1.05$ despite of slightly higher signal-to-noise ratios and an increased normalised intensity of the band of magnetite.

The addition of sulphur therefore appears to partly offset the effect of lower synthesis temperatures resulting from higher ϕ. Therefore, sulphur present in the CNT synthesis appears to lower the minimum synthesis temperature required for the inception and growth of CNTs. This may be associated with the production of nanoparticles,resulting a decrease in I_G/I_D as number density ratio of nanoparticles to CNTs increases with temperatures. This suggestion is discussed in the the following SEM analysis.

To further understand the changes of the Raman spectra of CNTs as a result of sulphur addition, a deconvolution of the Raman spectra near the region between the D and G bands, 1200–1800 cm^{-1}, was performed using the Gaussian-Lorentzian fitting function [131], for the cases around $\phi = 1.05$. Due to the high similarity in the Raman spectra among the samples with $m_{S/Fe} > 0.1$, we chose the spectrum of $m_{S/Fe} = 0.8$ as a representation of the samples produced at higher $m_{S/Fe}$. The comparison of the Raman spectra between these samples is illustrated in Fig.6.5.

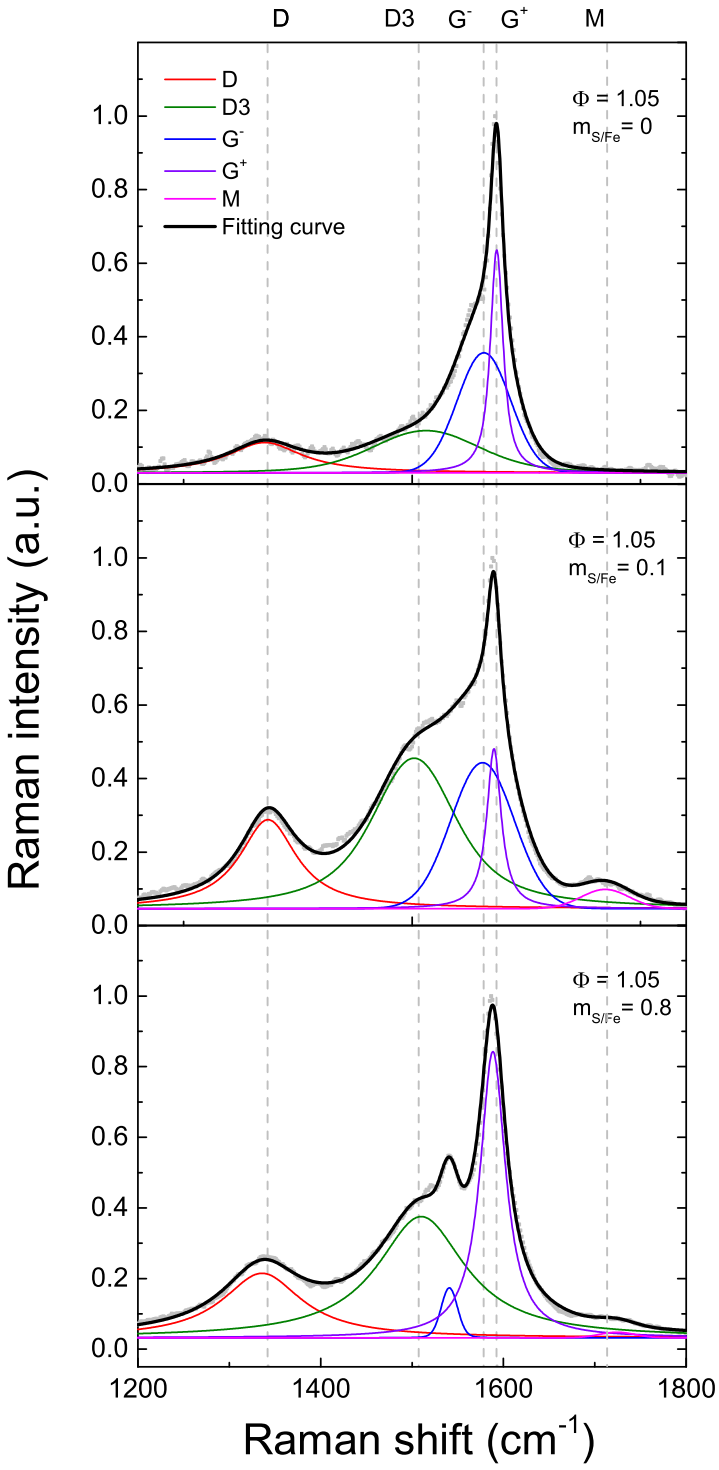

Fig. 6.5 Normalised Raman spectra (shaded dot) and their spectral deconvolution into Lorentzian peaks in the range of wave number between 1200 and 1800 cm^{-1} for the samples produced with different sulphur-to-iron mass ratios $m_{S/Fe}$ from 0 to 0.8 at ϕ = 1.05.

Table 6.3 Normalised Raman intensity ratios of the G-band to D-band I_G/I_D for the samples produced using the feedstock containing various sulphur-to-iron mass ratios $m_{S/Fe}$ at different ϕ from 1.05 to 1.20.

Test No.	$m_{S/Fe}$	I_G/I_D			
		ϕ = 1.05	ϕ = 1.1	ϕ = 1.15	ϕ = 1.2
S0	0	7.7	2.2	2.0	1.2
S1	0.1	3.2	2.8	2.1	1.6
S2	0.8	3.8	4.3	5.6	3.3
S3	2	3.4	4.1	5.1	3.4
S4	5	3.6	6.2	5.3	3.1
S5	10	3.2	3.8	3.5	3.3

Table 6.4 Fitting parameters (obtained by using the Gaussian-Lorentzian function) for the Raman spectra shown in Fig.6.5.

$m_{S/Fe}$	Wavenumber of the fitted peaks (cm^{-1})				
	D	D3	G^-	G^+	M
0	1339	1515	1579	1593	1750
0.1	1342	1502	1577	1590	1711
0.8	1336	1510	1541	1588	1724

According to the figure, the deconvolution of the normalised Raman spectra of the samples with $m_{S/Fe}$ from 0 to 0.8 at $\phi = 1.05$ is shown. These Raman spectra are deconvoluted into 5 Lorentzian peaks, D, D3, G^-, G^+ and M modes, in the wavenumber range of 1200 to 1800 cm^{-1}. The shaded dots represent the original data while the thick black line and the thin lines in various colours represent the fitting curve and the deconvoluted peaks, respectively. The fitting parameters for each sample are summarised in Table 6.4. Clearly observed in Fig.6.5 are the pronounced changes in the Raman spectra with the increase of $m_{S/Fe}$. A broadening effect is seen at the G-band spectrum, particularly at the lower frequencies. This is a result of the increased normalised intensity of D and D3 peaks after the addition of sulphur into the feedstock based on the current Lorentzian peak assumption. Specifically, the relative intensity ratio between D and D3 peaks is hardly affected by the sulphur catalyst, merely rising from 1.3 to 1.6 as $m_{S/Fe}$ changes from 0 to 1. However, their normalised intensities are tripled and doubled at $m_{S/Fe} = 0.1$ and 0.8, respectively, indicating a lowered intensity of the G-band compared with $m_{S/Fe} = 0$. As mentioned in the previous chapter, the D peak, a common feature present in carbon allotropes, is associated with defects in materials while D3 peak is mostly observed in amorphous carbon, *e.g.* soot [131]. Apart from appearance

of the broadening line shape of the G-band, downshifted G^+ and G^- peaks at ~1580 cm^{-1} 1540 cm^{-1}, respectively, are also observed for all the samples with $m_{S/Fe} \geq 0.1$ regardless of the variation of ϕ. This characteristic feature in the G spectrum appears to be consistent with that found in metallic CNTs, under a specific name of Breit-Wigner-Fano lineshape [127, 140]. Therefore, the characteristic Raman features of CNTs are seen to experience pronounced changes as $m_{S/Fe}$ increases up to 0.8, and a transition is clearly observed.

Returning to Fig.6.4, an enhanced RBM can be observed on the Raman spectra with $m_{S/Fe} > 0$. This region is therefore extracted and compared in Fig.6.6. As shown in the figure, there exist two distinct and intense peaks at ~230 cm^{-1} and ~268 cm^{-1}, and a less pronounced peak at ~286 cm^{-1} within the RBM region for all the samples with $m_{S/Fe} > 0$. The rise of the less intense peak at ~286 cm^{-1} is likely to be associated with the formation of FeS or mackinawite. This compound has been reported to have a featured Raman peak at ~283 cm^{-1} [141], and is absent from the Raman spectra at $m_{S/Fe} = 0$. The appearance of the other two distinct peaks are likely to be a result of the radial vibration of carbon atoms in CNTs, and hence are the RBM features. The normalised Raman intensities of these two peaks at different $m_{S/Fe}$ become more differentiated from their counterparts with the increase of ϕ, indicating an impact due to the variation of temperatures. These RBM features usually occur in the frequency range of 120–350 cm^{-1} for SWCNTs of diameters of 0.7–2 nm [127].

The phenomena of an enhanced intensity of the RBM and G'-band, and downshifted and lowered G-band features found on the current investigation have also been observed by experimental and numerical studies in isolated metallic SWCNTs comparing with the semiconducting ones [127, 142, 140]. However, extra care must be taken when analysing these features as the Raman signals in the present study are not directly obtained from an isolated and well-characterised CNT fibres but rather the bundles of CNTs with impurities distributed on the surfaces. Therefore it is difficult to determine if it is the sulphur that changes the properties of CNTs from semiconducting to metallic at this stage, but the features appeared point out the possible implication that adding sulphur into the combustion synthesis might have the aforementioned effect.

6.3.2.2 Morphology analysis by SEM

To further study the role of sulphur in the CNT synthesis, a morphology investigation of the samples produced with various sulphur-to-iron mass ratios, $m_{S/Fe}$, was carried out using scanning electron microscopy. These samples collected on the PTFE filters were examined without any additional treatment, except for a sputter coating on the samples using gold/palladium, a routine step to prevent overcharging the materials.

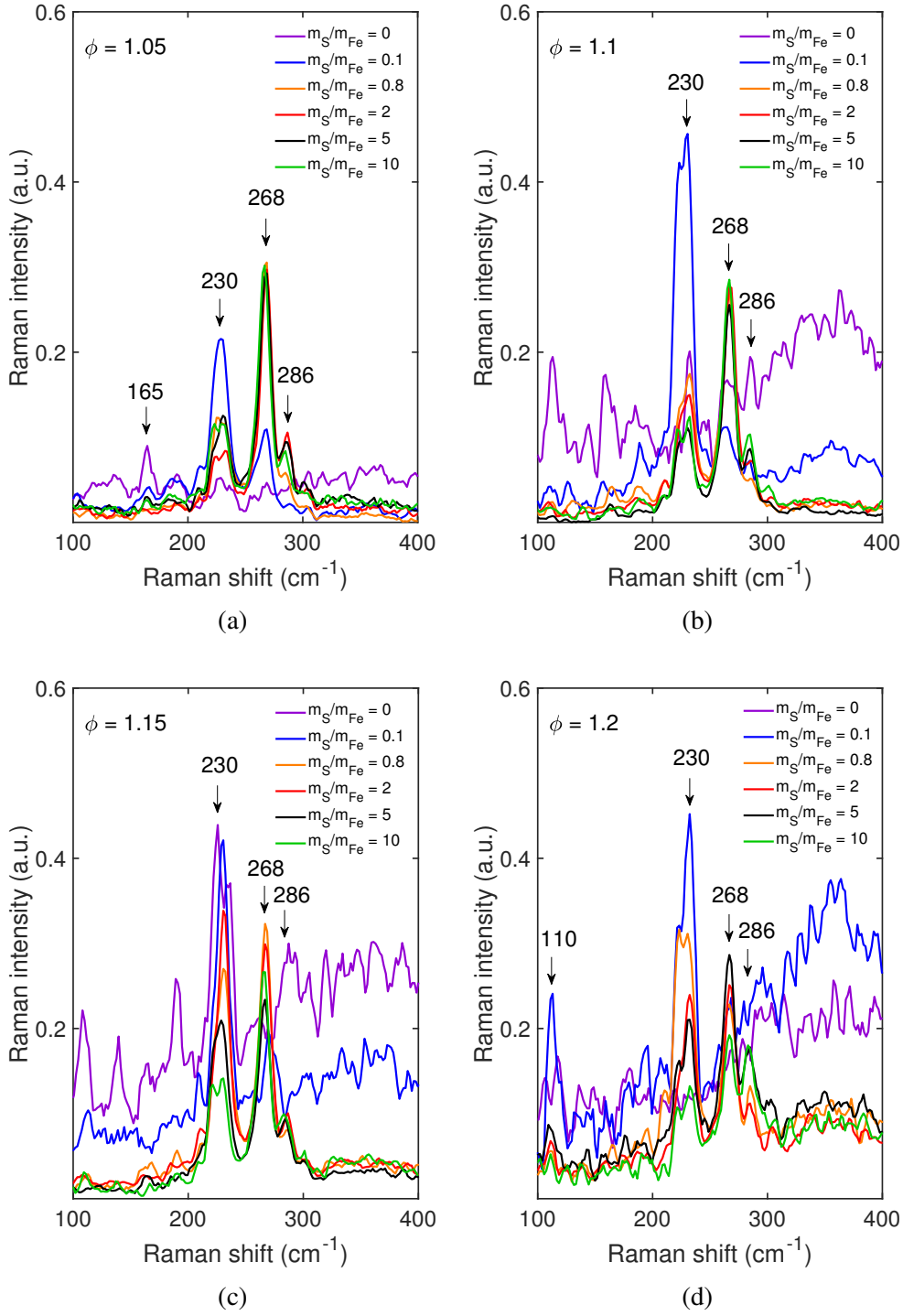

Fig. 6.6 Normalised Raman spectra of the radial breathing mode (RBM) region of the samples produced using feedstocks with various sulphur-to-iron mass ratios $m_{S/Fe}$ at different ϕ of (a) 1.05, (b) 1.10, (c) 1.15 and (d) 1.20.

Fig.6.7 compares the SEM images of samples produced at $\phi = 1.05$ with $m_{S/Fe} = 0$ (no sulphur) and 0.1 corresponding to the feedstock of S0 and S1 in Table 6.2, respectively. Fig.6.7.(a) and (b) shows a marked change in the morphology as a result of sulphur addition, albeit very small mass addition (0.1 wt.% of thiophene in the feedstock). Specifically, isolated CNT fibres and their webs are more clearly seen on the samples in Fig.6.7.(b) than in (a), indicating an increased number density of CNTs as a result of thiophene addition, although nanoparticles still appear as a major solid product. More details of the comparison can been seen on a smaller scale in Fig.6.7.(c) and (d). Apparently shown in these images is that CNTs formed at $m_{S/Fe} = 0.1$ are in a much larger quantity and their lengths also appear longer in comparison with those formed at $m_{S/Fe} = 0$. The diameters of the CNTs can vary but are all of the order of 10 nm, comparable to those at $m_{S/Fe} = 0$. While some CNTs are seen to have larger diameters up to 20 nm in Fig.6.7.(d), but these are expected to be CNT bundles comprising of several entangled CNT fibres. This is evident by the detection of nodes or diversions of these thick tubes into the thinner ones as shown in the inserted images in Fig.6.7.(d). By comparing the inserts in Fig.6.7.(c) and (d), it appears that nanoparticles are preferably packed into clumps instead of forming into radially stretched soot-like agglomerates after adding thiophene. As a consequence, a transition from soot-like agglomerates into a cotton-like morphology, shown in Fig.6.7.(a) and (b), is hence developed due to the presence of sulphur.

The results illustrated above indicate sulphur serves as a promoter for CNT growth during the flame synthesis, which changes the morphology of the samples and thus increases the proportion of CNTs with respective to crystalline nanoparticles (iron oxides and elemental irons). Hence the following questions arise: 1) how does the variation of the mass ratio of sulphur to iron $m_{S/Fe}$ affect the sample's morphology? 2) Is there an optimum composition of the feedstock where CNTs production is maximised relatively to nanoparticles? A further SEM investigation was thus carried out.

Fig.6.8 illustrates the variation of the morphology of samples produced with elevated $m_{S/Fe}$ ratios using the premixed H_2/air flames at $\phi = 1.05$. The morphology of samples changes markedly with the increase of $m_{S/Fe}$, and the most distinct change is an increased density of nanoparticles with $m_{S/Fe}$. For $m_{S/Fe} = 0.8$, CNTs are more clearly observed and have an increased number density based on a visual estimation compared with that at $m_{S/Fe} = 0.1$ (Fig.6.7.(b)). Furthermore, these CNTs possess longer lengths (> 1 μm) and seem to have fewer impurities deposited. A detailed shape of these CNTs is shown in the inserted image in Fig.6.8.(a) where several CNT fibres of diameter of ~5 nm are entangled and shaped into a web-like structure. Similarly to those at $m_{S/Fe} = 0.1$, the nanoparticles at $m_{S/Fe} = 0.8$ also tend to aggregate into clumps rather than being formed as a part of soot-like

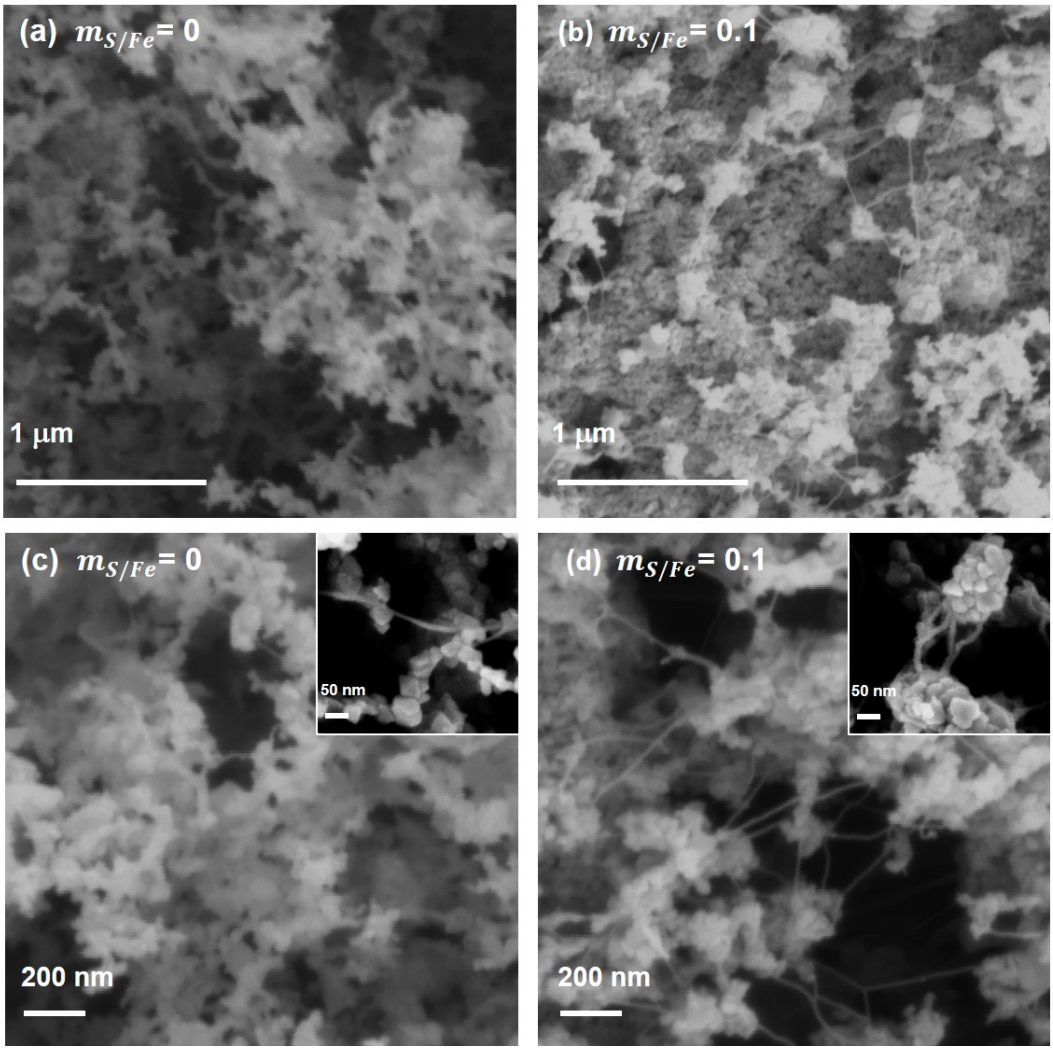

Fig. 6.7 SEM images of the samples produced at $\phi = 1.05$ using the feedstock without sulphur at $m_{S/Fe} = 0$, (a) and (c), and with sulphur at $m_{S/Fe} = 0.1$, (b) and (d).

web structures, which makes it difficult to discern evidence of CNT fibres. When $m_{S/Fe}$ increases to 2, there is an increased number density of nanoparticles instead of CNTs in contrast with the trend as observed below $m_{S/Fe} = 2$. At this condition, CNTs appear to be embedded underneath the nanoparticles as evidenced by the insert, which shows CNTs are surrounded by aggregates of nanoparticles. Beyond $m_{S/Fe} = 2$, a deteriorated morphology can be seen in Fig.6.8.(c) and (d) where CNTs become even harder to detect, despite that the Raman results revealed in Fig.6.4 still provide the evidence of the existence for high I_D/I_G Raman signatures. Given that, it can be inferred that at $\phi = 1.05$ there exist a window of $m_{S/Fe}$ between 0.1 up to 2 where an enhanced proportion of CNTs to nanoparticles can be achieved.

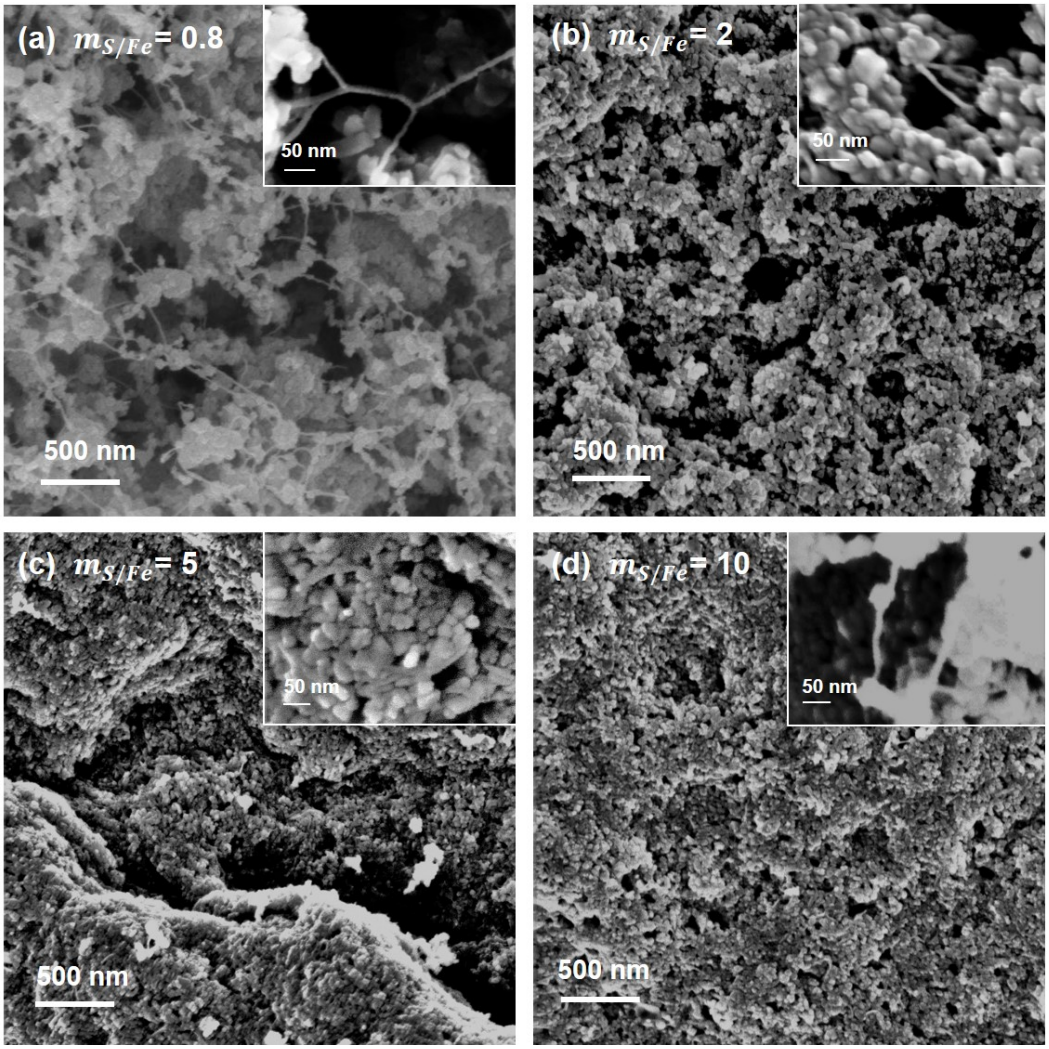

Fig. 6.8 SEM images of the samples produced at $\phi = 1.05$ using the feedstock with various sulphur-to-iron mass ratios $m_{S/Fe}$ from 0.8–10.

According to the results by Raman spectroscopy shown in Fig.6.4 and Table.6.3, the CNT Raman features still remain pronounced as ϕ increases, indicating that, in contrast to the conditions without sulphur, the production of CNTs is less affected by an elevation of equivalence ratios or lower flame temperatures, if sulphur added. This suggests an enlarged formation window of synthesis temperatures due to sulphur addition. Therefore we further examined the samples produced at higher ϕ using SEM to find out the change of morphology with increasing ϕ.

Fig.6.9 summarises the typical morphology of samples produced using feedstocks with different $m_{S/Fe}$ at $\phi = 1.20$, reflecting the changes by sulphur addition to the morphology. In general, beyond $\phi = 1.05$, which corresponds to the highest flame temperature in the

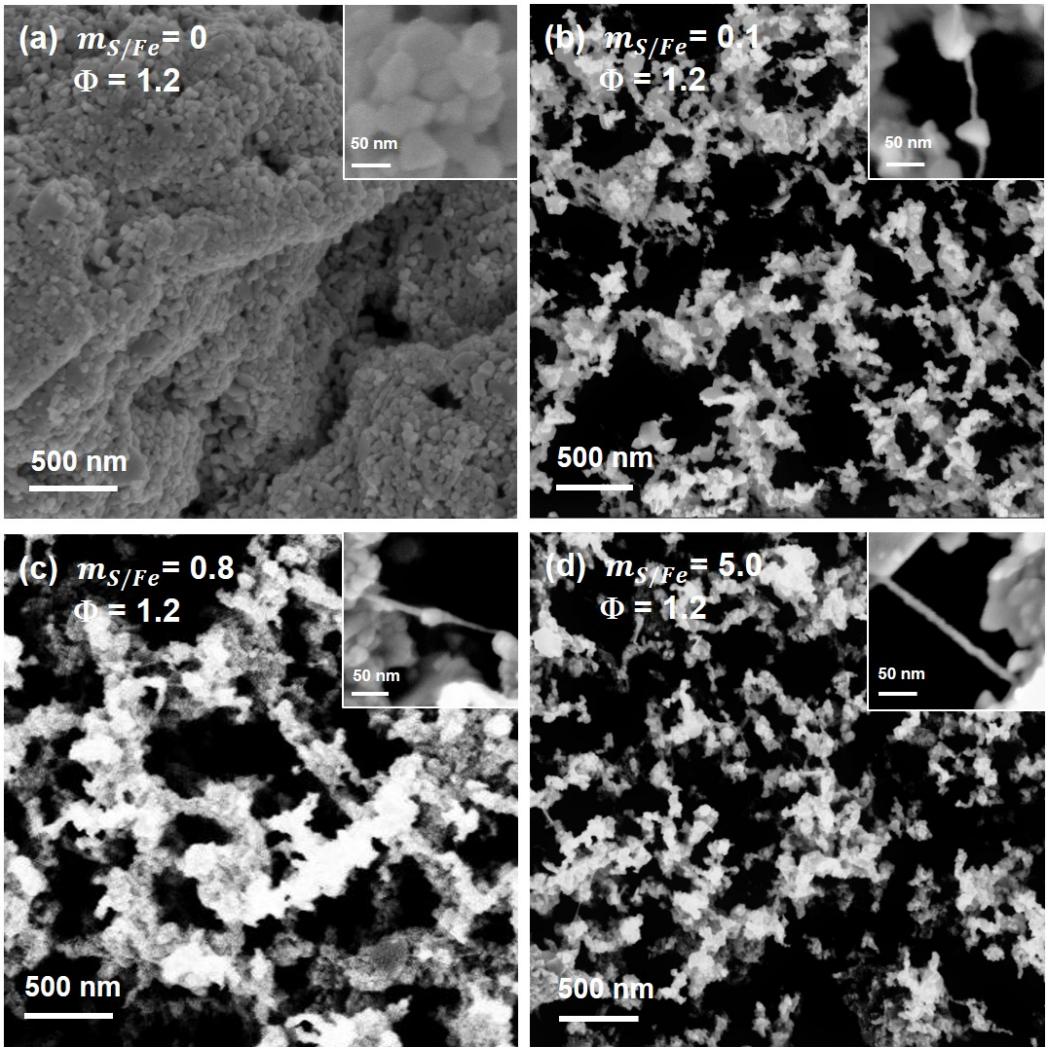

Fig. 6.9 SEM images of the samples produced at $\phi = 1.20$ using the feedstock with various sulphur-to-iron mass ratios $m_{S/Fe}$ from 0–5.0.

current study, there is a marked increase in nanoparticles for the samples with $m_{S/Fe} = 0$; and the web-like structure completely disappears beyond $\phi = 1.15$ as shown in Fig.6.9.(a). Moreover, no CNTs can be found in these samples by SEM, and the CNT Raman features on their spectra completely disappear. In contrast, by adding thiophene into the synthesis, the morphology of the as-produced samples significantly changes. The impact of the variation of $m_{S/Fe}$ on sample's morphology is most distinctly seen at $\phi = 1.05$ shown in Fig.6.8 where an optimum condition for CNT synthesis resides in the range of $m_{S/Fe} = 0.1 - 2.0$. However their morphology becomes closely resembled at ϕ beyond 1.05 according to our SEM examinations, indicating a weakened impact by the variation of $m_{S/Fe}$.

Fig.6.9.(b)-(d) illustrate the distribution pattern of samples produced using feedstocks with different $m_{S/Fe}$ at $\phi > 1.05$. In contrast to that with $m_{S/Fe} = 0$ (see Fig.6.9.(a)), the web-like structure prevail across all $m_{S/Fe}$ from $\phi = 1.1 - 1.2$, and isolated CNTs can still be found without much effort by SEM (highlighted on insets). Therefore, it becomes much clearer why the Raman intensity ratios I_G/I_D of samples with $m_{S/Fe} > 0.1$ (see Table.6.3) reach their maximum values beyond $\phi = 1.05$. As evidenced by Fig.6.8, there is a monotonic increase in number density of nanoparticles with $m_{S/Fe}$ particularly beyond 2, where CNTs are embedded in the lumps of nanoparticles. As a consequence, this morphology results in a lowered I_G/I_D ratio for these products. However, when ϕ increases further, the web-like structures re-emerge for all the samples with $m_{S/Fe} > 0.1$, indicating an increased proportion of CNTs with respective to nanoparticles. This leads to a higher I_G/I_D ratio on their Raman spectra compared with those at $\phi = 1.05$.

Therefore it may be inferred from the current findings that adding sulphur into the combustion synthesis leads to an enlarged temperature window within which CNTs are formed. However, it is must be pointed out that although the premixed flames with lower ϕ become capable of making CNTs if sulphur is added, the length of CNTs is generally shorter than those at $\phi = 1.05$ even though the residence time τ is longer at higher ϕ. Therefore, synthesis temperatures remain as the dominant parameter that not only controls the inception but also the growth of CNTs.

6.3.2.3 Characterisation by TEM

The properties of CNTs produced with varying conditions have been characterised via Raman spectroscopy and SEM in the previous sections, while a more precise determination of the physical properties of CNTs formed in the current synthesis is still needed. Hence we resorted to transmission electron microscopy to get a closer look at the CNTs, including their number of walls and diameters, and nanoparticles.

Given the results revealed from the above investigations, we chose to produce the samples at one of the optimum conditions where $\phi = 1.05$ and the feedstock consisted of $m_{S/Fe} = 1.2$ (ferrocene 2 wt.% and thiophene 1.9 wt.%) for the TEM characterisation. In order to get enough materials for the analysis, the products were collected via the sampling unit for 10 min until the PTFE filter was completely covered by the solids. These materials on the filter were cut into a number of pieces for TEM and SEM examinations.

Prior to TEM, the samples were examined by SEM whose images are shown in Fig.6.10. The morphology of the sample exhibits two dominant patterns: 1) a closed-packed pattern (Fig.6.10.(a)), and 2) a web-like structure (Fig.6.10.(b)). From the LHS image, one can clearly see CNTs hanging in parallel across the "valley" which connects two large bulks of

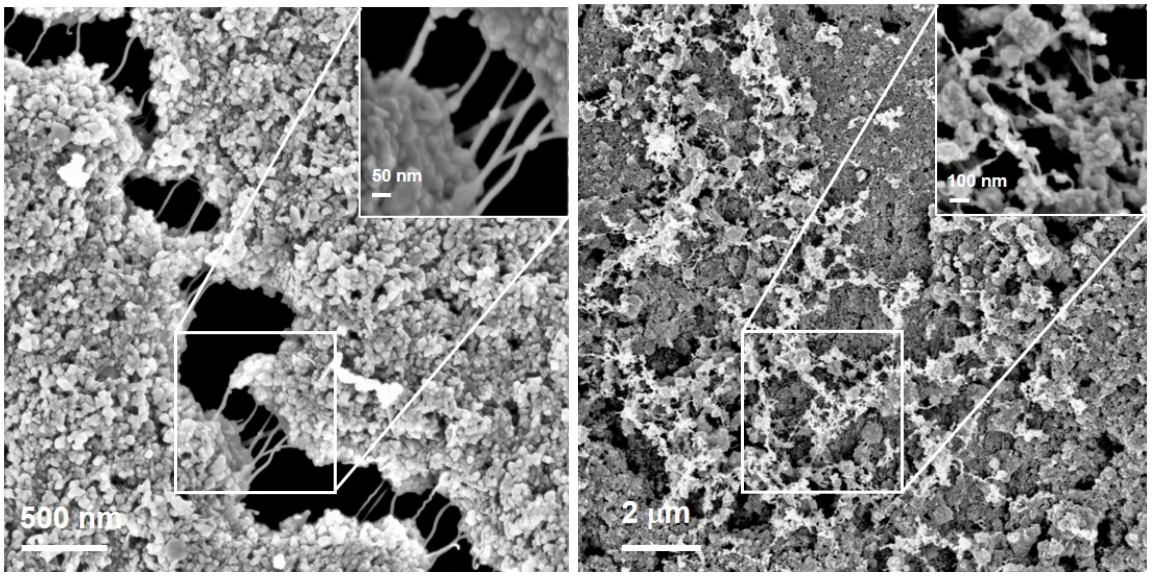

(a) (b)

Fig. 6.10 SEM images of two types of morphologies (a) and (b) of the sample produced at $\phi = 1.05$ using the feedstock with the sulphur-to-iron mass ratio $m_{S/Fe}$ of 1.2 (2.0 wt.% of ferrocene and 1.9 wt.% of thiophene). The whole sampling process lasted for 10 min via the probing unit.

nanoparticles. The inserted image provides a more detailed look of the CNTs. These CNTs with a diameter around 5 nm are generally well stretched, having a visible length over 200 nm but likely much longer. This morphology is of particular interest as it confirms that CNTs do exist inside the clumps of nanoparticles, which is not clearly exhibited in Fig.6.8. In addition, the other distribution pattern seen on the same sample is also of interest. Observed from Fig.6.10.(b) are web-like structures of CNTs with nanoparticles attached, and they are loosely distributed on the surface of the densely packed nanoparticle clumps as seen in the LHS image. It is shown that CNTs of comparable diameters (5 nm) to those shown in Fig.6.10.(a) possess much longer lengths extending up to 2 μm. This suggests that a large quantity of CNTs are actually embedded within the nanoparticle lumps. And the cause for this likely attributes to the long sampling time, as it leads to a collection of a large quantity of both CNTs and nanoparticles which are then densely stacked over time until pores within the web-like structures are fully blocked.

Fig.6.11 presents the TEM images of the samples with $m_{S/Fe} = 1.2$ produced at $\phi = 1.05$. Generally, the existence of CNTs is further confirmed by these images, as one can clearly see hollow cylindrical structures of these tubes. From Fig.6.11.(a), a CNT with a hollow structure can be easily seen, which appears to grow upon a nanoparticle nearby. Based on the direct measurements of the image, the outer and inner diameters of the CNTs are

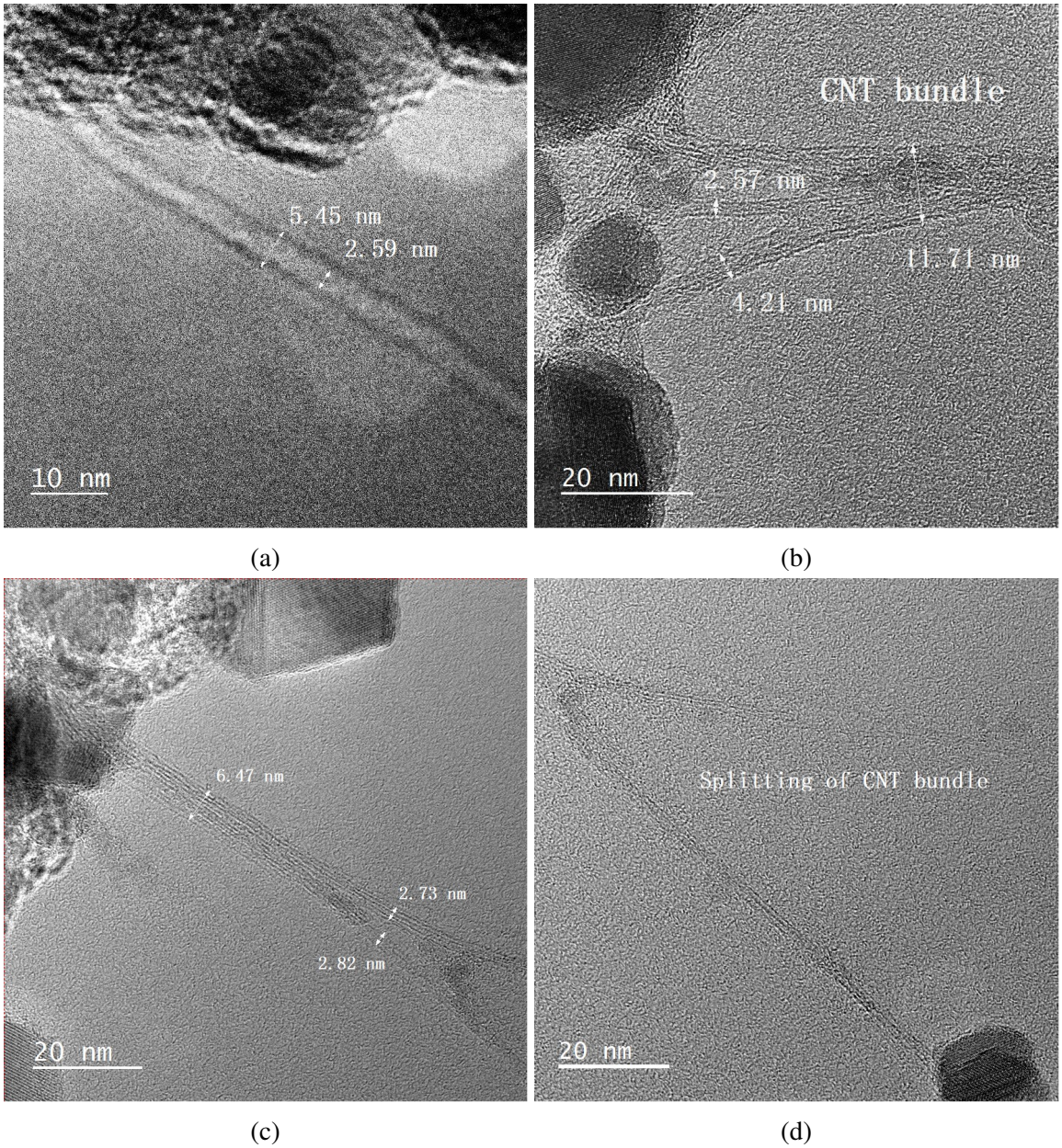

(a) (b)

(c) (d)

Fig. 6.11 TEM images of the samples produced at ϕ = 1.05 using the feedstock with the sulphur-to-iron mass ratio $m_{S/Fe}$ of 1.2 (2.0 wt.% of ferrocene and 1.9 wt.% of thiophene). The whole sampling process lasted 10 min.

determined as 5.45 nm and 2.59 nm, respectively, which yields a wall thickness of ~1.4 nm. However, it is hard to determine the number of walls of this tube, due to the limited resolution of the image. Fig.6.11.(b) shows several CNTs of different diameters joining to form a CNT bundle of an outer diameter of ~12 nm. Similarly to the images shown in Fig.6.11.(a), these individual CNTs are seen originating from nanoparticles on the RHS. Moreover, the inner structures of the CNTs such as wall boundaries can be more easily seen. Although the resolution is still limited, it can be discerned that the CNT of 2.57 nm outer diameter appears to be single-walled, while the other two next to it appear to have several walls. However, it is hard to distinguish whether these two thick tubes are actually individual CNTs or CNT bundles. More information revealed from this image is that these tubes all have a clean centre without impurities trapped in, showing an indication of good quality of the CNTs. Fig.6.11 (c) and (d) depict a splitting CNT bundle which is originated from the nanoparticles on the RHS shown in Fig.6.11(c). This CNT bundle has a smaller outer diameter of 6.5 nm, half of that shown in the previous images. This CNT bundle is seen to split into 2 or 3 individual CNTs or smaller bundles as it grows away from the nanoparticles. The wall boundaries inside bundle are clearly exhibited, and one can confirm that the CNTs of smaller O.D. are composed of a couple of walls. But whether or not these are constructed by SWCNTs is still an open question due to the limited contrast and resolution feasible, although indications associated with SWCNTs have already been shown in the Raman spectroscopy Fig.6.6. Therefore a further analysis by TEM to confirm the existence of SWCNTs is required. In addition, a closer look at the nanoparticles shown in Fig.6.11 (c) and (d) reveals that most of the nanoparticles are highly crystallised, possessing well-ordered arrangements of atoms or molecules. These ordered structured are more likely to belong to iron oxides or elemental iron solids rather than amorphous carbon, whilst some nanoparticles appear to have or partially covered by non-crystallized structures, which might be amorphous carbon. These suggestions however need to be further confirmed by techniques such as X-ray powder diffraction (XRD), which could identify phases of crystalline structures.

Nevertheless, Fig.6.11 confirms the existence of CNTs and CNT bundles. Furthermore, it shows that individual CNTs generally possess very small diameters (< 3 nm) with a couple of layers constructed inside. This figure also shows that the majority of nanoparticles are seen to possess crystalline structures instead of amorphous arrangements. And this implies that most of available carbon might transit into CNTs rather than their amorphous allotropes, which is a good sign for the potential scalability of the current process.

6.4 Conclusion

This chapter presents the results from the investigations of the effects of ferrocene and thiophene on the CNT synthesis using the current flame-based system. The premixed H_2/air flames at different ϕ from 1.05 to 1.2 were used as the heat source for both studies. Various mass fraction of ferrocene y_{Fe} from 0.1 up to 3.0 wt.% dissolved in ethanol solvent were supplied as the feedstock for the ferrocene experiments. Whilst the feedstock containing various proportions of ferrocene and thiophene normalised as mass ratios of sulphur to iron $m_{S/Fe}$ in the range of 0 up to 10 were used for the thiophene investigation. Different characterisation techniques have been used to determined the properties of the as-produced materials including Raman spectroscopy, scanning electron microscopy, and transmission electron microscopy.

CNTs were successfully produced over the whole range of ϕ and y_{Fe} considered. Higher temperatures were found as a dominant parameter rather than y_{Fe} for the CNT synthesis. y_{Fe} was found to have little effect on regulating the proportions of CNTs over nanoparticles but rather to slightly increase the overall yield of both. While more insights were gained from the study of thiophene. The results revealed that sulphur has an effect of moderating the proportion of CNTs over nanoparticles, making CNTs more favoured to form, particularly for the feedstock with $m_{S/Fe}$ of 0.1–2. Furthermore, by adding thiophene into the synthesis, CNTs were found to grow longer and in a much larger quantity compared with those without sulphur exclusively at $\phi = 1.05$ corresponding to a computed flame temperature of ~1450 °C. While when $m_{S/Fe}$ increased beyond 2, a decreased proportion of CNTs was observed, indicating an adverse effect on CNT synthesis. In addition, sulphur was found not only to moderate the proportion of CNTs over nanoparticles and promote the inception and growth of CNTs, but it also lowered the minimum temperature at which CNTs formed. CNTs were successfully formed at $\phi = 1.2$ with $m_{S/Fe} > 0$ where no traces of CNTs were found for cases without thiophene. The results above confirm the addition of sulphur is beneficial for the CNT synthesis, and the optimum range of $m_{S/Fe}$ was identified as 0.1–2.0.

Chapter 7

A Numerical Study on the Premixed Flame Synthesis of CNTs

7.1 Introduction

In Chapter 5 and 6, we have demonstrated the feasibility of producing CNTs using a premixed H_2/air flame. This synthesis method facilitates the understanding of the mechanisms underlying the formation process of CNTs due to its 1-D flame structure, simple post-flame products, and the potential feasibility of doing optical diagnostics. Moreover we have also developed our knowledge of CNT formation using the 0-D thermodynamic equilibrium and the 1-D burner-stabilised flame models. These theoretical calculations are assisted by using the open-source software, Cantera, which has a variety of tools for investigating processes involving chemical kinetics, thermodynamics, and transport [76]. The computational results yielded from these models provide valuable insights about the process and help researchers in the field to better understand the CNT formation, and the complex species distributions. Nevertheless these models still have limitations, particularly for analysing our current combustion process as it involves variations in a higher dimension.

We demonstrate here a 2-D numerical method which links the results from the 0-D and 1-D models to the present study to develop a better understanding of the CNT formation in the combustion system. This 2-D model primarily focuses on the mixing between the centrally injected feedstock (ethanol, catalyst precursors and argon), and the surrounding flows comprising H_2O and N_2 formed from the premixed hydrogen flames. This study aims to investigate the species and temperature distributions of the synthesis in an axisymmetrical domain.

7.2 Methodology

The present model is built for predicting local temperatures and mixing status on the basis of the following assumptions:

1. Incompressible, laminar and axisymmetric flow with variable density at atmospheric pressure;
2. Unity Lewis number $Le = 1$ *i.e.* the thermal diffusivity α equals to the mass diffusivity D_f;
3. Identical diffusivity for all gaseous species;
4. Laminar, steady, and axisymmetric flow;
5. Negligible radiation and conduction losses;
6. Negligible axial diffusion of momentum and species.

Whereas not all of these assumptions are strictly true in the current experiment conditions, the simplified assumptions allow a construction of mixture fraction-temperature maps which assist the understanding of the reacting environment, and serve as a reasonably realistic preliminary model of the system.

Fig.7.1 illustrates the 2-D diffusion model for the flame synthesis. The centrally injected feedstock consists of carbon sources, catalyst precursors, and argon, whereas the surrounding flow is composed of H_2O and N_2 from the hydrogen flames. These two streams are mixed in a confined domain with different proportions depending on the location. To qualitatively study this process, the following governing equations and assumptions are used for the calculations.

7.2.1 Species conservation

The control volume considered herein is based on cylindrical coordinates. The steady state species conservation equation for a 2-D cylindrical element, neglecting axial diffusion can be written as:

$$\rho u_z \frac{\partial Y_i}{\partial z} + \rho u_r \frac{1}{r} \frac{\partial}{\partial r} (r Y_i) = \frac{1}{r} \frac{\partial}{\partial r} \left(r \rho D_f \frac{\partial Y_i}{\partial r} \right) + \dot{w}_i \tag{7.1}$$

where Y_i and Y_e are the mass fractions of the surrounding gases (H_2O and N_2) and the feedstock injected through the central tube, respectively. D_f is the mass diffusivity of species and $\dot{w}_i$ is the rate of production of the species i. For inert or conserved species, $\dot{w}_i = 0$.

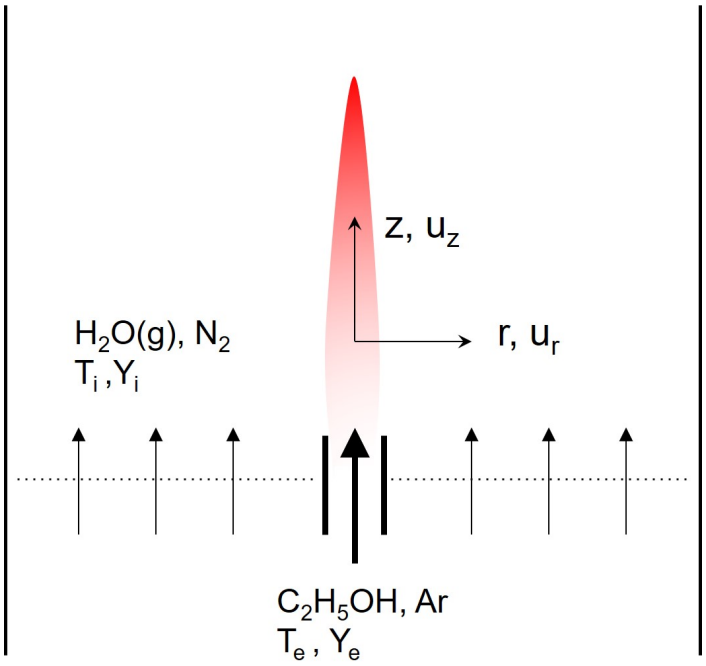

Fig. 7.1 Schematic representation of the 2-D diffusion model for the pyrolysis.

7.2.2 Mixture fraction

We consider a conserved quantity across the reaction zone, such as the total number of atoms or the total energy in an adiabatic exchange. This allows the conservation equations to be expressed without a reaction term, which can be considered later as a function of the state space. We can therefore take the mixture fraction to be defined as the total enthalpy. In a system with constant properties, where the specific heat is constant, the mixture fraction thus be defined as:

$$\xi = \frac{T - T_{i,0}}{T_{e,0} - T_{i,0}}$$

where $T_{e,0}$ and $T_{i,0}$ are the initial temperature of feedstock and the surrounding hot gases. The mixture fraction ξ can also be written as the normalised corresponding to atomic quantities in the mixture, which are conserved across the mixing/reaction region,

$$\xi = \frac{Y_e}{Y_{e,0}}$$

where Y_e and $Y_{e,0}$ are the actual and initial mass fractions of carbon sources, respectively.

7.2.3 Axial momentum conservation

The axial momentum conservation states that the sum of the forces in the axial direction must equal the net momentum flow out of the control volume:

$$\frac{1}{r}\frac{\partial}{\partial z}\left(r\rho u_z u_z\right)+\frac{1}{r}\frac{\partial}{\partial r}\left(r\rho u_z u_r\right)=\frac{1}{r}\frac{\partial}{\partial r}\left(r\mu\frac{\partial u_z}{\partial r}\right)+g\left(\rho_\infty-\rho\right) \tag{7.2}$$

where μ is the dynamic viscosity. The Eq.7.2 is valid throughout the entire 2D axisymmetric flame domain without any discontinuities.

7.2.4 Continuity equation

The overall mass conservation herein considers major mass transport routes: the axial convection and the radial diffusion, which is given as

$$\frac{\partial\rho u_z}{\partial z}+\frac{1}{r}\frac{\partial}{\partial r}\left(r\rho u_r\right)=0 \tag{7.3}$$

It is worth of noting that this is not an independent equation, and it is a result of the sum of all species equations.

7.2.5 Equation of state

To solve above equations, a knowledge of mixture density ρ is needed. According to the state of equation, the density can be derived as

$$\rho=\frac{P\overline{W}}{R_u T} \tag{7.4}$$

where $\overline{W}$ is the mean mixture molecular weight which can be calculated based on the mixtures by

$$\overline{W}=\sum_i^I\left(\frac{Y_i}{W_i}\right)^{-1} \tag{7.5}$$

where Y_i and W_i are the local mass fractions and molecular weights of each species.

The density of the mixture is given by

$$\rho=\frac{p\overline{W}}{R_u T} \tag{7.6}$$

Table 7.1 Specifications of the transport properties of the pyrolysis mixtures

Parameter	Reference value at 300 K	Relation
D_f*	2.5×10^{-5} m^2 s^{-1}	$D_f = 1.87 \times 10^{-10} \frac{T^{2.072}}{P}$ ($T < 450$ K)
		$D_f = 2.75 \times 10^{-9} \frac{T^{1.632}}{P}$ ($T > 450$ K)
μ	1.86×10^{-5} kg m^{-1} s^{-1}**	$\mu = \mu_{ref} \left(\frac{T}{T_{ref}}\right)^{\frac{3}{2}} \frac{T_{ref}+S}{T+S}$, $S = 125$ K

* Using D_f of H_2O in air as the global D_f, see details in Ref.[143].

** Using μ of air as the global μ, see details in Ref.[144].

7.2.6 Boundary conditions

To solve the differential equations, a series of boundary conditions are specified and listed in Table 7.2. For the boundary condition at $z = 0$, the radial region is divided into two parts as shown in Fig.7.1: 1) the central injection region, and 2) the outer surrounding region. The central and the outer regions have radii of $r_c = 3$ mm and $r_w = 35$ mm, respectively. The initial temperature of the central stream $T_{e,0}$ is set at 100 °C which is controlled by the heating unit as described in Chapter 4, while that of the surrounding flow $T_{i,0}$ can vary, which is determined by the mass flux $\dot{m}''$ of the H_2/air mixture, as shown in Fig.5.9. The axial velocities, u_e and u_i, are the initial values for the central and the surrounding flows, respectively.

Table 7.2 Boundary conditions for the diffusion model

Boundary	Mixture fraction ξ	Axial velocity	Radial velocity
$z = 0, 0 \leq r \leq r_c$	1	$u_z = u_e$	
$z = 0, r_c < r < r_w$	0	$u_z = u_i$	
$z = \infty$	0	$u_z = 0$	$u_r = 0$
$r = 0$	$\frac{\partial \xi}{\partial r} = 0$	$\frac{\partial u_z}{\partial r} = 0$	
$r = r_w$	$\xi = 0$	$u_z = 0$	

7.3 Results and discussion

The present numerical results are calculated based on the standard condition at $\phi = 1.05$ used for making CNTs as described in Chapter 5. At this condition, H_2 and air are supplied at 7.0 slpm and 16.7 slpm, respectively. After combustion, the post-flame products formed from this mixture are primarily H_2O and N_2 which have molar fractions of 35% and 65%, respectively, as indicated by the 1-D burner stabilised flame model. The combustion produces a flame temperature T_b of 1450 °C (see Fig.5.9), hence giving rise to an initial axial velocity for the surrounding flow of $u_{i,0} = 0.6$ m/s. The feedstock is injected through the central tube at 0.5 ml/min and carried by an argon stream of 0.1 slpm. This yields an initial axial velocity for the central stream of $u_{e,0} = 0.27$ m/s. Based on these initial assumptions, the present model simulates the whole mixing process, and the results are illustrated in Fig.7.2.

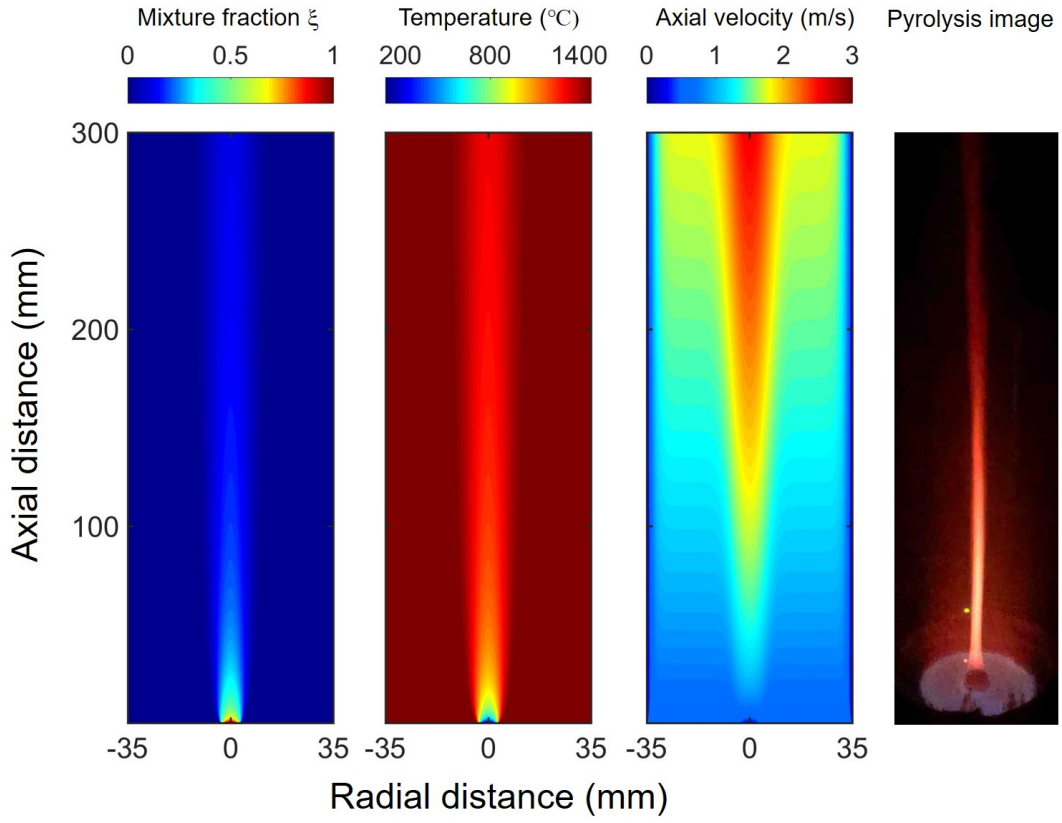

Fig. 7.2 Simulated results for the axisymmetric pyrolysis zone under combustion synthesis. The simulation was carried out based on the standard condition where the outer mixture is burned at at $\phi = 1.05$ (7.0 slpm H_2 and 16.7 slpm air). The feedstock was injected at 0.5 ml/min and carried by an argon stream at 0.1 slpm. Rightmost image shows a photograph of the flame under pyrolysis condition.

According to Fig.7.2, the plots shown from left to right are the spatial distributions of mixture fraction ξ, local temperature T and axial velocity u_z, and the image of the pyrolysis region, respectively. From the plot corresponding to the spatial distribution of ξ, it is seen that the feedstock injected from the central tube diffuses out with increasing axial distance, and ξ soon becomes lower than 0.5 at axial locations beyond 10 mm. This plot provides the spatial distribution of ξ by which the local mass fractions of the feedstock Y_e and the surrounding stream Y_i can be calculated accordingly. The information of Y_e (mass fraction of the feedstock) and Y_i (mass fraction of the surrounding gas) may be used as the input parameters for further analysis by using the 0-D equilibrium model as described in Chapter 2. Next is the the plot which depicts a detailed temperature distribution of the process. The surrounding flow comes out from the premixed H_2/air flame has an initial temperature of 1450 °C much higher than the centrally injected stream which is just heated to 100 °C. While the fast diffusion of species leads to a rapid increase of local temperatures for the cold feedstock. And it is seen that the temperature at $r = 0$ rapidly elevates to 1000 °C at just above 20 mm in the axial direction, quickly approaching the temperature range suitable for making CNTs as recommended by FCCVD studies.

It must be pointed out that the present model does not consider the heat loss to the environment and therefore can only be used for a rough estimation. Refinements shall be made if more accurate results are demanded. The third plot illustrates the spatially-resolved axial velocity of the mixing flows. Since the present model has taken the density change of gaseous species into account, such change due to the rise of temperatures accelerates the flow, leading to an increased axial velocity with the elevation of heights. The flow following the centreline possesses a higher velocity compared with those at a radial position away from the centreline. This is due to the no-slip boundary constraint made for the model, where the u_z at $r = 35$ mm equals to zero. Hence one shall see a decrease in u_z with the increase of r for a given axial distance (> 20 mm). Accordingly, the residence time for the feedstock at the centreline shall be of the order of ~200 ms.

The current model provides critical information of the spatial distributions of input species, temperature and axial velocity, laying the foundation for a deeper understanding of the production of CNTs in the present combustion system. Moreover this computational method serves as a pivotal that connects our numerical models developed in this thesis. We hereby propose a strategy for utilising these modelling methods for studying the synthesis. Fig.7.3 shows the general procedures for a systematic numerical analysis for the CNT production. First, the critical experimental parameters for a successful CNT synthesis serve as the key inputs for the computational study. These include the reactant species, mass fluxes and the burner temperatures. The following 1-D flame simulations based on these input

parameters yield flame temperatures and the distribution of post-flame products, which are then used for the 2-D diffusion modelling. Afterwards, the calculated spatial distribution of mass fractions of species and temperatures are then used as the final inputs for the 0-D analysis by the equilibrium calculations. This produces a spatially-resolved distribution of equilibrium species that ultimately gives a full picture of the entire process.

However, further work is needed to make for improving the current 2-D diffusion model as it still has some limitations. In our current assumptions, chemical reactions are not considered during the mixing of the two streams as there exist some questions need to be answered. First, does H_2O engage in the pyrolysis of ethanol? If so, what the consumption rates are? This must be considered as a source term in Eq.7.1. Second, what is the minimal temperature at which ethanol starts to pyrolyse? Does the thermal decomposition rates fast enough that could be assumed as a reaction sheet model *i.e.* infinitely fast chemical kinetics? This question is rather critical as it allows us to identify the boundary of the chemical reactions by re-defining the current mixture fractions. Hence the present 2-D diffusion model becomes more practically applicable as it resembles a commonly used diffusion flame model.

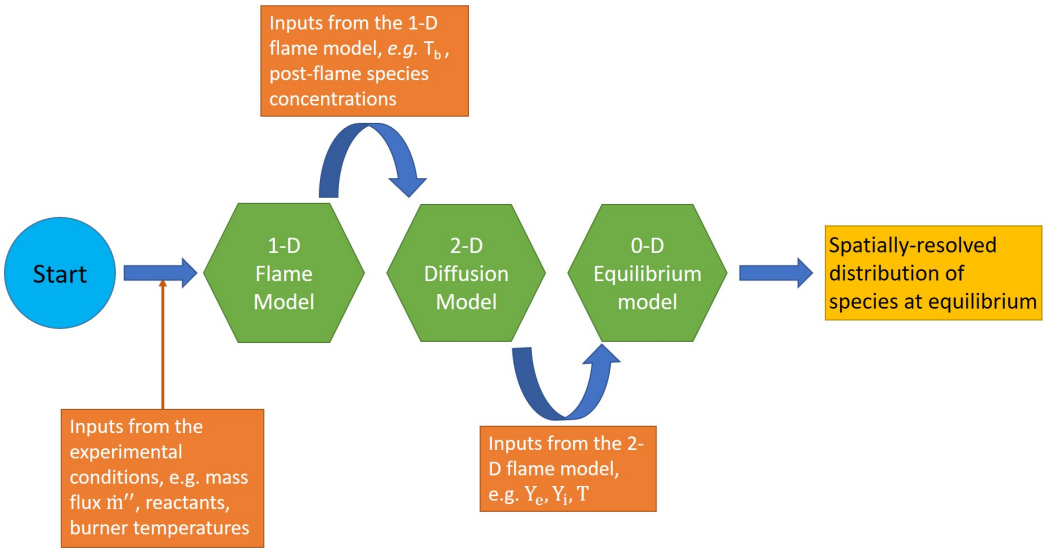

Fig. 7.3 Schematic of the numerical analysis pathway for the CNT synthesis in the combustion system.

7.4 Conclusion

In this chapter, we have proposed a 2-D diffusion model for a computational analysis for the combustion synthesis. This model was built on the basis of non-reacting axisymmetrical laminar jets, which describes pure mixing of two streams: 1) centrally injected feedstock

containing ethanol, catalyst precursors and argon gas, and 2) hot post-flame products, H_2O and N_2, of the surrounding central flows. Spatially-resolved distributions of mixture fraction ξ, local temperature T and axial velocity u_z were obtained for the standard condition at $\phi = 1.05$ for producing CNTs. Ethanol, as the carbon source, has been found diffuse out quickly, with its mass fractions halved just over 10 mm in the axial distance. The cold central stream is heated quickly by the surrounding flows, which reaches 1000 °C from its initial temperature at 100 °C over just 20 mm in the axial direction. The density change of the feedstock as a result of heating by the surrounding flows accelerates its axial velocity, which yields a residence time of the order of 200 ms given for a length of 300 mm. The current model serves as a pivot that connects the 1-D burner stabilised flame model with the 0-D thermodynamic equilibrium method. Further improvements in chemical reaction parts are of urgent need to help refine the current 2-D model so as to estimate the spatial distribution of species with an assistance by the equilibrium model.

Chapter 8

Conclusion and future work

8.1 Conclusion

In the present project, we have carried out a serial of numerical studies and experimental investigations on CNT synthesis, and our understanding of the inception and growth of CNTs has hence been improved. All the experimental conditions of the flame synthesis are listed in Appendix B in Table B.1. We here summarise the primary results in this thesis as follows:

1. A multi-phase thermodynamic equilibrium model is developed for studying the species and phase distributions in a FCCVD system. Thermodynamic properties of CNTs obtained from literature are compared against that of graphite, and only slight deviations are found in the threshold formation temperature of each graphitic carbon allotrope. The atomic partitions of Fe and S elements at equilibrium are however not affected. Iron carbide (Fe_3C) is found to be the primary iron-containing species that exist in both solid and liquid phases within the furnace temperature range (1000–1400 °C), while atomic iron vapour Fe(g) is expected to form at $T > 1250$ °C. H_2S consumes nearly all of the S atoms in the furnace temperature region with a small fraction of S atoms being occupied by SH(g) and CS(g) species. While at lower temperatures ($T < 800$ °C), S atoms are more favoured to form FeS(s) than H_2S(g). An isothermal study of the varying proportions of C, Fe and S elements reveals that Fe_3C, γ-Fe, FeS and C(s) are the four condensed-phase species that may be expected during the synthesis. With oxygen presents in the synthesis, CO is expected to form at the furnace temperatures. The formation of C(s) is significantly affected by the atomic molar ratio O/C. No C(s) is expected if O/C exceeds 1.0, which provides a guideline for selecting carbon sources for CNT synthesis.

2. We developed a premixed flame synthesis apparatus with optical access for *in situ* diagnostics. CNTs were successfully produced using rich H_2/air premixed flames and the feedstock containing ethanol, ferrocene and thiophene. Various characterisation techniques were applied for studying the properties of the as-produced CNTs and nanoparticles. A CNT formation window of $\phi = 1.0$–1.2 was identified. With the assistance of the 1-D burner stabilised flame model, the flame temperature was found critical to a successful CNT synthesis, which was determined by ϕ and the mass flux $\dot{m}''$ of the H_2/air mixtures. The EDX analysis suggested that nanoparticles formed along with CNTs were primarily iron oxides. While the specific chemical forms of these nanoparticles are still unknown, and other methods such as X-ray diffraction (XRD) can be used for a further investigation.

3. A parametric study of the roles of ferrocene and thiophene on CNT synthesis was performed on the premixed flame system. Various proportions of ferrocene from 0.1–3.0 wt.% in feedstock were studied and no significant effects on CNT formation were found. We studied the role of thiophene for the first time in flame synthesis of CNTs, and more insights were gained from this study. By adding thiophene to the feedstock consisting of ethanol and ferrocene, CNTs were found to grow longer and in a much larger quantity than the cases without thiophene. An optimum range was found for the mass ratio of sulphur to iron $m_{S/Fe}$ between 0.1 and 2. The results show that sulphur plays a role in moderating the proportion of CNTs over nanoparticles (the majority is likely to be iron oxides suggested by EDX analysis), and confirm the addition of sulphur is beneficial for CNT synthesis.

4. We developed a 2-D diffusion model for a computational study for the flame synthesis of CNTs. This model was built based on non-reacting axisymmetrical laminar jets. Spatially-resolved distributions of mixture fraction ξ, local mixture temperature T and axial velocity u_z have been calculated for the standard condition at $\phi = 1.05$ for CNT synthesis. This model has been demonstrated as a useful tool for studying the synthesis, and it serves as a pivotal which connects the 0-D thermodynamic equilibrium model with the 1-D burner stabilised flame model. We proposed a strategy/pathway that unifies all the three numerical methods developed in the thesis, and hence a spatial distribution of species in the flame synthesis can be achieved accordingly, although it needs some further refinements for a more accurate estimation.

8.2 Future work

Given the results summarised above, further plans are laid out as follows:

1. **Investigation at variable HAB**. Since the present work only studies the materials collected at a fixed axial distance, or height above burner (HAB), future investigations can be performed by collecting materials at different HAB. By doing this, an inception and growth region along the axis can be identified, which is key for a complete understanding of the synthesis process.

2. **A comprehensive characterisation of CNTs**. During this project, characterisation techniques including Raman spectroscopy, scanning electron microscopy, transmission electron microscopy and energy-dispersive X-ray spectroscopy have been applied for studying the materials. A further investigation by TEM is needed, as it helps researchers to determined number of walls of the as-produced CNTs, although the present evidences indicate the CNTs produced by the flame synthesis shall be single-walled CNTs. Although the atomic ingredients of nanoparticles formed during synthesis have been studied by EDX, their crystalline structures, or chemical formula, are however still unknown. X-ray diffraction technique can be applied to identify these nanoparticles, which helps improve the understanding of the inception and growth mechanisms of CNTs.

3. **Synthesis in H_2/O_2 premixed flames**. In light of the current findings, flame temperatures play a dominant role in CNT synthesis. Hence H_2/O_2 premixed flames with a certain fraction of inert gases can achieve a higher temperature while keeping the overall flow rates minimised. Moreover, a gas phase supply of all precursors including carbon, iron and sulphur, provides a much more flexible control of the synthesis, and hence a broader range of parametric study can be carried out.

   In Fig.8.1, the experimental setup for the CNT synthesis using H_2/O_2 premixed flames is illustrated. A sublimator consists of a stainless steel container and a heating unit controlled by a temperature controller can be used to sublime ferrocene solids. A bubbler in a cold bath can be used for thiophene supply via a stream of carrier gas. These two devices make the gas phase supply of iron and sulphur catalyst precursors become possible. Hence various of gas phase carbon sources such as CH_4, C_2H_2 and C_2H_4, may be used for CNT synthesis. This setup provide a higher degree of flexibility for making nanomaterials, and has the potential of producing CNTs in a larger quantity and of better quality.

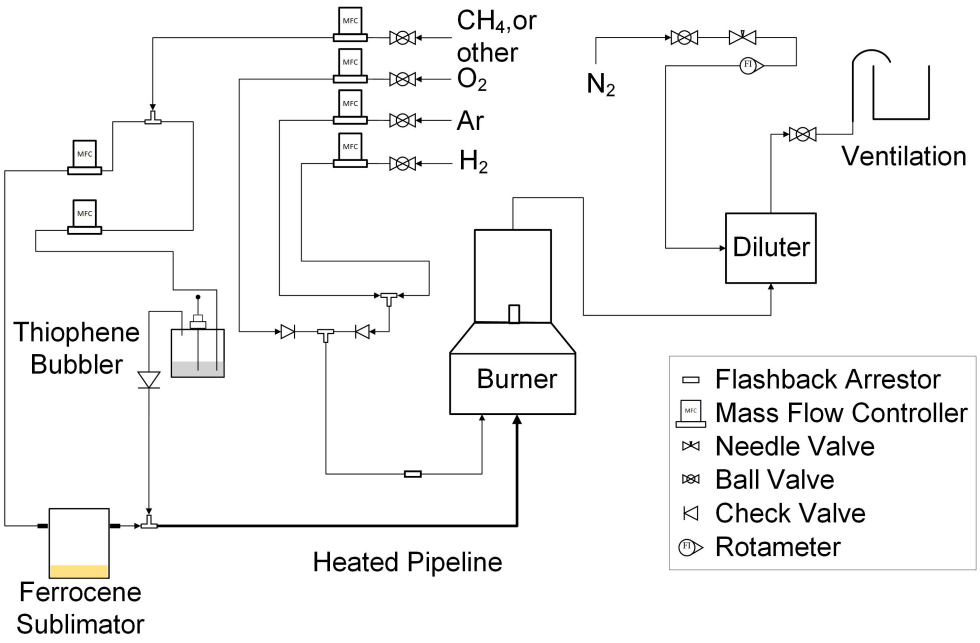

Fig. 8.1 Schematic of the experimental setup for the synthesis of CNTs in H_2/O_2 flames using the gas phase injection equipment.

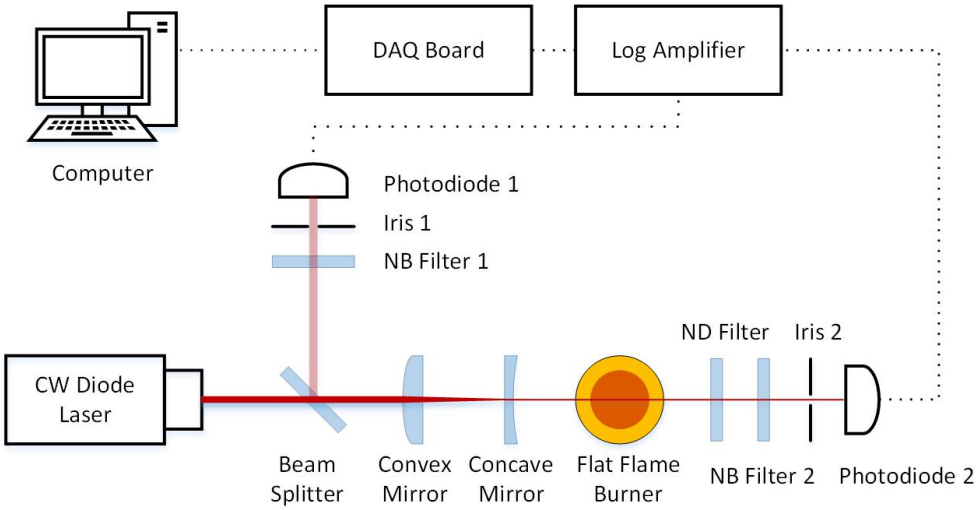

Fig. 8.2 Schematic of the experimental setup of optical diagnostics for flame synthesis using light extinction technique.

4. **Optical diagnostics on CNT synthesis in the flame system .** As described in Chapter 1, a flame synthesis configuration is relatively easy to perform *in situ* optical diagnostics compared to FCCVD methods. Fig.8.2 shows a possible experimental setup for a laser diagnostics for CNT synthesis on the current flame system. Since a quartz tube is placed on top of the premixed flame burner, it provide optical access for laser diagnostics.

Light extinction combined with laser-induced incandescence (LII) techniques have been widely used to determine soot volume fractions and particle size distributions in flames. Theses technique may also be applicable for detecting CNTs in our system, although a more comprehensive review of the existing model must be conducted to develop a modified model to account for CNT signals.

References

[1] S Iijima. Helical microtubules of graphitic carbon. *nature*, 354(07 November):56–58, 1991.

[2] Michael F L De Volder, Sameh H. Tawfick, Ray H. Baughman, and A.John Hart. Carbon Nanotubes : Present and Future Commercial Applications. *Science*, 535(February):535–540, 2013.

[3] R Saito, G Dresselhaus, and M S Dresselhaus. *Physical Properties of Carbon Nanotubes*. Imperial College Press, London, jul 1998.

[4] Erik T Thostenson, Zhifeng Ren, and Tsu-Wei Chou. Advances in the science and technology of carbon nanotubes and their composites: a review. *Composites Science and Technology*, 61(13):1899–1912, oct 2001.

[5] Ray H. Baughman, Zakhidov Anvar A., and Walt A. de Heer. Carbon Nanotubes: The Route Toward Applications. *Science*, 297(5582):787, 2002.

[6] Avetik R. Harutyunyan, Gugang Chen, Tereza M. Paronyan, Elena M. Pigos, Oleg A. Kuznetsov, Kapila Hewaparakrama, Seung Min Kim, Dmitri Zakharov, Eric A. Stach, and Gamini U. Sumanasekera. Preferential Growth of Single-Walled. *Science*, 326(5949):116–120, 2009.

[7] L. Ding, A. Tselev, J. Wang, D. Yuan, H. Chu, T.P. McNicholas, Y. Li, and J. Liu. Selective growth of well-aligned semiconducting single-walled carbon nanotubes. *Nano Letters*, 9(2):800–805, 2009.

[8] Lu-Chang Qin, Xinluo Zhao, Kaori Hirahara, Yoshiyuki Miyamoto, Yoshinori Ando, and Sumio Iijima. The smallest carbon nanotube. *Nature*, 408(6808):50–50, 2000.

[9] Z. K. Tang, L. Zhang, N. Wang, X. X. Zhang, G. H. Wen, G. D. Li, J. N. Wang, C. T. Chan, and P. Sheng. Superconductivity in 4 angstrom single-walled carbon nanotubes. *Science*, 292(5526):2462–2465, 2001.

[10] S. Bandow, F. Kokai, K. Takahashi, M. Yudasaka, L.C. Qin, and S. Iijima. Interlayer spacing anomaly of single-wall carbon nanohorn aggregate. *Chemical Physics Letters*, 321(5-6):514–519, may 2000.

[11] Sumio Iijima. Carbon nanotubes: Past, present, and future. *Physica B: Condensed Matter*, 323(1-4):1–5, 2002.

[12] Raymond M Reilly. Carbon Nanotubes: Potential Benefits and Risks of Nanotechnology in Nuclear Medicine. *Journal of Nuclear Medicine*, 48(7):1039–1042, 2007.

[13] Bei Peng, Mark Locascio, Peter Zapol, Shuyou Li, Steven L. Mielke, George C. Schatz, and Horacio D. Espinosa. Measurements of near-ultimate strength for multiwalled carbon nanotubes and irradiation-induced crosslinking improvements. *Nature Nanotechnology*, 3(10):626–631, 2008.

[14] Shigenobu Ogata and Yoji Shibutani. Ideal tensile strength and band gap of single-walled carbon nanotubes. *Physical Review B - Condensed Matter and Materials Physics*, 68(16):1–4, 2003.

[15] B. Q. Wei, R. Vajtai, and P. M. Ajayan. Reliability and current carrying capacity of carbon nanotubes. *Applied Physics Letters*, 79(8):1172–1174, aug 2001.

[16] R.J. Mora, J.J. Vilatela, and A.H. Windle. Properties of composites of carbon nanotube fibres. *Composites Science and Technology*, 69(10):1558–1563, aug 2009.

[17] Jonghwan Suhr, Nikhil Koratkar, Pawel Keblinski, and Pulickel Ajayan. Viscoelasticity in carbon nanotube composites. *Nature Materials*, 4(2):134–137, 2005.

[18] Alexandre Beigbeder, Philippe Degee, Sheelagh L. Conlan, Robert J. Mutton, Anthony S. Clare, Michala E. Pettitt, Maureen E. Callow, James A. Callow, and Philippe Dubois. Preparation and characterisation of silicone-based coatings filled with carbon nanotubes and natural sepiolite and their application as marine fouling-release coatings. *Biofouling*, 24(4):291–302, jun 2008.

[19] Zhuangchun Wu, Zhihong Chen, Xu Du, Jonathan M Logan, Jennifer Sippel, Maria Nikolou, Katalin Kamaras, John R Reynolds, David B Tanner, Arthur F Hebard, and Andrew G Rinzler. SUPPORTING INFORMATION: Transparent, Conductive Carbon Nanotube Films. *Science*, 305(August):1–3, 2004.

[20] Grzegorz Lota, Krzysztof Fic, and Elzbieta Frackowiak. Carbon nanotubes and their composites in electrochemical applications. *Energy and Environmental Science*, 4(5):1592–1605, 2011.

[21] Elzbieta Frackowiak and François Béguin. Electrochemical storage of energy in carbon nanotubes and nanostructured carbons. *Carbon*, 40(10):1775–1787, aug 2002.

[22] Taketoshi Matsumoto, Toshiki Komatsu, Kazuya Arai, Takahisa Yamazaki, Masashi Kijima, Harukazu Shimizu, Yosuke Takasawa, and Junji Nakamura. Reduction of Pt usage in fuel cell electrocatalysts with carbon nanotube electrodes. *Chemical Communications*, 0(7):840, mar 2004.

[23] Jay P. Gore and Anup Sane. Flame Synthesis of Carbon Nanotubes. In *Carbon Nanotubes - Synthesis, Characterization, Applications*, chapter 7, pages 121–146. InTech, jul 2011.

[24] S Iijima and T Ichihashi. Single-shell carbon nanotubes of 1-nm diameter. *Nature*, 363(17 JUNE):603–605, 1993.

[25] Yoshinori Ando. The Preparation of Carbon Nanotubes. *Fullerene Science and Technology*, 2(2):173–180, may 1994.

[26] Yoshinori Ando, Xinluo Zhao, and Masato Ohkohchi. Sponge of Purified Carbon Nanotubes. *Japanese Journal of Applied Physics*, 37(Part 2, No. 1A/B):L61–L63, jan 1998.

[27] Yoshinori Ando, Xinluo Zhao, Toshiki Sugai, and Mukul Kumar. Growing carbon nanotubes. *Materials Today*, 7(10):22–29, 2004.

[28] Ting Guo, M D Diener, Yan Chai, M J Alford, R E Haufler, S M McClure, T Ohno, J H Weaver, G E Scuseria, and R E Smalley. Uranium stabilization of C28: A tetravalent fullerene. *Science*, 257(5077):1661–1664, sep 1992.

[29] Andreas Thess, Roland Lee, Pavel Nikolaev, Hongjie Dai, Pierre Petit, Jerome Robert, Chunhui Xu, Young Hee Lee, Seong Gon Kim, Andrew G. Rinzler, Daniel T. Colbert, Gustavo E. Scuseria, David Tománek, John E. Fischer, and Richard E. Smalley. Crystalline ropes of metallic carbon nanotubes. *Science*, 273(5274):483–487, jul 1996.

[30] Wilson Merchan-Merchan, Alexei V. Saveliev, Lawrence Kennedy, and Walmy Cuello Jimenez. Combustion synthesis of carbon nanotubes and related nanostructures. *Progress in Energy and Combustion Science*, 36(6):696–727, dec 2010.

[31] Shunji Bandow, S. Asaka, Y. Saito, A. M. Rao, L. Grigorian, E. Richter, and P. C. Eklund. Effect of the Growth Temperature on the Diameter Distribution and Chirality of Single-Wall Carbon Nanotubes. *Physical Review Letters*, 80(17):3779–3782, apr 1998.

[32] Rahul Sen, Y Ohtsuka, T Ishigaki, D Kasuya, S Suzuki, H Kataura, and Y Achiba. Time period for the growth of single-wall carbon nanotubes in the laser ablation process: evidence from gas dynamic studies and time resolved imaging. *Chemical Physics Letters*, 332(5-6):467–473, dec 2000.

[33] H. Kataura, Y. Kumazawa, Y. Maniwa, Y. Ohtsuka, R. Sen, S. Suzuki, and Y. Achiba. Diameter control of single-walled carbon nanotubes. *Carbon*, 38(11):1691–1697, 2000.

[34] Ya-Li Li, Ian a Kinloch, and Alan H Windle. Direct spinning of carbon nanotube fibers from chemical vapor deposition synthesis. *Science (New York, N.Y.)*, 304(5668):276–8, apr 2004.

[35] P. L. Walker, J. F. Rakszawski, and G. R. Imperial. Carbon formation from carbon monoxide-hydrogen mixtures over iron catalysts. I. Properties of carbon formed. *Journal of Physical Chemistry*, 63(2):133–140, 1959.

[36] J.-F Colomer, C Stephan, S Lefrant, G Van Tendeloo, I Willems, Z Kónya, A Fonseca, Ch Laurent, and J.B Nagy. Large-scale synthesis of single-wall carbon nanotubes by catalytic chemical vapor deposition (CCVD) method. *Chemical Physics Letters*, 317(1-2):83–89, jan 2000.

[37] Firoozeh Danafar, A. Fakhru'l-Razi, Mohd Amran Mohd Salleh, and Dayang Radiah Awang Biak. Fluidized bed catalytic chemical vapor deposition synthesis of carbon nanotubes-A review. *Chemical Engineering Journal*, 155(1-2):37–48, 2009.

[38] K. B.K. Teo, S. B. Lee, M Chhowalla, V Semet, Vu Thien Binh, O Groening, M Castignolles, A Loiseau, G Pirio, P Legagneux, D Pribat, D G Hasko, H Ahmed, G. A.J. Amaratunga, and W I Milne. Plasma enhanced chemical vapour deposition carbon nanotubes/nanofibres - How uniform do they grow? *Nanotechnology*, 14(2):204–211, feb 2003.

[39] Chee Howe See and Andrew T. Harris. A review of carbon nanotube synthesis via fluidized-bed chemical vapor deposition. *Industrial and Engineering Chemistry Research*, 46(4):997–1012, 2007.

[40] Morinobu Endo, Takuya Hayashi, and Yoong-Ahm Kim. Large-scale production of carbon nanotubes and their applications. *Pure and Applied Chemistry*, 78(9):1703–1713, 2006.

[41] Christian Hoecker, Fiona Smail, Mark Bajada, Martin Pick, and Adam Boies. Catalyst nanoparticle growth dynamics and their influence on product morphology in a CVD process for continuous carbon nanotube synthesis. *Carbon*, 96:116–124, 2016.

[42] Ya-Li Li, Liang-Hong Zhang, Xiao-Hua Zhong, and Alan H Windle. Synthesis of high purity single-walled carbon nanotubes from ethanol by catalytic gas flow CVD reactions. *Nanotechnology*, 18(22):225604, jun 2007.

[43] Celia Castro, Mathieu Pinault, Dominique Porterat, Cécile Reynaud, and Martine Mayne-L'Hermite. The role of hydrogen in the aerosol-assisted chemical vapor deposition process in producing thin and densely packed vertically aligned carbon nanotubes. *Carbon*, 61:585–594, sep 2013.

[44] Anna Moisala, Albert G. Nasibulin, David P. Brown, Hua Jiang, Leonid Khriachtchev, and Esko I. Kauppinen. Single-walled carbon nanotube synthesis using ferrocene and iron pentacarbonyl in a laminar flow reactor. *Chemical Engineering Science*, 61(13):4393–4402, jul 2006.

[45] M. Motta, Y. L. Li, I. a. Kinloch, and a. H. Windle. Spun fibers of carbon nanotubes. *Nano Letters*, 5(8):1529–1533, 2005.

[46] J. N. Wang, X. G. Luo, T. Wu, and Y. Chen. High-strength carbon nanotube fibre-like ribbon with high ductility and high electrical conductivity. *Nature Communications*, 5:1–8, 2014.

[47] Wei Xu, Yun Chen, Hang Zhan, and Jian Nong Wang. High-Strength Carbon Nanotube Film from Improving Alignment and Densification. *Nano Letters*, 16(2):946–952, 2016.

[48] Tong Wu and Jian Nong Wang. Carbon nanotube springs with high tensile strength and energy density. *RSC Advances*, 6(44):38187–38191, 2016.

[49] M. S. Motta, A. Moisala, I. A. Kinloch, and A. H. Windle. The Role of Sulphur in the Synthesis of Carbon Nanotubes by Chemical Vapour Deposition at High Temperatures. *Journal of Nanoscience and Nanotechnology*, 8(5):2442–2449, 2008.

[50] Devin Conroy, Anna Moisala, Silvana Cardoso, Alan Windle, and John Davidson. Carbon nanotube reactor: Ferrocene decomposition, iron particle growth, nanotube aggregation and scale-up. *Chemical Engineering Science*, 65(10):2965–2977, may 2010.

[51] Hongjie Dai. Carbon nanotubes : opportunities and challenges. *Surface Science*, 500:218–241, 2002.

[52] T. S. Gspann, F. R. Smail, and a. H. Windle. Spinning of carbon nanotube fibres using the floating catalyst high temperature route: purity issues and the critical role of sulphur. *Faraday Discussions*, 173:47–65, 2014.

[53] Wey Yang Teoh, Rose Amal, and Lutz Mädler. Flame spray pyrolysis: An enabling technology for nanoparticles design and fabrication. *Nanoscale*, 2(8):1324–1347, 2010.

[54] JB Howard, KD Chowdhury, and JBV Sande. Carbon shells in flames. *Nature*, 1994.

[55] Shuiqing Li, Yihua Ren, Pratim Biswas, and Stephen D. Tse. Flame aerosol synthesis of nanostructured materials and functional devices: Processing, modeling, and diagnostics. *Progress in Energy and Combustion Science*, 55:1–59, 2016.

[56] Randall L. Vander Wal, Lee J. Hall, and Gordon M. Berger. Optimization of Flame Synthesis for Carbon Nanotubes Using Supported Catalyst. *The Journal of Physical Chemistry B*, 106(51):13122–13132, dec 2002.

[57] Liming Yuan, Kozo Saito, Chunxu Pan, FA Williams, and AS Gordon. Nanotubes from methane flames. *Chemical Physics Letters*, 340(June):237–241, 2001.

[58] W Merchan-Merchan and Alexei Saveliev. Formation of carbon nanotubes in counterflow, oxy-methane diffusion flames without catalysts. *Chemical Physics Letters*, 354(March):20–24, 2002.

[59] Michael D. Diener, Noah Nichelson, and John M. Alford. Synthesis of Single-Walled Carbon Nanotubes in Flames. *The Journal of Physical Chemistry B*, 104(41):9615–9620, oct 2000.

[60] Randall L. Vander Wal, Lee J. Hall, and Gordon M. Berger. The chemistry of premixed flame synthesis of carbon nanotubes using supported catalysts. *Proceedings of the Combustion Institute*, 29(1):1079–1085, jan 2002.

[61] RL Vander Wal and LJ Hall. Flame synthesis of Fe catalyzed single-walled carbon nanotubes and Ni catalyzed nanofibers: growth mechanisms and consequences. *Chemical Physics Letters*, 349(November):178–184, 2001.

[62] RL Vander Wal. Flame synthesis of Ni-catalyzed nanofibers. *Carbon*, 40:2101–2107, 2002.

[63] Murray J. Height, Jack B. Howard, Jefferson W. Tester, and John B. Vander Sande. Flame synthesis of single-walled carbon nanotubes. *Carbon*, 42(11):2295–2307, jan 2004.

[64] Randall L Vander Wal, Thomas M Ticich, and Valerie E Curtis. Diffusion flame synthesis of single-walled carbon nanotubes. *Chemical Physics Letters*, 323(June):217–223, 2000.

[65] Ying Li, XinMing Qiu, Yajun Yin, Fan Yang, and Qinshan Fan. The specific heat of carbon nanotube networks and their potential applications. *Journal of Physics D: Applied Physics*, 42(15):155405, 2009.

[66] C.J. Unrau, R.L. Axelbaum, P. Biswas, and P. Fraundorf. Synthesis of single-walled carbon nanotubes in oxy-fuel inverse diffusion flames with online diagnostics. *Proceedings of the Combustion Institute*, 31(2):1865–1872, jan 2007.

[67] M. R. Zachariah, D. Chin, H. G. Semerjian, and J. L. Katz. Silica particle synthesis in a counterflow diffusion flame reactor. *Combustion and Flame*, 78(3-4):287–298, dec 1989.

[68] M. D. Rumminger, D. Reinelt, V. Babushok, and G. T. Linteris. Numerical study of the inhibition of premixed and diffusion flames by iron pentacarbonyl. *Combustion and Flame*, 116(1-2):207–219, 1999.

[69] Alexei V. Saveliev, Wilson Merchan-Merchan, and Lawrence A. Kennedy. Metal catalyzed synthesis of carbon nanostructures in an opposed flow methane oxygen flame. *Combustion and Flame*, 135(1-2):27–33, oct 2003.

[70] Shuhn Shyurng Hou, De Hua Chung, and Ta Hui Lin. High-yield synthesis of carbon nano-onions in counterflow diffusion flames. *Carbon*, 47(4):938–947, apr 2009.

[71] Garima Mittal, Vivek Dhand, Kyong Yop Rhee, Hyeon-Ju Kim, and Dong Ho Jung. Carbon nanotubes synthesis using diffusion and premixed flame methods: a review. *Carbon Letters*, 16(1):1–10, 2015.

[72] Prarthana Gopinath and Jay Gore. Chemical kinetic considerations for postflame synthesis of carbon nanotubes in premixed flames using a support catalyst. *Combustion and Flame*, 151(3):542–550, nov 2007.

[73] Randall L Vander Wal and Lee J Hall. Ferrocene as a precursor reagent for metal-catalyzed carbon nanotubes: competing effects. *Combustion and Flame*, 130(1-2):27–36, jul 2002.

[74] Randall L Vander Wal. Fe-catalyzed single-walled carbon nanotube synthesis within a flame environment. *Combustion and Flame*, 130(1-2):37–47, jul 2002.

[75] John Z. Wen, Henning Richter, William H. Green, Jack B. Howard, Meri Treska, Paula M. Jardim, and John B. Vander Sande. Experimental study of catalyst nanoparticle and single walled carbon nanotube formation in a controlled premixed combustion. *Journal of Materials Chemistry*, 18(13):1561, 2008.

[76] David G Goodwin, Harry K Moffat, and Raymond L Speth. Cantera: An Object-Oriented Software Toolkit For Chemical Kinetics, Thermodynamics, And Transport Processes. Version 2.3.0, jan 2017.

[77] Won Yong Lee, Jeff Hanna, and Ahmed F Ghoniem. On the Predictions of Carbon Deposition on the Nickel Anode of a {SOFC} and Its Impact on Open-Circuit Conditions. *Journal of The Electrochemical Society*, 160(2):F94–F105, 2013.

[78] K. Sasaki and Y. Teraoka. Equilibria in Fuel Cell Gases I. Equilibrium Compositions and Reforming Conditions. *Journal of The Electrochemical Society*, 150(7):A885, 2003.

[79] K. Sasaki and Y. Teraoka. Equilibria in Fuel Cell Gases II. The C-H-O Ternary Diagrams. *Journal of The Electrochemical Society*, 150(7):A885, 2003.

[80] Zdzisław Jaworski, Barbara Zakrzewska, and Paulina Pianko-Oprych. On thermodynamic equilibrium of carbon deposition from gaseous C-H-O mixtures: Updating for nanotubes. *Reviews in Chemical Engineering*, 33(3):217–235, 2017.

[81] Christophe Guéret, Michel Daroux, and Francis Billaud. Methane pyrolysis: Thermodynamics. *Chemical Engineering Science*, 52(5):815–827, 1997.

[82] Bonnie Mcbride, Sanford Gordon, and Martin Reno. Coefficients for Calculating Thermodynamic and Transport Properties of Individual Species. *Nasa Technical Memorandum*, 4513(NASA-TM-4513):98, 1993.

[83] William R. (William Robert) Smith and Ronald W. (Ronald William) Missen. *Chemical reaction equilibrium analysis : theory and algorithms*. John Wiley & Sons, New York, 1982.

[84] William R. Smith and R.W. Missen. Strategies for Solving The Chemical Equilibrium Problem and an Efficient Microcomputer-Based Algorithm. *The Canadian Journal of Chemical Engineering*, 66(August):591–598, 1988.

[85] Arnold Wexler. Vapor pressure formulation for water in range 0 to 100 Degrees C. A revision. *Journal of Research of the National Bureau of Standards-A. Physics and Chemistry*, 80A:775–785, 1976.

[86] P. D. Desai. Thermodynamic Properties of Iron and Silicon. *Journal of Physical and Chemical Reference Data*, 15(3):967–983, jul 1986.

[87] Alexander Burcat and Branko Ruscic. Third Millennium Ideal Gas and Condensed Phase Thermochemical Database for Combustion with Updates from Active Thermochemical Tables, 2005.

[88] O Kubaschewski, A L Evans, and C B Alcock. *Metallurgical thermochemistry*. Pergamon, Oxford, 4th edition, 1967.

[89] John Chipman. Thermodynamics and phase diagram of the Fe-C system. *Metallurgical Transactions*, 3(1):55–64, 1972.

[90] Michal Fulem, Květoslav Růžička, Ctirad Červinka, Marisa a.a. Rocha, Luís M.N.B.F. Santos, and Robert F. Berg. Recommended vapor pressure and thermophysical data for ferrocene. *The Journal of Chemical Thermodynamics*, 57:530–540, feb 2013.

[91] J.A. Martinho Simões. Organometallic Thermochemistry Data. In P.J. Linstrom and W.G. Mallard, editors, *NIST Chemistry WebBook, NIST Standard Reference Database Number 69*, chapter Organometa. National Institute of Standards and Technology, Gaithersburg MD, 20899, 2018.

[92] Jing Kong and Alan M Cassell. Chemical vapor deposition of methane for single-walled carbon nanotubes. *Chemical Physics Letters*, 292(August):567–574, 1998.

[93] Qingwen Li, Hao Yan, Jin Zhang, and Zhongfan Liu. Effect of hydrocarbons precursors on the formation of carbon nanotubes in chemical vapor deposition. *Carbon*, 42(4):829–835, 2004.

[94] Christian Hoecker, Fiona Smail, Martin Pick, and Adam Boies. The influence of carbon source and catalyst nanoparticles on CVD synthesis of CNT aerogel. *Chemical Engineering Journal*, 314:388–395, 2017.

[95] Samuel Aaron Miller. *Acetylene: its properties, manufacture, and uses.Vol I*. Ernest Benn, London, 1965.

[96] Gregory T Linteris, Marc D Rumminger, and Valeri I Babushok. Catalytic inhibition of laminar flames by transition metal compounds. *Progress in Energy and Combustion Science*, 34(3):288–329, 2008.

[97] Chao Hu, Wenzhi Li, Qizhao Lin, Xiaofang Cheng, Qifu Huang, Haitao Zhang, and Ziyu Wang. Effects of ferrocene on flame temperature, formation of soot particles and growth of polycyclic aromatic hydrocarbons. *Journal of the Energy Institute*, 90(6):893–901, 2017.

[98] Rajyashree M. Sundaram, Krzysztof K. K. Koziol, and Alan H. Windle. Continuous Direct Spinning of Fibers of Single-Walled Carbon Nanotubes with Metallic Chirality. *Advanced Materials*, 23(43):5064–5068, nov 2011.

[99] Qingfeng Liu, Wencai Ren, Zhi-Gang Chen, Da-Wei Wang, Bilu Liu, Bing Yu, Feng Li, Hongtao Cong, and Hui-Ming Cheng. Diameter-Selective Growth of Single-Walled Carbon Nanotubes with High Quality by Floating Catalyst Method. *ACS Nano*, 2(8):1722–1728, aug 2008.

[100] Hiroshi Ohtani and Taiji Nishizawa. Calculation of Fe-C-S Ternary Phase Diagram. *Transactions of the Iron and Steel Institute of Japan*, 26(7):655–663, 1986.

[101] Christoph T Wirth, Bernhard C Bayer, Andrew D Gamalski, Santiago Esconjauregui, Robert S Weatherup, Caterina Ducati, Carsten Baehtz, John Robertson, and Stephan Hofmann. The phase of iron catalyst nanoparticles during carbon nanotube growth. *Chemistry of Materials*, 24(24):4633–4640, 2012.

[102] Anton S. Anisimov, Albert G. Nasibulin, Hua Jiang, Pascale Launois, Julien Cambedouzou, Sergey D. Shandakov, and Esko I. Kauppinen. Mechanistic investigations of single-walled carbon nanotube synthesis by ferrocene vapor decomposition in carbon monoxide. *Carbon*, 48(2):380–388, 2010.

[103] Zhanbing He, Jean Luc Maurice, Aurélien Gohier, Chang Seok Lee, Didier Pribat, and Costel Sorin Cojocaru. Iron catalysts for the growth of carbon nanofibers: Fe, Fe3C or both? *Chemistry of Materials*, 23(24):5379–5387, 2011.

[104] Daniele Gozzi, Alessandro Latini, Laura Lazzarini, Dipartimento Chimica, Sapienza Uni V, and Piazzale Aldo Moro. Experimental Thermodynamics of High Temperature Transformations in Single-Walled Carbon Nanotube Bundles. *Journal of American Chemical Society*, 131(14):12474–12482, 2009.

[105] Andrey A. Levchenko, Alexander I. Kolesnikov, Olga Trofymluk, and Alexandra Navrotsky. Energetics of single-wall carbon nanotubes as revealed by calorimetry and neutron scattering. *Carbon*, 49(3):949–954, 2011.

[106] Daniele Gozzi, Massimiliano Iervolino, Alessandro Latini, La Sapienza, and Piazzale Aldo Moro. The Thermodynamics of the Transformation of Graphite to Multiwalled Carbon Nanotubes. *Journal of American Chemical Society*, 129:10269–10275, 2007.

[107] Gennady J. Kabo, Eugene Paulechka, Andrey V. Blokhin, Olga V. Voitkevich, Tatsiana Liavitskaya, and Andrey G. Kabo. Thermodynamic Properties and Similarity of Stacked-Cup Multiwall Carbon Nanotubes and Graphite. *Journal of Chemical & Engineering Data*, 61:3849–3857, 2016.

[108] Nikolay B. Cherkasov, Serguei V. Savilov, Anton S. Ivanov, and Valery V. Lunin. Bomb calorimetry as a bulk characterization tool for carbon nanostructures. *Carbon*, 63:324–329, 2013.

[109] E. V. Suslova, S. V. Savilov, J. Ni, V. V. Lunin, and S. M. Aldoshin. The enthalpies of formation of carbon nanomaterials as a key factor for understanding their structural features. *Physical Chemistry Chemical Physics*, 19(3):2269–2275, 2017.

[110] Charan Masarapu, L L Henry, and Bingqing Wei. Specific heat of aligned multiwalled carbon nanotubes. *Nanotechnology*, 16(9):1490–1494, 2005.

[111] A Mizel, L X Benedict, M L Cohen, S G Louie, A Zettl, N K Budraa, and W P Beyermann. Analysis of the low-temperature specific heat of multiwalled carbon nanotubes and carbon nanotube ropes. *Physical Review B*, 60(5):3264–3270, 1999.

[112] N R Pradhan, H Duan, J Liang, and G S Iannacchione. The specific heat and effective thermal conductivity of composites containing single-wall and multi-wall carbon nanotubes. *Nanotechnology*, 20(24):245705, 2009.

[113] Lorin X. Benedict, Steven G. Louie, and Marvin L. Cohen. Heat capacity of carbon nanotubes. *Solid State Communications*, 100(3):177–180, 1996.

[114] Daniele Gozzi, Alessandro Latini, and Massimo Tomellini. Thermodynamics of CVD Synthesis of Multiwalled Carbon Nanotubes : A Case Study Thermodynamics of CVD Synthesis of Multiwalled Carbon Nanotubes : A Case Study. *The Journal of Physical Chemistry C*, 5(2):45–53, 2009.

[115] Chunyu Li and Tsu-Wei Chou. Modeling of heat capacities of multi-walled carbon nanotubes by molecular structural mechanics. *Materials Science and Engineering: A*, 409(1-2):140–144, 2005.

[116] J Hone, M C Llaguno, M J Biercuk, a T Johnson, B Batlogg, Z Benes, and J E Fischer. Thermal properties of carbon nanotubes and nanotube-based materials. *Applied Physics A: Materials Science & Processing*, 74(3):339–343, 2002.

[117] H Yoshida, S Takeda, T Uchiyama, H Kohno, and Y Homma. Atomic-scale in-situ observation of carbon nanotube growth from solid state iron carbide nanoparticles. *Nano Letters*, 8(7):2082–2086, 2008.

[118] Xianfeng Zhang, a Cao, B Wei, Y Li, J Wei, C Xu, and D Wu. Rapid growth of well-aligned carbon nanotube arrays. *Chemical Physics Letters*, 362(August):285–290, 2002.

[119] SW Pattinson and RE Diaz. In Situ Observation of the Effect of Nitrogen on Carbon Nanotube Synthesis. *Chemistry of Materials*, 25:2921–2923, 2013.

[120] A. Leonhardt, M. Ritschel, R. Kozhuharova, A. Graff, T. Muhl, R. Huhle, I. Monch, D. Elefant, and C. M. Schneider. Synthesis and properties of filled carbon nanotubes. *Diamond and Related Materials*, 12:790–793, 2003.

[121] Andreas K Schaper, Haoqing Hou, Andreas Greiner, and Fritz Phillipp. The role of iron carbide in multiwalled carbon nanotube growth. *Journal of Catalysis*, 222(1):250–254, 2004.

[122] J. Oudar. Sulfur Adsorption and Poisoning of Metallic Catalysts. *Catalysis Reviews*, 22(2):171–195, jan 1980.

[123] Qiang Zhang, Kewei Li, Qingxia Fan, Xiaogang Xia, Nan Zhang, Zhuojian Xiao, Wenbin Zhou, Feng Yang, Yanchun Wang, Huaping Liu, and Weiya Zhou. Performance improvement of continuous carbon nanotube fibers by acid treatment. *Chinese Physics B*, 26(2), 2017.

[124] G. Ortega-Cervantez, G. Rueda-Morales, and J. Ortiz-López. Catalytic CVD production of carbon nanotubes using ethanol. *Microelectronics Journal*, 36(3-6):495–498, 2005.

[125] S. Chaisitsak, J. Nukeaw, and A. Tuantranont. Parametric study of atmospheric-pressure single-walled carbon nanotubes growth by ferrocene-ethanol mist CVD. *Diamond and Related Materials*, 16(11):1958–1966, 2007.

[126] Yuchi Che, Chuan Wang, Jia Liu, Bilu Liu, Xue Lin, Jason Parker, Cara Beasley, H. S.Philip Wong, and Chongwu Zhou. Selective synthesis and device applications of semiconducting single-walled carbon nanotubes using isopropyl alcohol as feedstock. *ACS Nano*, 6(8):7454–7462, 2012.

[127] Millie S. Dresselhaus, G. Dresselhaus, R. Saito, and A. Jorio. Raman spectroscopy of carbon nanotubes. *Physics Reports*, 409(2):47–99, 2005.

[128] L. Slavov, M. V. Abrashev, T. Merodiiska, Ch Gelev, R. E. Vandenberghe, I. Markova-Deneva, and I. Nedkov. Raman spectroscopy investigation of magnetite nanoparticles in ferrofluids. *Journal of Magnetism and Magnetic Materials*, 322(14):1904–1911, 2010.

[129] D. L. A. de Faria, S. Venâncio Silva, and M. T. de Oliveira. Raman microspectroscopy of some iron oxides and oxyhydroxides. *Journal of Raman Spectroscopy*, 28(11):873–878, 1997.

[130] Susana L H Rebelo, Alexandra Guedes, Monika E Szefczyk, M Pereira, and Cristina Freire. Progress in the Raman spectra analysis of covalently functionalized multiwalled carbon nanotubes : unraveling disorder in graphitic materials. *Physical Chemistry Chemical Physics*, 18:12784–12796, 2016.

[131] A. Sadezky, H. Muckenhuber, H. Grothe, R. Niessner, and U. Pöschl. Raman microspectroscopy of soot and related carbonaceous materials: Spectral analysis and structural information. *Carbon*, 43(8):1731–1742, 2005.

[132] Abigail C. Allwood, Malcolm R. Walter, and Craig P. Marshall. Raman spectroscopy reveals thermal palaeoenvironments of c.3.5 billion-year-old organic matter. *Vibrational Spectroscopy*, 41(2):190–197, 2006.

[133] Markus Knauer, Matteo Carrara, Dieter Rothe, Reinhard Niessner, and Natalia P. Ivleva. Changes in structure and reactivity of soot during oxidation and gasification by oxygen, studied by micro-Raman spectroscopy and temperature programmed oxidation. *Aerosol Science and Technology*, 43(1):1–8, 2009.

[134] Joseph Goldstein, Dale E. Newbury, Joseph R. Michael, Nicholas W. M. Ritchie, John Henry J. Scott, and David C. Joy. *Scanning electron microscopy and x-ray microanalysis*. Springer, New York, fourth edition, 2016.

[135] C. N. R. Rao and A. Govindaraj. Carbon Nanotubes. In *Nanotubes and Nanowires*, chapter 1, pages 1–242. Royal Society of Chemistry, 2 edition, 2011.

[136] H. W. Zhu, C. L. Xu, D. H. Wu, B. Q. Wei, R. Vajtai2, and P. M. Ajayan. Direct Synthesis of Long Single-Walled Carbon Nanotube Strands. *Science*, 296(5569):884–886, 2002.

[137] G. H. Du, W. Z. Li, Y. Q. Liu, Y. Ding, and Z. L. Wang. Growth of carbon nanotubes by pyrolysis of thiophene. *Journal of Physical Chemistry C*, 111(39):14293–14298, 2007.

[138] R Andrews, D Jacques, AM Rao, and J Chen. Continuous production of aligned carbon nanotubes: a step closer to commercial realization. *Chemical physics Letters*, 303(April):467–474, 1999.

[139] V W Brar, M S Dresselhaus, G Dresselhaus, R Saito, A K Swan, B B Goldberg, A G Souza Filho, and A Jorio. Second-order harmonic and combination modes in graphite , single-wall carbon nanotube bundles , and isolated single-wall carbon nanotubes. *Physical Review B*, 66:155418, 2002.

[140] S D M Brown, A Jorio, and P Corio. Origin of the Breit-Wigner-Fano lineshape of the tangential G -band feature of metallic carbon nanotubes. *Physical Review B*, 63:155414, 2001.

[141] Georgi Genchev and Andreas Erbe. Raman Spectroscopy of Mackinawite FeS in Anodic Iron Sulfide. *Journal of The Electrochemical Society*, 163(6):5–10, 2016.

[142] A Jorio, M. A. Pimenta, A. G. S. Filho, R Saito, G. Dresselhaus, and M. S. Dresselhaus. Characterizing carbon nanotube samples with resonance Raman scattering Characterizing carbon nanotube samples with resonance Raman scattering. *New Journal of Physics*, 5(1):139.1 – 139.17, 2003.

[143] Anthony F. Mills. *Heat and mass transfer*. Irwin, 1995.

[144] John H Lienhard IV and John H Lienhard V. *A Heat Transfer Textbook*. Phlogiston Press, Cambridge Massachusetts, fourth edition, 2011.

Appendix A

List of Species for Equilibrium Study

Table A.1 Species list

Species group	Literature
Gas phase species:	[82]
C, CH, CH_2, CH_3, CH_4, C_2, C_2H,	
C_2H_2(acetylene), C_2H_2(vinylidene), C_2H_3(vinyl),	
C_2H_4, C_2H_5, C_2H_6, C_3, C_3H_3(propargyl),	
C_3H_4(allene), C_3H_4(propyne), C_3H_4(cyclo-)	
C_3H_5(allyl), C_3H_6(propylene), C_3H_6(cyclo-),	
C_3H_7(n-propyl), C_3H_7(i-propyl), C_3H_8,	
C_4, C_4H_2, C_4H_4(1,3-cyclo-), C_4H_6(butadiene),	
C_4H_6(2-butyne), C_4H_6(cyclo-), C_4H_8(1-butene),	
C_4H_8(cis2-buten), C_4H_8(tr2-butene), C_4H_8(isobutene),	
C_4H_8(cyclo-), C_4H_9(n-butyl), C_4H_9(i-butyl),	
C_4H_9(s-butyl), C_4H_9(t-butyl), C_4H_{10}(isobutane),	
C_4H_{10}(n-butane), C_5, C_5H_6(1,3cyclo-),	
C_5H_8(cyclo-), C_5H_{10}(1-pentene), C_5H_{10}(cyclo-),	
C_5H_{11}(pentyl), C_5H_{11}(t-pentyl), C_5H_{12}(n-pentane),	
C_5H_{12}(i-pentane), $CH_3C(CH_3)_2C_3$,	
C_6H_2, C_6H_5(phenyl), C_6H_6,	
C_6H_{10}(cyclo-), C_6H_{12}(1-hexene), C_6H_{12}(cyclo-),	
C_6H_{13}(n-hexyl), C_7H_7(benzyl), C_7H_8,	
C_7H_{14}(1-heptene), C_7H_{15}(n-heptyl), C_7H_{16}(n-heptane),	
C_8H_8(styrene), C_8H_{10}(ethylbenz), C_8H_{16}(1-octene),	
C_8H_{17}(n-octyl), C_8H_{18}(isooctane), C_8H_{18}(n-octane),	

C_9H_{19}(n-nonyl), $C_{10}H_8$(naphthale), $C_{10}H_{21}$(n-decyl), $C_{12}H_9$(o-biphenyl), $C_{12}H_{10}$(biphenyl), $C_{12}H_{23}$(Jet-A(g)), CS, CS_2, H, H_2, H_2S, S, SH, S_2, S_8, Fe, CN, CNN, CH_3CN, $CH_3N_2CH_3$, CCN, CNC, C_2N_2, C_4N_2, HCN, HCCN, HNC, N, NH, NH_2, NH_3, N_2, NCN, N_2H_2, N_2H_4, N_3, N_3H, SN, Ar, C_3H_5O, $C_4H_{10}O$, $C_4H_{10}O_2$, FeO_2 CH_2OH, CH_3O, CH_3OH, CO, COS, CO_2, COOH, CHCO(ketyl), CH_2CO(ketene), CH_3CO(acetyl), C_2H_4(ethylen), CH_3CHO(ethanal), CH_3COOH, $(HCOOH)_2$, CH_3OCH_3, C_2H_5OH, C_2O, C_3H_6O, C_3H_8O(1-propanol), C_3H_8O(2-propanol), C_3O_2, $(CH_3COOH)_2$, C_6H_5O(phenoxy), C_6H_5OH(phenol), C_7H_8O(cresol), FeC_5O_5, FeO, $Fe(OH)_2$, HCO, HO_2, HCHO(formaldehy), HCOOH, H_2O, H_2O_2, H_2SO_4, O, OH, O_2, O_3, SO, SO_2, SO_3, S_2O, HCCO, HCCOH, CH_2CHO, CH_3CHO CH_2O **Solid phase species:** α-Fe(s), γ-Fe(s), δ-Fe(s), FeS(s), FeS_2(s), C(s), FeO(s), Fe_2O_3(s) Fe_3O_4(s), $Fe(OH)_2$(s), $Fe(OH)_3$(s), $FeSO_4$(s), $Fe_2S_3O_{12}$(s) **Liquid phase species:** Fe(l), S(l), FeS(l), FeO(l), FeC_5O_5(l), H_2SO_4, H_2O(l)	
FeS(g), C_4H_4S(g), Fe_3C(s), Fe_3C(l)	[87]
$Fe(C_5H_5)_2$(g)	[90]
CNTs by Gozzi *et.al*	[106]
CNTs by Kabo *et.al*	[107]
CNTs by Levchenko *et.al*	[105]

Appendix B

Summary of Experimental Conditions

Experimental details of the flame synthesis of CNTs have been illustrated in Chapter 5 and 6; we here summarise all the experimental conditions in Table B.1:

Table B.1 Summary of experimental conditions

Test No.	ϕ	H_2 (slpm)	Air (slpm)	Ferrocene (wt.%)	Thiophene (wt.%)	$\dot{q}$ (ml/min)	$\dot{V}_{Ar}$ (slpm)	$\dot{m}''$ (kg m^{-2} s^{-1})
Effects of Varying ϕ								
A1	1.0	7	17.5	1.0	0	0.5	0.1	0.27
A2	1.05		16.7					0.26
A3	1.1		16.0					0.25
A4	1.15		15.3					0.24
A5	1.2		14.6					0.23
A6	1.3		13.5					0.21
A7	1.4		12.6					0.20
A8	1.5		11.7					0.18
Effects of varying $\dot{q}$								
B1	1.05	7	16.7	1.0	0	0.1	0.1	0.26
B2						0.3		
B3						0.5		
B4						0.7		
B5						1.0		
B6						1.5		
B7						2.0		
Effects of varying $\dot{V}_{Ar}$								
C1	1.05	7	16.7	1.0	0	0.5	0.05	0.26
C2							0.1	
C3							0.2	
C4							0.5	
C5							1.0	

Table B.1...*continued*.

Test No.	ϕ	H_2 (slpm)	Air (slpm)	Ferrocene (wt.%)	Thiophene (wt.%)	$\dot{q}$ (ml/min)	$\dot{V}_{Ar}$ (slpm)	$\dot{m}''$ (kg m^{-2} s^{-1})
Effects of varying $\dot{m}''$								
D1	1.05	3.5	8.4	1.0	0	0.5	0.1	0.13
D2		5.3	12.5					0.19
D3		7.0	16.7					0.26
D4		10.5	25.0					0.39
Effects of varying ferrocene								
	1.05	7	16.7	0.1	0	0.5	0.1	0.26
F1	1.1		16.0					0.25
	1.2		14.6					0.23
	1.05		16.7	0.3				0.26
F2	1.1		16.0					0.25
	1.2		14.6					0.23
	1.05		16.7	0.5				0.26
F3	1.1		16.0					0.25
	1.2		14.6					0.23
	1.05		16.7	1.0				0.26
F4	1.1		16.0					0.25
	1.2		14.6					0.23
	1.05		16.7	2.0				0.26
F5	1.1		16.0					0.25
	1.2		14.6					0.23
	1.05		16.7	3.0				0.26
F6	1.1		16.0					0.25
	1.2		14.6					0.23

Table B.1...*continued*.

Test No.	ϕ	H_2 (slpm)	Air (slpm)	Ferrocene (wt.%)	Thiophene (wt.%)	$\dot{q}$ (ml/min)	$\dot{V}_{Ar}$ (slpm)	$\dot{m}''$ (kg m^{-2} s^{-1})
Effects of varying ϕ								
S1	1.05	7	16.7	1.0	0	0.5	0.1	0.26
	1.1		16.0					0.25
	1.15		15.3					0.24
	1.2		14.6					0.23
S1	1.05		16.7	1.0	0			0.26
	1.1		16.0					0.25
	1.15		15.3					0.24
	1.2		14.6					0.23
S2	1.05		16.7	2.3	1.5			0.26
	1.1		16.0					0.25
	1.15		15.3					0.24
	1.2		14.6					0.23
S3	1.05		16.7	1.0	1.6			0.26
	1.1		16.0					0.25
	1.15		15.3					0.24
	1.2		14.6					0.23
S4	1.05		16.7	0.5	2.0			0.26
	1.1		16.0					0.25
	1.15		15.3					0.24
	1.2		14.6					0.23
S5	1.05		16.7	0.25	2.0			0.26
	1.1		16.0					0.25
	1.15		15.3					0.24
	1.2		14.6					0.23